A SEISMIC REFRACTION STUDY OF THE HECATE SUB-BASIN, BRITISH COLUMBIA

by

CHRISTOPHER JAMES PIKE

B.Sc.(Physics), The University of Toronto, 1982

A THESIS SUBMITTED IN PARTIAL FULFILLMENT OF

THE REQUIREMENTS FOR THE DEGREE OF

MASTER OF SCIENCE

in

THE FACULTY OF GRADUATE STUDIES

Department of Geophysics and Astronomy

We accept this thesis as conforming

to the required standard

THE UNIVERSITY OF BRITISH COLUMBIA

November 1986

In presenting this thesis in partial fulfilment of the requirements for an advanced degree at the University of British Columbia, I agree that the Library shall make it freely available for reference and study. I further agree that permission for extensive copying of this thesis for scholarly purposes may be granted by the head of my department or by his or her representatives. It is understood that copying or publication of this thesis for financial gain shall not be allowed without my written permission.

Department of Geophysics and Astronomy

The University of British Columbia
1956 Main Mall
Vancouver, Canada
V6T 1Y3

Date November 2, 1986

To my grandmother,

Nanny Pike,

who passed away

three short weeks

before the completion of this thesis

ABSTRACT

The Hecate sub-basin is one of two similar sedimentary structures comprising Queen Charlotte Basin, which is located between the British Columbia mainland and the Queen Charlotte Islands. The Queen Charlotte Basin was the locale of an active but unsuccessful exploration program, including drill holes, in the 1960's. However, recent studies incorporating modern concepts of plate tectonics have indicated a re-evaluation of the resource potential of the area is warranted. The Hecate sub-basin and its southern counterpart, the Charlotte sub-basin, are filled with Tertiary sediments that are underlain by a thick sequence of Tertiary volcanics. Penetration of the latter unit using the reflection method has been difficult. Thus the thickness of the volcanics and the existence or not of more sediments below them has not been established. To address this problem an airgun/ocean bottom seismograph (OBS) refraction survey was carried out across the Hecate sub-basin in 1983. Data from the airgun shots at approximately 160 m spacings were recorded on four OBSs deployed at 20 km intervals to provide a series of reverse profiles extending over 60 km. The principal interpretation procedure involved calculation of theoretical seismograms and travel-time curves for 2–D velocity structure models and comparisons with observed record sections.

The interpreted structure model shows significant lateral variations. Low velocity Pleistocene and Pliocene sediments form an upper layer varying between 0.5 and 1.0 km thick. The principal sedimentary unit is the Tertiary Skonun Formation with interpreted velocities of 2.7 km/s and a gradient averaging 0.4 km/s/km, values that are consistent with well log data. These sediments are generally thicker (approximately 2.5 km) on the western side of the sub-basin although they reach their maximum thickness of 3 km in a depression near the central part of the basin. Toward the eastern side of the

basin, the Tertiary sediments thin to about 1 km as the underlying Tertiary volcanics rise toward the mainland. The maximum sediment thickness in the basin is about 4 km. The upper surface of the volcanic unit shows a pronounced topography which is consistent with the erosional nature of this surface. Velocities for the volcanics vary between 4.8 and 5.0 km/s; thickness of the unit ranges from about 0.2 km to 1.8 km. Below the Tertiary volcanics on the eastern 20 km of the model, a low velocity zone less than 1 km thick had to be introduced to satisfy the data. This zone is inferred to contain Upper Cretaceous sediments. A unit with a poorly constrained velocity of 5.9 km/s which underlies the Tertiary volcanics and low velocity zone on the eastern side is interpreted to be the Paleozoic Alexander Terrane. Most of the characteristics of this model are similar to those determined from an earlier study in the Charlotte sub-basin.

An additional component of this thesis project was the development of an interactive procedure for the inversion of densely spaced seismic refraction data by wavefield continuation to derive a 1-D velocity-depth profile, and its application to data derived from 2-D structures. The procedure consists of two steps: a slant stack followed by a downward continuation. The method was found to yield velocity-depth structures which, when compared with an average velocity-depth structure from the 2-D model, have very similiar gradients and velocity increases. In general the velocity depth curve from the inversion had lower velocities at deeper depths than the averaged 2-D structure.

TABLE OF CONTENTS

LIST OF TABLES

LIST OF FIGURES

ACKNOWLEDGEMENTS

I would like to thank my supervisor, Dr. Ron M. Clowes, for his support and encouragement over the past years. I am particularly grateful for his patient and painstaking reviews of this thesis. I would also like to thank Dr. Robert M. Ellis for critically reviewing this thesis, particularly in light of the severe time constraints.

Without the invaluable help from Kathy Penney and Andy Boland during the final stages of this thesis it would not have been completed in time. This is also true of David Mackie and Joane Berube who offered much needed assistance in the preparation of figures. David Mackie is also responsible for many of the programs used in processing the origional analog tapes. The efforts of Phil Ross and Elaine Wright are also greatly appreciated. The use of TEX files compiled by Sonya Dehler permitted the quick understanding of this text writing package. The people of the Geophysics and Astronomy Department are responsible for making the time spent at UBC very enjoyable.

Financial support for data acquisition and analysis was provided by NSERC through Operating Grant A7707 and Strategic (Oceans) Grant G0738, by D.S.S. contract 05SU.23235-3-1089 from the Earth Physics Branch, E.M.R., and by D.S.S. contracts 06SB.23445-4-1170 and 11SB.23227-5-0127 from the Pacific Geoscience Centre, E.M.R. Additional support was provided by Chevron Canada Resources Ltd., Shell Canada Resources Ltd. and Mobil Oil Canada Ltd..

CHAPTER I INTRODUCTION

Hecate Strait is situated between the west coast of mainland British Columbia and the Queen Charlotte Islands in the latitude range 52° to 54° N. It is underlain by the Queen Charlotte basin, a north-south trending depression 400 km long and 100 km wide which to the northwest also underlies northeastern Graham Island and Dixon Entrance and to the south Queen Charlotte Sound (Figure 1.1). The Queen Charlotte basin forms part of the coastal depression bordering the western margin of North America and is one of many sedimentary basins with ages ranging from Late Mesozoic to Cenozoic (Figure 1.2). In terms of the basin's size, it resembles the Cook Inlet and Bristol Bay basins in Alaska and the Sacremento-San Joaquin basin in California (Young, 1981).

The hydrocarbon potential of the area was investigated as early as 1912 with the drilling of the Tian No.1 well which reached a depth of 490 m and bottomed in Paleocene Masset volcanics (see Table 1 of Appendix I for formation nomenclature). This well and others drilled on the islands during the period 1950-1961 did not show any significant hydrocarbon finds. Exploration was renewed in the 1960's when Shell Canada Ltd. drilled a number of wells off the west coast of British Columbia, including eight in Hecate Strait and Queen Charlotte Sound (Figure 1.1; Shouldice 1971, 1973). The exploratory wells in Hecate Strait were drilled on structural highs defined by relatively poor reflection seismic data and also did not result in any significant oil and gas shows. Activity ended with the moratorium on exploration in the early 1970's.

Between 1970 and the present, several factors have contributed to a renewed interest in the basins off the west coast of British Columbia, and particularly the Queen Charlotte basin. The relationship between plate tectonics and the world-wide distribution

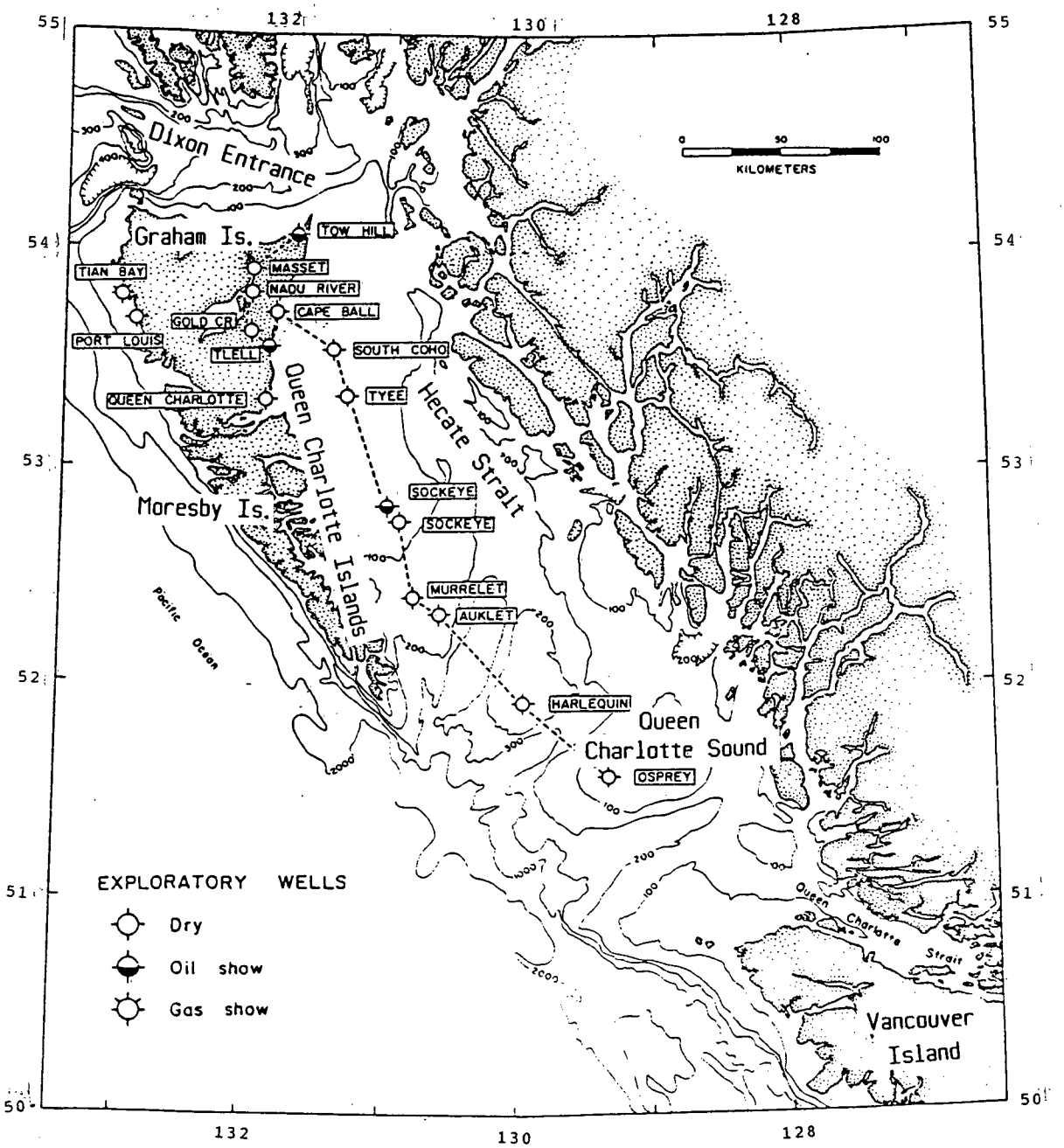

Figure 1.1 Location map for the Queen Charlotte Islands, Hecate Strait and Queen Charlotte Sound. Exploratory wells drilled by Richfield Oil Corporation on the Queen Charlottte Islands and Shell Canada Ltd. in Hecate Strait and Queen Charlotte Sound are indicated by boxed labels (after Young, 1981).

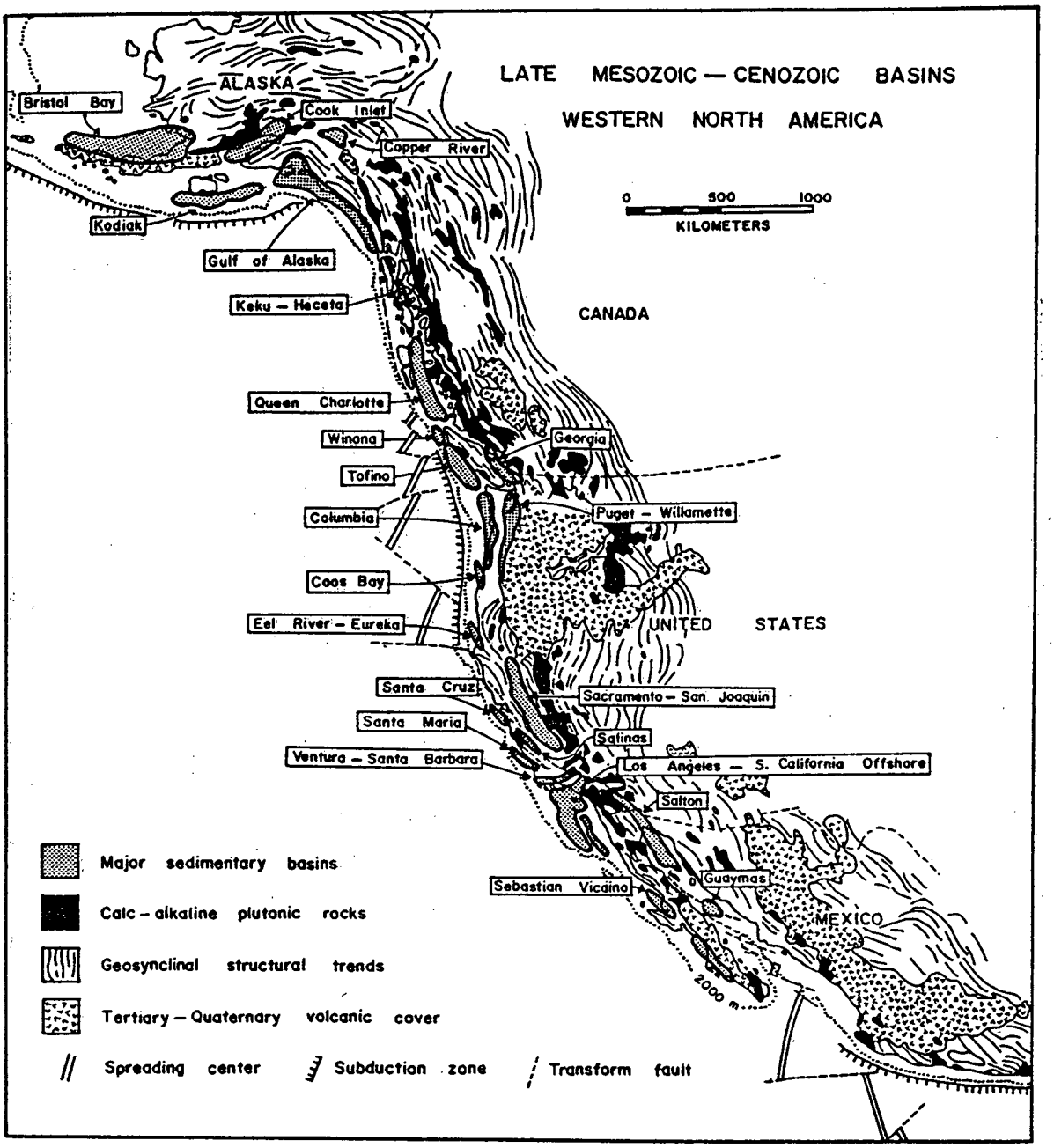

Figure 1.2 Late Mesozoic—Cenozoic basins of the of the Pacific margin (after Young, 1981).

of hydrocarbons highlighted many prospective areas (eg. Rona, 1980). Oil companies began to adopt these principles in their analysis of basin development. The concept of accreted terranes, which are fragments of more ancient material that has been juxtaposed against other terranes and/or cratons with vastly differing evolutions, was easily accommodated by plate tectonic theory. The Alexander and Wrangellia Terranes have been identified as examples of this process (Berg *et al.*, 1972; and Jones *et al.*, 1977 respectively). These accreted terranes originated in more equatorial environments, consequently may have developed organic-rich formations unrelated to the adjoining terranes, and thus warrant independent investigation. The recent studies of the evolution of the Queen Charlotte basin and surrounding regions by Yorath and Chase (1981), Yorath and Cameron (1982), Yorath and Hyndman (1983), Mackie (1985), Clowes and Gens-Lenartowicz (1985) and Dehler (1986) have contributed greatly to the present understanding of the region.

1.1 Tectonic Evolution of the Queen Charlotte Basin

Yorath and Chase (1981) reviewed the work of Sutherland Brown (1968) and Shouldice (1971, 1973), and integrated this with their own and other studies to develop a model for the evolution of the Queen Charlotte basin. They simplified the geology and tectonics of the region by defining four basic tectonic assemblages. The Paleozoic Alexander Terrane and the Mesozoic Wrangellia Terrane comprise the allochthonous assemblages; the Upper Jurassic plutons and Lower Cretaceous Longarm Formation (Table 1, Appendix I) make up the suture Assemblage; the post suture assemblage consists of the Middle to Upper Cretaceous Queen Charlotte Group (Table 1, Appendix I); and the mid-Tertiary plutons, Masset volcanics and Neogene Skonun formation comprise the rift assemblage.

Berg *et al.* (1972) defined the Alexander Terrane as a complex assemblage of sedimentary, igneous and metamorphic rocks ranging from Late Precambrian to Late Paleozoic in age. Rocks of Late Triassic age unconformably overlie Permian limestones in the southern part of the terrane (Berg *et al.*, 1978). The metasedimentary and metavolcanic rocks along the margin of the Coast Mountains have also been included in the Alexander Terrane by Yorath and Chase (1981). Van der Voo *et al.* (1980) and Van der Voo and Channel (1980) have obtained paleomagnetic results from Ordovician, Devonian and Carboniferous rocks from southeastern Alaska which clearly indicate the exotic nature of the Alexander Terrane. Displacements of 1800 km relative to cratonic North America between Late Carboniferous and Triassic time have been determined.

Jones *et al.* (1977) described the terrane underlain by Middle to Upper Triassic tholeitic basalts and calcareous sedimentary rocks which occur in the Wrangell Mountains and Chichagof Islands as Wrangellia. Yorath and Chase (1981) also included Jurassic volcanic and sedimentary rocks under the definition for Wrangellia. The 4300 m of tholeitic pillow lavas, pillow basalts, equagene tuffs, and the massive basalt flows of the Upper Triassic Karmutsen Formation conformably overlie about 100 m of limestone and argillite of the Upper Triassic to Lower Jurassic Kunga Formation (Sutherland Brown, 1968). This formation, together with the terrigenous clastics and calc-alkaline volcanics of Early to Middle Jurassic age on Queen Charlotte Islands (the Maude and Yakoun Formations), are included in Wrangellia by Yorath and Chase (1981) following upon evidence from Tipper and Cameron (1980), who found ammonite faunas in the Yakoun Formation that developed in a warm-water environment. Paleomagnetic evidence from the Nicolai Greenstone belt in the Wrangell Mountains (Hillhouse, 1977) suggests a northward displacement of 3000 km or 6000 km prior to their accretion to

the North American continental margin (the different results depend upon whether a northern or southern hemispherical solution is chosen).

The model proposed by Yorath and Cameron (1982) for the evolution of the Pacific margin in the vicinity of the Queen Charlotte Islands is depicted in Figure 1.3. By late Triassic time, the Alexander Terrane had reached its present latitude (Figure 1.3a). There was a cessation of the northward movement of the Alexander Terrane following collision with Wrangellia. By some process, the northward movement of the two terranes was converted to movement in a northeasterly direction (Figure 1.3b). The unconformity between the Longarm Formation, characterizing the suture zone, and the Middle Jurassic rocks may be indicative of the Lower Cretaceous–Upper Jurassic collision event (Table 1, Appendix 1). The Longarm Formation consists of sandstones, siltstones and conglomerates (Sutherland-Brown, 1968). Sutherland Brown (1968) noted large blocks of andesitic volcanic rocks (8 to 10 m in size) occurring closely above the unconformable contact. Such large clasts would have to have been derived from the rapid development of substantial relief in zones adjacent to the suture zone (Yorath and Chase, 1981). Figure 1.4 shows the major faults in the region of the Queen Chatlotte Islands. The offshore trace of the Rennell Sound Fault, which coincides with the trend of a prominent gravity anomaly and a seismic reflection survey interpreted by Yorath (Yorath and Chase, 1981), has led the authors to suggest that this fault zone represents the boundary between the Alexander and Wrangellia terranes. They propose that the structural depression, as evident from gravity and seismic data, was possibly due to a relocation of compressive stresses in a post-collisional regime.

Following the Late Jurassic to Early Cretaceous suturing, the two terranes then docked with North America somewhere between 90 and 40 Ma ago (Figure 1.3c) and may have been responsible for the plutonic uplift within the Coast Mountains. The post

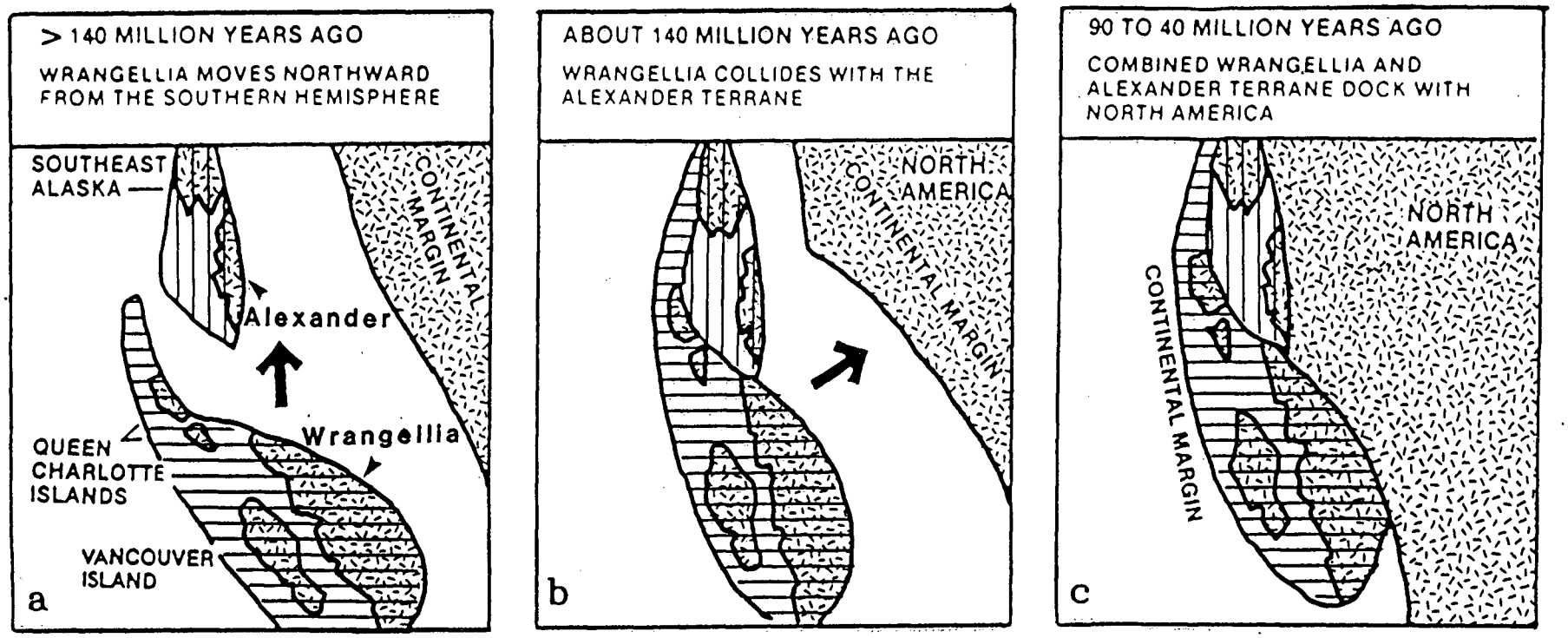

Figure 1.3 Schematic diagram for the tectonic evolution of the Pacific Northwest margin showing the collision of Wrangellia with Alexander and then with the Pacific Margin (Yorath and Cameron, 1982).

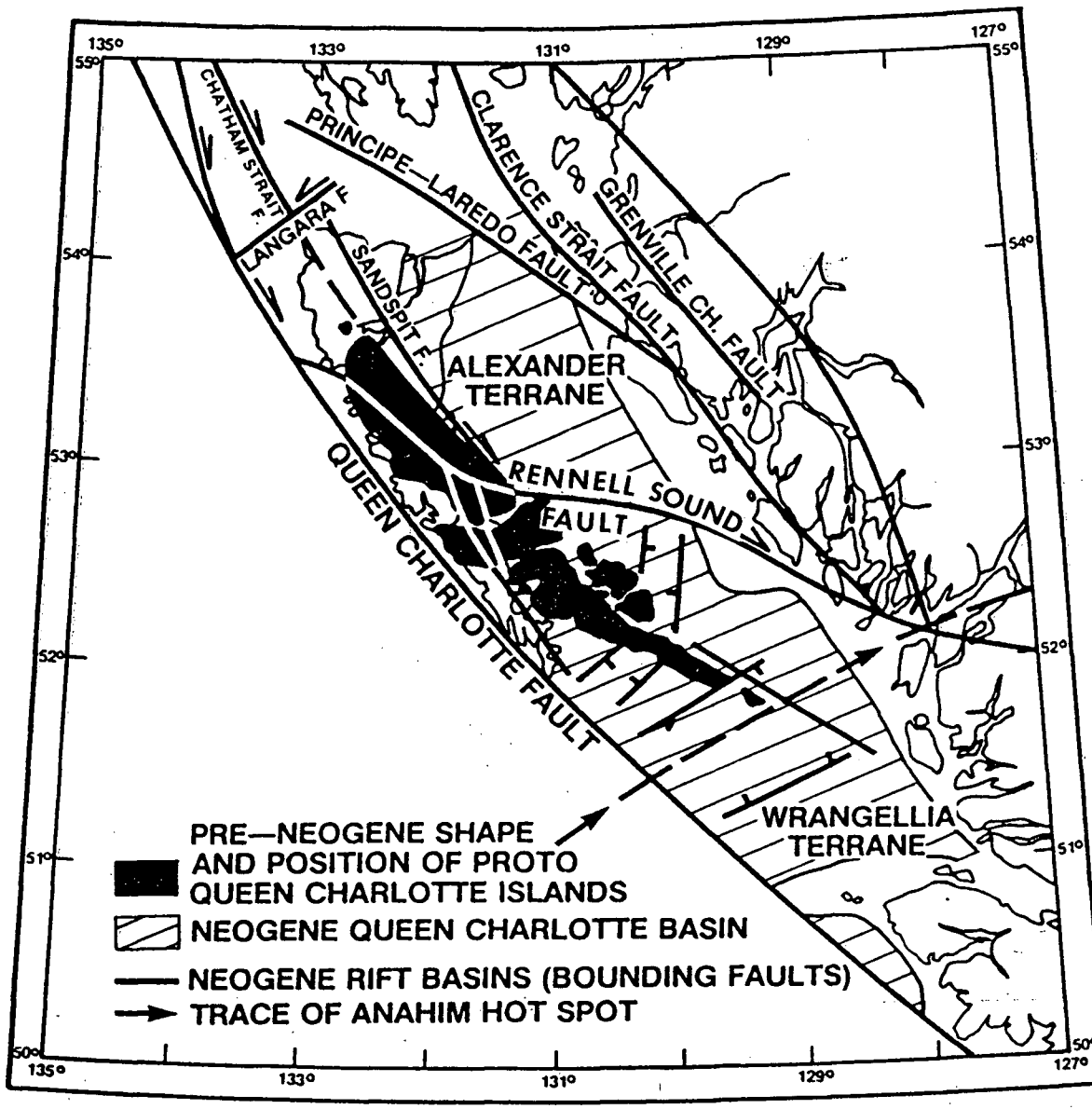

Figure 1.4 Present day relationship between Wrangellia and Alexander terranes showing the major faults and the position of the proto-Queen Charlotte Islands (after Yorath and Hyndman, 1983).

suture assemblage, composed of the Mid to Upper Cretaceous Queen Charlotte Group, was deposited across the suture zone and overlies Wrangellia, the Alexander Terrane and the suture assemblage.

The fourth evolutionary stage is represented by the Masset and Skonun Formations and by a series of intermediate epizonal plutons, all of Tertiary age, defined by Yorath and Chase (1981) as the rift assemblage. Also related to the rift assemblage are several peralkaline volcanic centres of the Anahim volcanic belt.

The Masset Formation is composed of pyroclastic rocks consisting primarily of alkalic basalt and sodic rhyolite (Sutherland Brown, 1968). The formation is 1200 to 5500 m thick, erupted subaerially for the most part, and rests unconformably on all older units on the Queen Charlotte Islands. The age of the formation varies between Paleocene and Miocene (62 and 11 Ma) (Young, 1981). The mean age of the Masset volcanics for the Queen Charlotte Islands is 27 Ma (Late Oligocene), while for Hecate Strait and Queen Charlotte Sound it is 35 Ma (Early Oligocene). The origin of the formation has been suggested as upper mantle material for the basalts and remelted Paleozoic plutonic rocks for the rhyolites (Sutherland Brown, 1968).

The Skonun Formation consists of marine and non-marine sands, sandstone, shale, lignite stringers and conglomerates (Sutherland Brown, 1968). Where found on the Queen Charlotte Islands, it rests unconformably on the Masset volcanics. The formation thickens towards the east into Hecate Strait and Queen Charlotte Sound and ranges in age from Early Miocene to Late Pliocene.

North of the assumed suture zone, the Skonun and Masset formations overly the Cretaceous and/or Jurassic rocks of the post suture assemblage (Yorath and Chase,

1981). They are also found in fault contact with the Jurassic rocks of Wrangellia and the Cretaceous strata of the post-suture assemblage on the Queen Charlotte Islands.

1.2 Subsidence of the Queen Charlotte basin

The Queen Charlotte sedimentary basin is comprised of several subsidiary basins, of which the Hecate sub-basin and the Charlotte sub-basin are considered the most important. These are separated by a basement topographic high known as the Moresby Ridge, which runs in a northeasterly direction from southern Moresby Island (Figure 1.5). The basement ridge is located roughly in the center of the Queen Charlotte basin.

Yorath and Hyndman (1983) have proposed a model for the subsidence of the Queen Charlotte basin which combines an initial stage of rifting, followed by flexural down-warping and sediment loading, which resulted from the oblique convergence of oceanic lithosphere with the North American continental margin. They argue that if the trace of the Anahim hot spot is extrapolated backwards in time, it would have passed beneath Queen Charlotte Sound (Figure 1.6a). Furthermore, the rifting and crustal extension which occurred were responsible for the widespread subareal Masset volcanics. This rifting activated or reactivated the Rennell Sound-Sandspit Fault, which allowed the proto-Queen Charlotte Islands to move to their present latitude (Figure 1.6b). Heat flow from the Queen Charlotte basin offshore wells is high for the northern three wells (Figure 1.7), particularly the Sockeye well, which coincides with the proposed suture between Wrangellia and Alexander terranes. The depressed heat flow in the four southern wells is thought to be due to recent underthrusting of oceanic lithosphere. The rifting is considered to have occurred during a period of regional uplift and to have commenced about 21 Ma ago and ceased 17 Ma ago (Yorath and Hyndman, 1983).

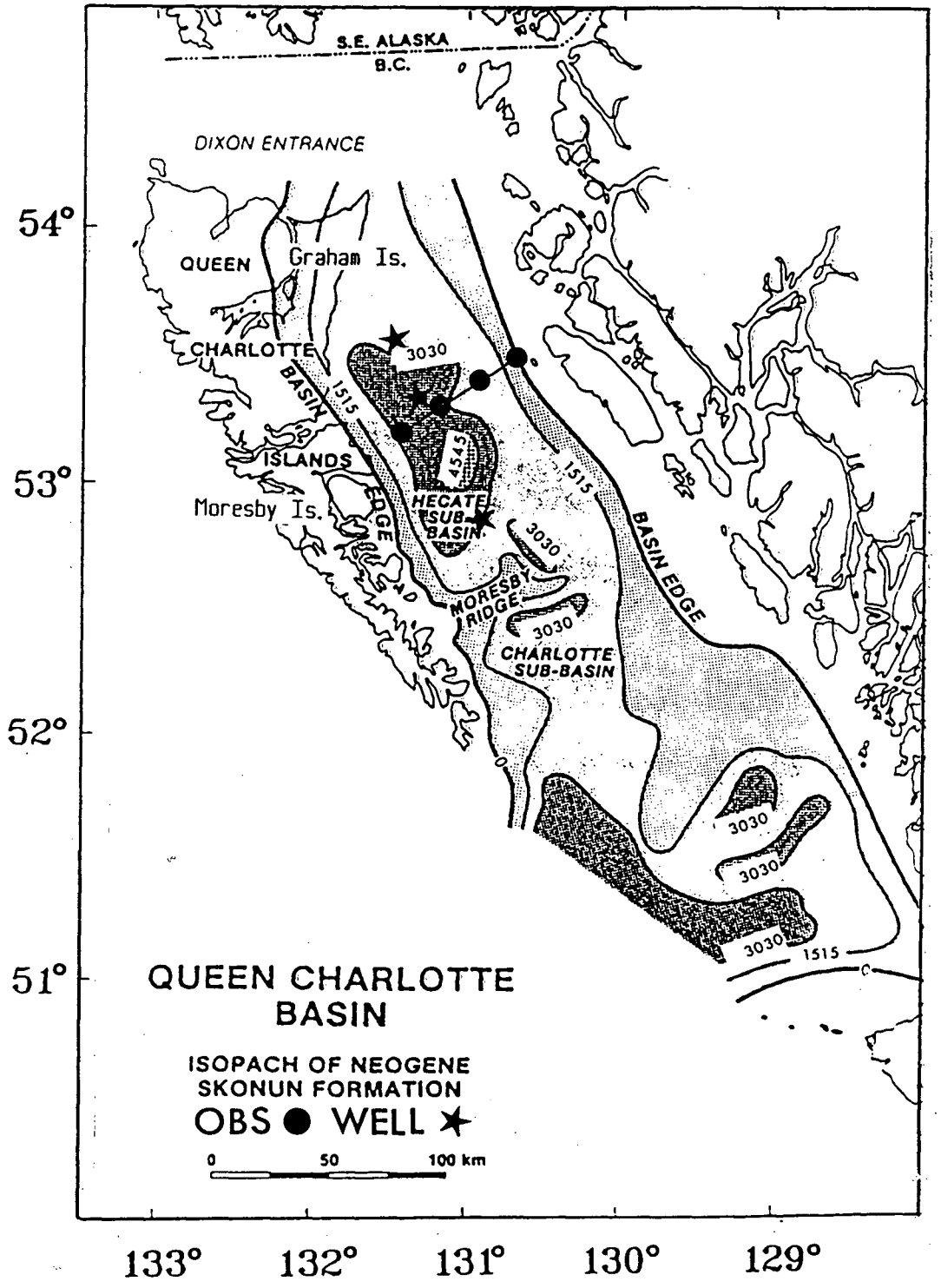

Figure 1.5 Isopach of the Tertiary Skonun sediments for the Queen Charlotte Basin (after Shouldice, 1971, 1973). Location of the airgun/OBS survey and the three nearest wells is also indicated.

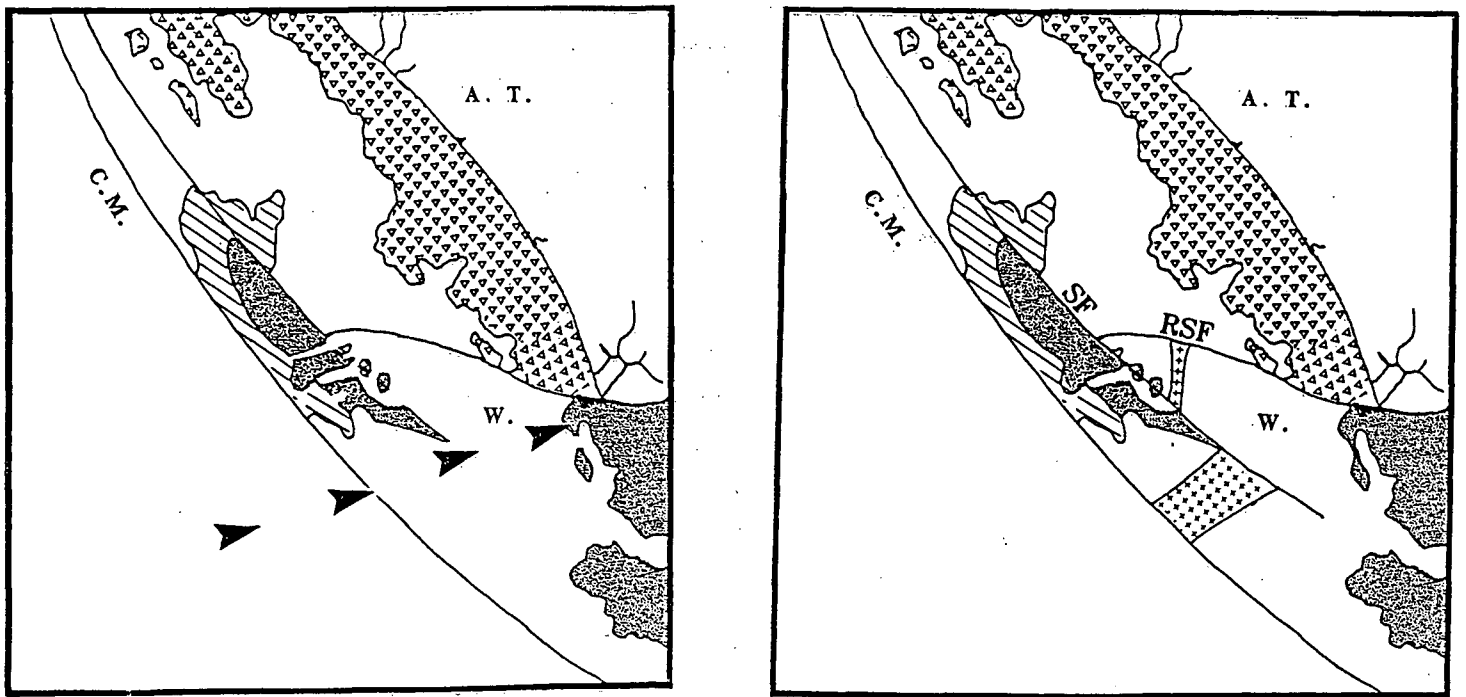

A. 20 TO 17 MILLION YEARS AGO

B. ABOUT 17 MILLION YEARS AGO

Alexander Terrane (A.T.) – Paleozoic rocks

Wrangellia (W.) – Mesozoic rocks

Rift zones

Trace of Anahim Hot Spot

C. M. Continental Margin

RSF Rennel Sound Fault

SF Sandspit Fault

Figure 1.6 Rifting sequence for the Queen Charlotte Basin (after Yorath and Cameron, 1982).

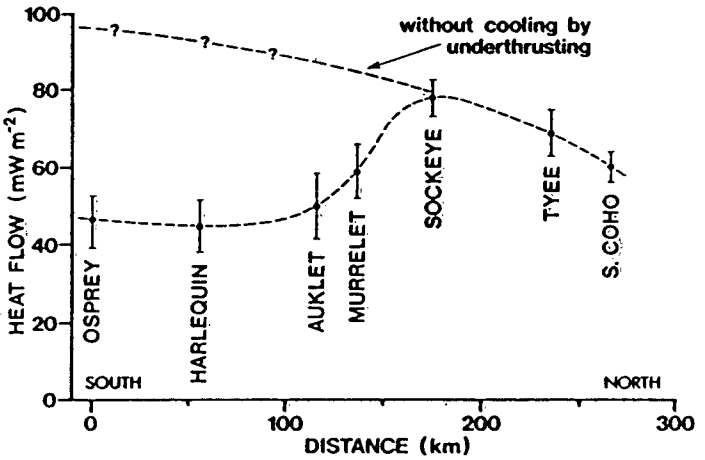

Figure 1.7 Estimated present heat flow based on down hole temperature measurements and thermal conductivities computed from porosity and mineralogy data from the Queen Charlotte Basin offshore wells. The dashed curve of higher heat flow for the southern wells is a possible profile if no underthrust cooling had occurred (after Yorath and Hyndman, 1983).

Yorath and Hyndham (1983) have interpreted the subsidence curves for all the offshore wells drilled in Queen Charlotte basin. Present depths to biostratigraphic horizons were converted to a basement subsidence history through corrections for sediment compaction and paleowater depths. The sediment compaction correction was derived using an exponential approximation of the decrease in porosity with depth. Tectonic subsidence curves were then estimated, thus correcting for sediment loading. The major uncertainty in their interpretation is in the biostratigraphic data reported by Shouldice (1971).

The tectonic curves first showed uplift, which resulted in the unconformity, at the end of the Late Miocene or Early Pliocene. Then 6 Ma ago there was a sudden onset of subsidence which has continued at a decreasing rate to the present. The Queen Charlotte Islands appear to have been uplifted and eroded, particularly on the west coast of the islands. The flexural model developed to explain this second stage of subsidence is based upon the assumption of oblique convergence at the North American continental margin. The subsidence due to the flexural downwarping was further amplified by sediment loading. The Oshawa rise, west of the islands, and the missing Upper Miocene and Pliocene sediments on Graham Island west of the hinge line where subsidence is balanced by uplift are cited by Yorath and Hyndman (1983) in support of this model.

1.3 Stratigraphy

Much of the information on the Neogene Skonun succession was obtained from the exploratory wells drilled on northeastern Graham Island by Richfield Oil Corporation and in Hecate Strait and Queen Charlotte Sound by Shell Canada Ltd. The location of the wells is shown on the map in Figure 1.1 and a cross section derived from the

well data is depicted in Figure 1.8. There are several striking features evident on the cross section. As already noted, there are several smaller basins within the Queen Charlotte basin that are controlled by the unconformity at the base of the Tertiary Skonun sediments. In the central part of Hecate Strait, the Moresby Ridge, between the Sockeye and Murrelet wells, separates the main part of the Queen Charlotte basin into the Hecate sub-basin and the Charlotte sub-basin (Figure 1.5). The Tertiary sediments are primarily non-marine in the Hecate sub-basin and marine to the south in the Queen Charlotte sub-basin.

Within the Hecate sub-basin, the major source was probably the Coast Mountains with small contributions from the Queen Charlotte Islands (Young, 1981). The Charlotte sub-basin, of marine Lower Miocene - Upper Pliocene succession, was probably deposited in water depths ranging from shallow to deep (0–50m to 200–1000m) based on biostratigraphic information.

Underlying the Tertiary Skonun sediments and Masset volcanics are the Skidegate Formation conformably resting on the Honna formation. The two formations represent the upper and middle units of the Queen Charlotte Group (Sutherland Brown, 1968); they are included in the post suture assemblage of Yorath and Chase (1981). The Honna Formation consists of conglomerate and coarse arkasic sandstone with minor shale or siltstone. The Skidegate Formation consists of fine grained detrital rocks, siltstone, silty shale, fine to medium sandstone and calcareous shale and sandstone. Both formations are estimated to be Late Cretaceous in age with a combined thickness ranging between 800 to 2100 m.

Beneath the Queen Charlotte Group, within Wrangellia, the Kunga, Maude and Yakoun Formations locally contain significant quantities of heavy fraction hydrocarbons locally on the Queen Charlotte Islands. The Kunga Formation is primarily composed

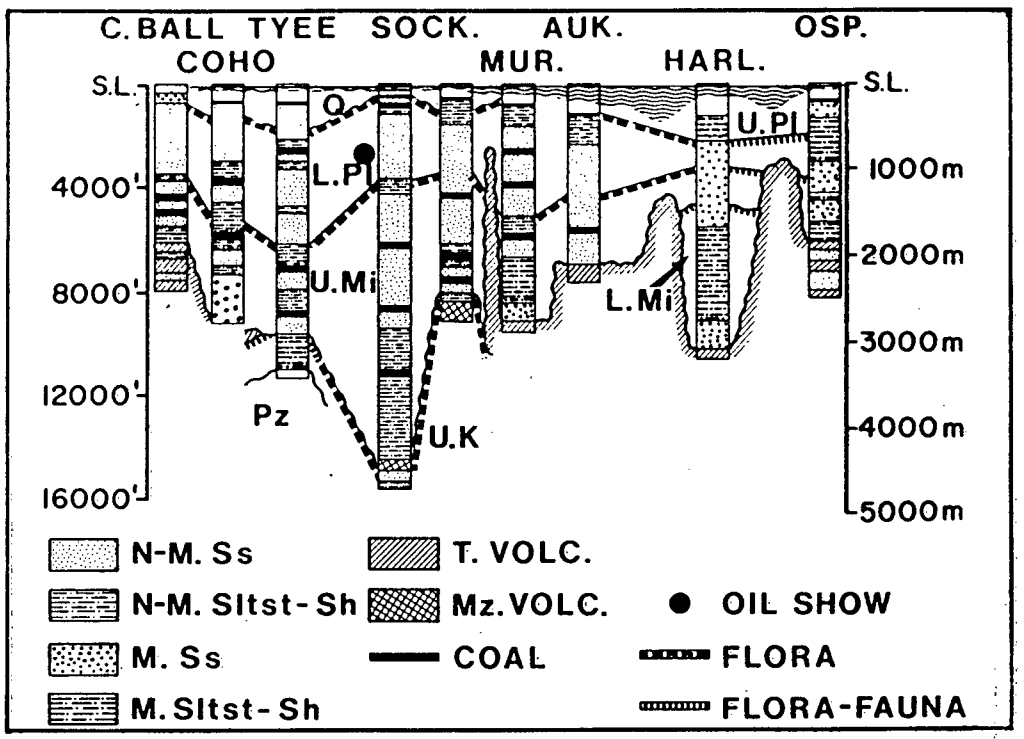

Figure 1.8 Cross section for the offshore wells drilled by Shell Canada Ltd. showing the unconformity controlling the basin. Stratigraphic correlations are based upon flora and fauna from well cores (after Shouldice, 1971, 1973).

of limestone and argillite with its age ranging from Early Upper Triassic to mid Lower Jurassic. The Maude Formation, where present, rests conformably on the Kunga Formation and is composed of argillite, shale, calcareous shale and lithic sandstone. The contact with the Kunga Formation is gradational, extending over many meters. The age of the Formation is estimated to be Late Jurassic with a total thickness of 225 m. It is seen on the southeastern portion of Graham Island, northeastern Moresby Island and Lyell Island. The Yakoun Formation contains some non-marine, as well as marine sediments. The formation consists primarily of pyroclastic rocks, many of which are formed largely of porphyritic andesite. It also includes volcanic sandstone, some conglomerate, shale, siltstone and minor coal. The age of the formation is between Middle Jurassic and earliest Upper Jurassic. Sutherland Brown (1968) described the volcanic cones which rose above sea level during this period to have once been clothed in lush Jurassic forests. The total thickness is approximatley 900 m. Table 1 of Appendix I summarizes each formation's lithology, age and thickness.

1.3.1 Hydrocarbon potential for the major stratigraphic units

The Upper Triassic and Jurassic rocks of Wrangellia, the Kunga, Maude and Yakoun formations, are the most favourable prospect for hydrocarbon generation. These are the Kunga, Maude and Yakoun Formations. In some places, Yorath and Cameron (1982) report that these rocks have been described as oil shales. Offshore, they probably occur at considerable depths but the oil may have migrated along faults into either the Upper Cretaceous sediments or the Tertiary sediments. The Cretaceous Honna Formation has good porosity and fair permeability (Shouldice, 1971, 1973) and is thought to be a good reservoir rock. The Tertiary sediments contain the necessary stratigraphic and structural traps for containing the oil which may have migrated into these sediments.

Another source of oil may be from the Tertiary sediments within the rift zones (Figure 1.6). If the increased heat flow seen in the wells (Figure 1.7) was higher in the past, oil may have been generated. The heat flux is certainly sufficient to have produced more than an immature gas. However if the heat flow was too high for too long, only dry gas would have been generated (Yorath and Cameron, 1982).

Below the Hecate sub-basin north of the suture zone, the Alexander Terrane rocks are not known to contain hydrocarbons. Therefore, only the Tertiary rocks could have generated oil. However, the geothermal gradients are thought to have been normal, as no rifting occurred in the Hecate sub-basin and only small amounts of immature gas may be expected (Yorath and Cameron, 1982). The lack of a sufficient thickness for the sediments combined with their primarily non-marine composition would further support this conclusion.

Another prospect, albeit costly, exists within the Cretaceous sediments which lie beneath the Tertiary lavas. Exploration, using conventional seismic reflection techniques, would be difficult as the volcanic rocks present a strong acoustic barrier to adequate penetration of sound waves. The Tertiary volcanics are known to thin and disappear in some locations (Figure 1.9; Shouldice 1971, 1973), which may aid in the exploration of this stratigraphic zone.

1.4 An Outline of The Seismic Refraction Study

The refraction experiment was designed to determine the seismic velocity structure of the Hecate sub-basin, particularly below the Tertiary sediments where the thickness of the Masset volcanics was unknown. Also, the existence or not of sediments below the volcanics was important to evaluate this region for any further exploration programs.

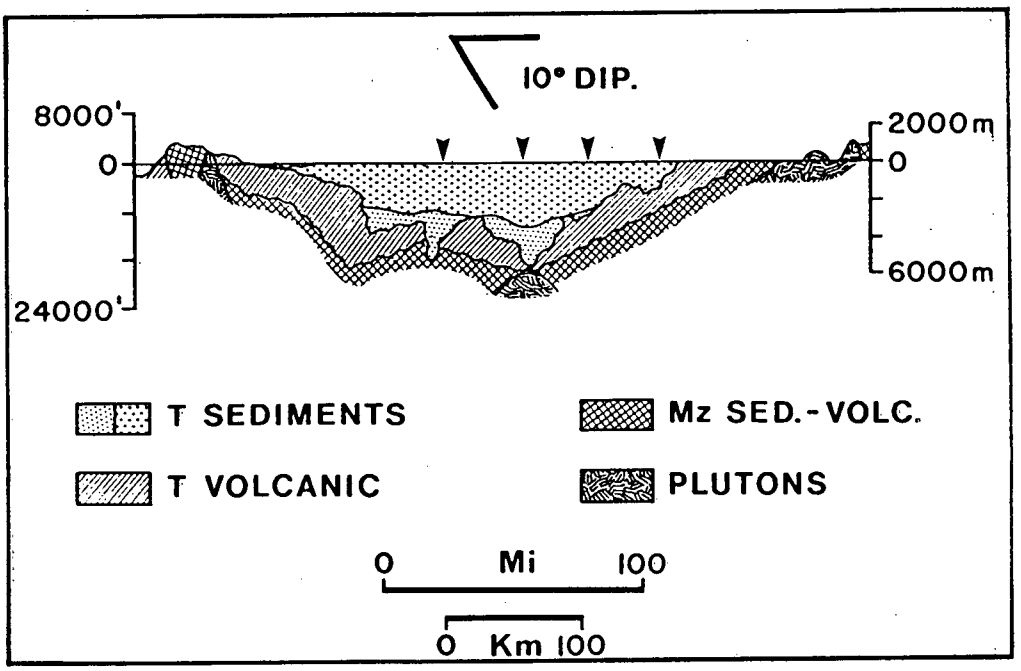

Figure 1.9 Structural geological model inferred from the cross section in figure 1.8, industry seismic reflection and refraction data and gravity and magnetics. Projected position of the four OBSs is indicated by arrows (after Shouldice, 1973).

The initial model, inferred by Shouldice (1971, 1973) from well data and available geophysical data, is shown in Figure 1.9. The upper boundary and even the presence of the Mesozoic sediments and volcanics is poorly defined beneath the Hecate sub-basin. The position of this unit in Figure 1.9 is based upon limited well log information and outcrops seen on the land on either side of the basin.

To verify and/or modify the model of Figure 1.9, an airgun/OBS survey was carried out in 1983. Four OBSs were deployed at 20 km intervals across Hecate Strait; airgun shots at about 0.2 km spacings were recorded to provide three reversed profiles extending over 60 km. Chapter II gives the details of the data acquisition and analysis procedures. In Chapter IV, the record sections and their interpretation through comparisons with theoretical sections for 2-D velocity models are described. The three sub-models resulting from interpretation of the individual reversed profiles are composited to provide a complete model across the basin. A discussion of the reliability of this model and its relationship to the local geology for the Hecate sub-basin are provided in Chapter V.

Chapter III contains an additional component to this thesis – the development of an interactive procedure for inversion of refraction data by wavefield continuation. The theoretical basis is outlined and and its application to the synthetic and real data of Chapter IV is shown.

CHAPTER II DATA ACQUISITION AND ANALYSIS

2.1 Data Acquisition

2.1.1 Airgun–OBS experiment

The airgun/ocean bottom seismograph (OBS) refraction program in Hecate Strait was undertaken as one component of a larger refraction program. In cooperation with the Earth Physics Branch (EPB) and the Pacific Geoscience Center (PGC), the University of British Columbia carried out an onshore-offshore refraction program during August, 1983. This large 330 km profile was recorded from the deep ocean across northern Moresby Island and Hecate Strait, to the mainland of British Columbia. Seventeen seismographs were deployed: 11 land based seismographs and six OBSs; and two energy sources were employed: TNT explosives and an airgun. The objective of this thesis was to investigate the upper 6 km of the crust beneath Hecate Strait. The data, recorded on the four OBSs deployed across Hecate Strait using a 32 litre ($2000 in^3$) airgun source, were utilized to develop a seismic velocity structural model to meet this objective. The location and plan of the airgun/OBS experiment is shown in Figure 2.1.

2.1.2 Description of the OBSs and the airgun

The OBSs were built at UBC and followed the design used by Atlantic Geoscience Center (Heffler and Barrett, 1979) with some minor modifications incorporated during construction. The OBS consists of four main components: (1) the delivery system comprised of a glass flotation sphere, a pressure case and an anchor; (2) the seismic wave detection system represented by a vertical and a horizontal gimbaled 4.5 Hz geophone

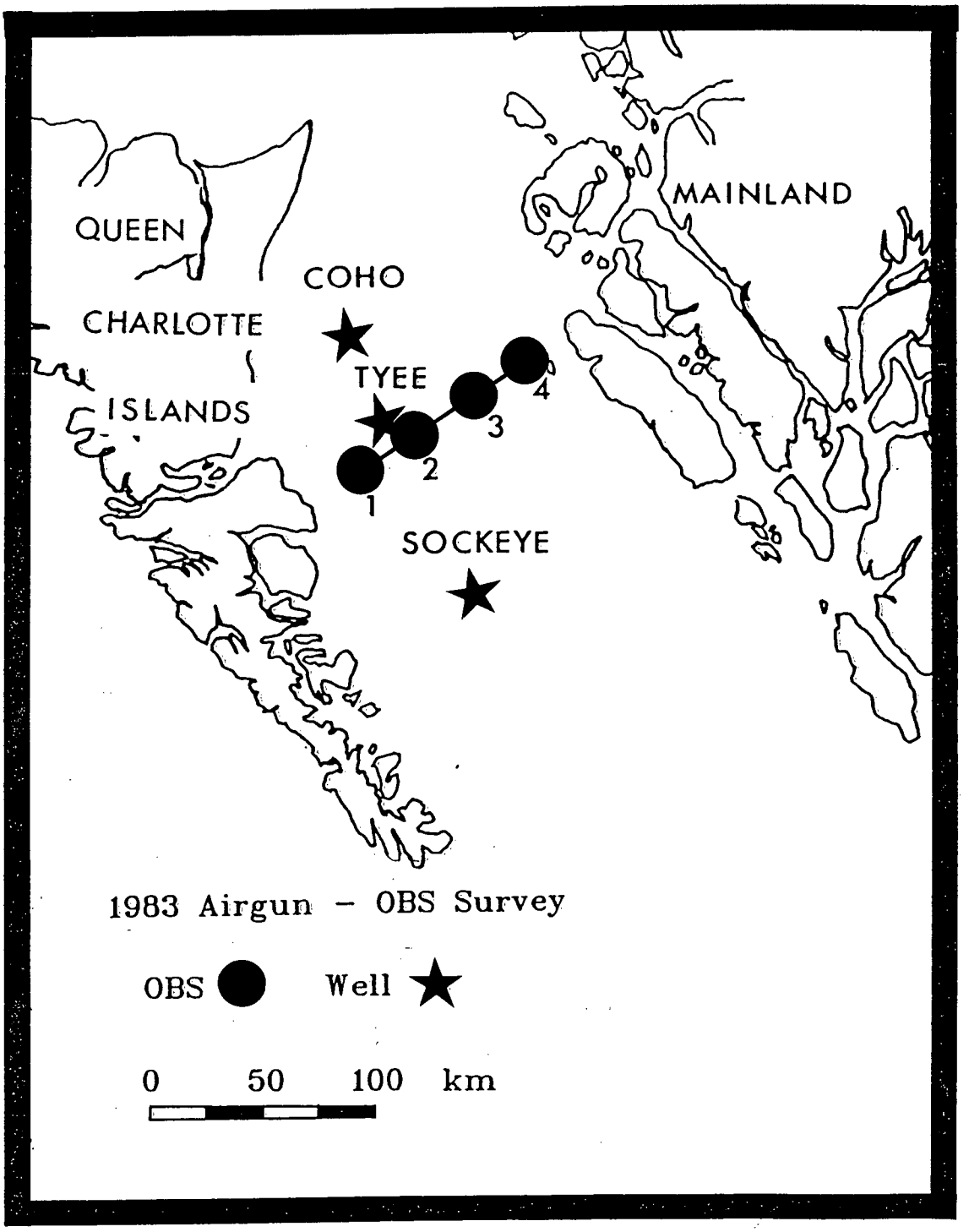

Figure 2.1 Location and plan of the 1983 airgun/OBS survey. OBSs are indicated by darkened circles numbered 1 to 4 and the Coho, Tyee and Sockeye wells are marked by stars.

housed within the pressure case, and a hydrophone, mounted on the side of the flotation sphere; (3) the recording system which uses a four channel slow speed direct record tape unit to store the amplified signal from the two geophones and hydrophone; (4) the clock, rated against WWVB at the time of deployment and recovery, generates a 10 Hz amplitude modulated time code. The operation of the OBS is governed by a microprocessor and the signals from the three components along with the time code were recorded on cassette tape. The passband of the OBSs lies between 4.5 and 30 Hz (Clowes, 1985). The seismic source was a 32 litre ($2000in^3$) airgun which provided energy equivalent to about 4 kg within the seismic passband. The airgun firing was controlled by a microprocessor which triggered the airgun at one minute intervals using a clock which was rated against WWVB time code at the start of the shooting.

2.1.3 Description of the procedure

The OBSs were deployed at approximately 20 km spacing across Hecate Strait in water depths ranging from 22 m for OBS 1 in the west to 162 m for OBS 4 in the east (Figure 2.1). The depths were determined using the ship's depth sounding system as recorded on an EPC line scan recorder. The latitudes and longitudes were derived from readings of the ship's principal navigation system, Loran C, at the time of deployment. Table 2.1 lists the depth and position for each OBS.

The ship started from the point of deployment of OBS 4 in the west. The airgun was towed behind the ship at a depth of 18 metres until it neared OBS 2, where the depth was decreased to 14 m for the remaining portion of the profile. This firing rate of one minute, combined with the ship's speed, resulted in a source interval spacing

OBS	*LOCATION (N. Long. : W. Lat.)*	*DEPTH*	*AIRGUN DEPTH*
1	*53.005 : 131.4616*	*22*	*14*
2	*53.3002 : 131.2342*	*32*	*14*
3	*53.3060 : 130.9579*	*122*	*18*
4	*53.5153 : 130.7155*	*163*	*18*

Table 2.1 OBS location and depth and depth of airgun (depths are given in meters).

of approximately 160 m. Reversed profiles for segments of the airgun line between neighbouring OBSs arose naturally from the design of the experiment.

2.2 Data Processing

2.2.1 Digitizing, editing and demultiplexing the analog data

The direct record cassette tapes were digitized using the PDP11/34-based analog-to-digital conversion facility. The data were converted at a 120 Hz sampling rate with variations in analog tape speed taken into account. The digitized data were then edited into 25 segments centred about the largest automatically detectable event within each 60 s recording interval. The time of first sample for each event was determined with the aid of a computer program which keyed on the OBS time code. The time code was not explicitly read because the high pass band response of the hydrophone to the water wave had been cross-fed to the time code channel. This facilitated the water wave recognition, but interfered with the time code signal over a range of data points. This

problem was circumvented by detecting only minute marks, keeping track of the time to the point where the edited data segments began, and then skipping over the requisite number of data blocks to bypass the water wave interference. The edited data were then demultiplexed and converted to an IBM-compatible format for plotting.

2.2.2 Basic timing and positioning

Corrections were applied to the time of the first sample of each seismogram for drift in the OBS and airgun clocks relative to WWVB, delay in the actual firing of the airgun after the trigger pulse and adjustments for the skewness of the recording head. Ship positions were determined by Loran C readings logged at 10 minute intervals.

2.2.3 Special positioning and related timing corrections

The navigation data show that the shot line did not pass directly over the OBSs nor did the nearest offset, as defined by these data, agree with the offset as determined from first arrival observations. To enable compilation of the seismic data into appropriate record sections for which 2-D profile recording is assumed, distance and time corrections were required. Also, the most accurate data from which shot-receiver distances can be determined is the first arrival and/or direct water wave arrival on the seismograms, rather than interpolated navigation positions. A full description of the timing and positioning corrections along with a complete set of navigation and time of first sample tables is given in Clowes (1985). The special positioning and timing will be restated here as they represent adjustments which influence all the traces particularly for the source/receiver distances that are less than 2.0 km where inline corrections are most noticeable.

Corrections for shot/receiver positions and distances were made in three stages, and necessitated a corresponding adjustment to traveltimes. The first stage made use of the navigation data to place the shots and OBSs approximately in line and provide the usual trace spacing associated with a one minute firing interval. Simple planar geometry was used to project the OBS positions onto the shot line.

The revised (shortened) shot receiver distances did require that a corresponding travel time correction for the extra travel path be removed. This was the substance of the second stage which used first arrivals to determine the travel times to the OBSs. Direct water waves were not in fact the first arrivals, even at short distances, due to the effects of the shallow water and refraction through the sub bottom. Consequently, a two-layer model (water plus sub bottom, for which the approximate velocity was determined from first arrival data) was used to determine the best projected location of the OBSs relative to the shots along the profile. This was accomplished by iterative adjustments of calculated intercepts to agree with measured travel times. Knowing the depth of the OBS and the depth of the water below the airgun (from 3.5 kHz profiling), which was nearly constant for a few kilometers on either side of the OBSs, a simple calculation using Pythagoras' theorem enabled determination of the appropriate time correction. The time corrections applied to each OBS amounted to less than 0.45 s for the OBS requiring the largest inline correction at zero offset. At 1 km offset this correction (which was for OBS 2) had dropped to 0.11 s. These inline timing corrections were generally less for the other three OBSs and were large compared to the picking of first breaks. However, the large shifts do not correspond to a large uncertainty in first arrival picks for the affected traces but do affect secondary arrival positions, rendering them unreliable where the corrections were large (less than 1 km source/receiver distance). Secondary arrivals were only modelled beyond the 5 km range where the corrections

for travel time were not significant. This was borne out in the comparison of velocities determined from the corrected traces (2.0 km/s) versus velocities derived from some well logs in the area which yielded velocities of 2.17 km/s at 300 m depths. Details of the calculations can be found in Clowes (1985). The time correction is only applied to the plotting parameter which controls the sample representing zero time.

The third stage involved a simple lateral shift to produce agreement between the nearest offset based upon navigation and the nearest offset based upon observed data. Although the relative accuracy of Loran C is approximately + or - 200 m in far offshore regions, it may deteriorate near station locations in near shore areas. Furthermore, there was no check for lane jumps which can result in 1 to 2 kilometer errors in the relative position of the ship. To determine the lateral shift, two methods were applied; one which uses the velocity, and one which used the predicted time-distance intercept for a two layer model. Table 2.2 contains a summary of the positioning corrections for each OBS. The details of the calculations for the lateral shift are given in Clowes (1985). Appendix II contains all the corrected sections plotted in variable area format.

	OFFLINE CORRECTION (km)		
OBS	*NAVIGATION BASED*	*ARRIVAL BASED*	*LATERAL SHIFT (km)*
1	*0.810*	*0.190*	*0.995*
2	*1.170*	*0.619*	*1.156*
3	*0.460*	*0.124*	*1.990*
4	*0.656*	*0.154*	*1.160*

Table 2.2 OBS positioning corrections.

2.3 Data Analysis and Interpretation Procedures

2.3.1 Data analysis

The frequency content of the seismic signal and noise recorded on an OBS is illustrated by the power spectra shown in Figure 2.2 . The signal-to-noise ratio for the record sections was very good and only certain cases required the use of filtered record sections. The noise is concentrated in two bands (Figure 2.2a), the 14 to 24 Hz frequency band and the 0 to 5 Hz frequency band. There is also noise present in the 5 to 12 Hz frequency band but, as illustrated in Figure 2.2b, the signal contains more power than the noise for most cases. However, sometimes noise obscures any recorded seismic signal as shown in Figure 2.3a for OBS 4 hydrophone component. In this case filtering within the seismic passband proved helpful. Figure 2.3b shows the same data (plotted using the same scale factors) after bandpass filtering between 5 and 12 Hz. An event parallel to the distance axis at about 1.8 s is now distinguishable. Arrows highlighting the event were purposely omitted to permit the reader to judge the results without too much bias from the author. This particular example proved to be a valuable guide in the eventual interpretation of the data recorded on the vertical and horizontal channels of OBS 4.

2.3.2 Interpretation procedures

The record sections in Appendix II are in a form ready for interpretation. Conventional interpretation of refraction data usually involves a forward model in the form of two-dimensional modelling schemes. The process begins by determining a starting model, usually based upon a dipping layered model derived from straight line fits to

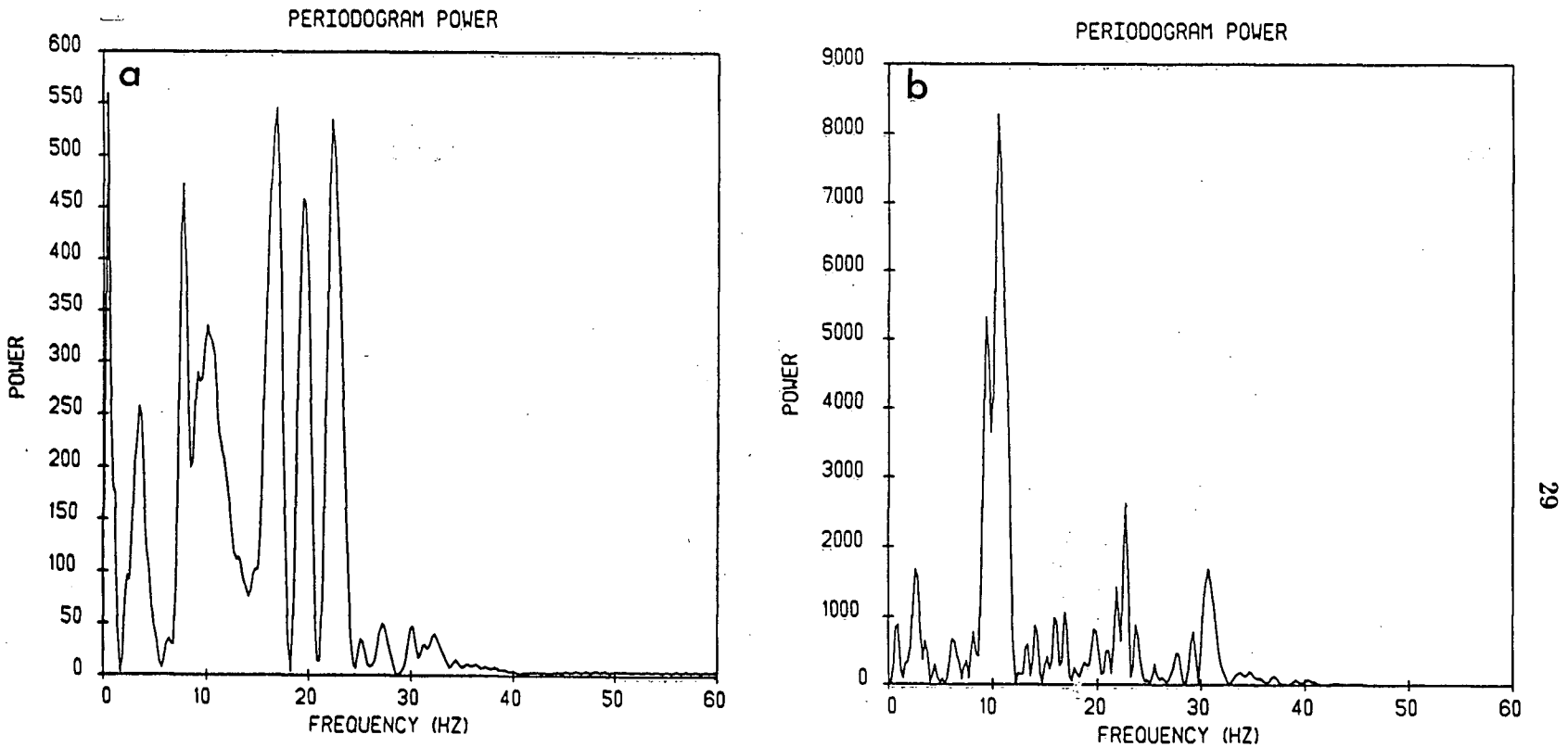

Figure 2.2 Power spectra (a) background noise (b) signal + noise for OBS 3. Periodograms were computed over two second window (see text for explanation).

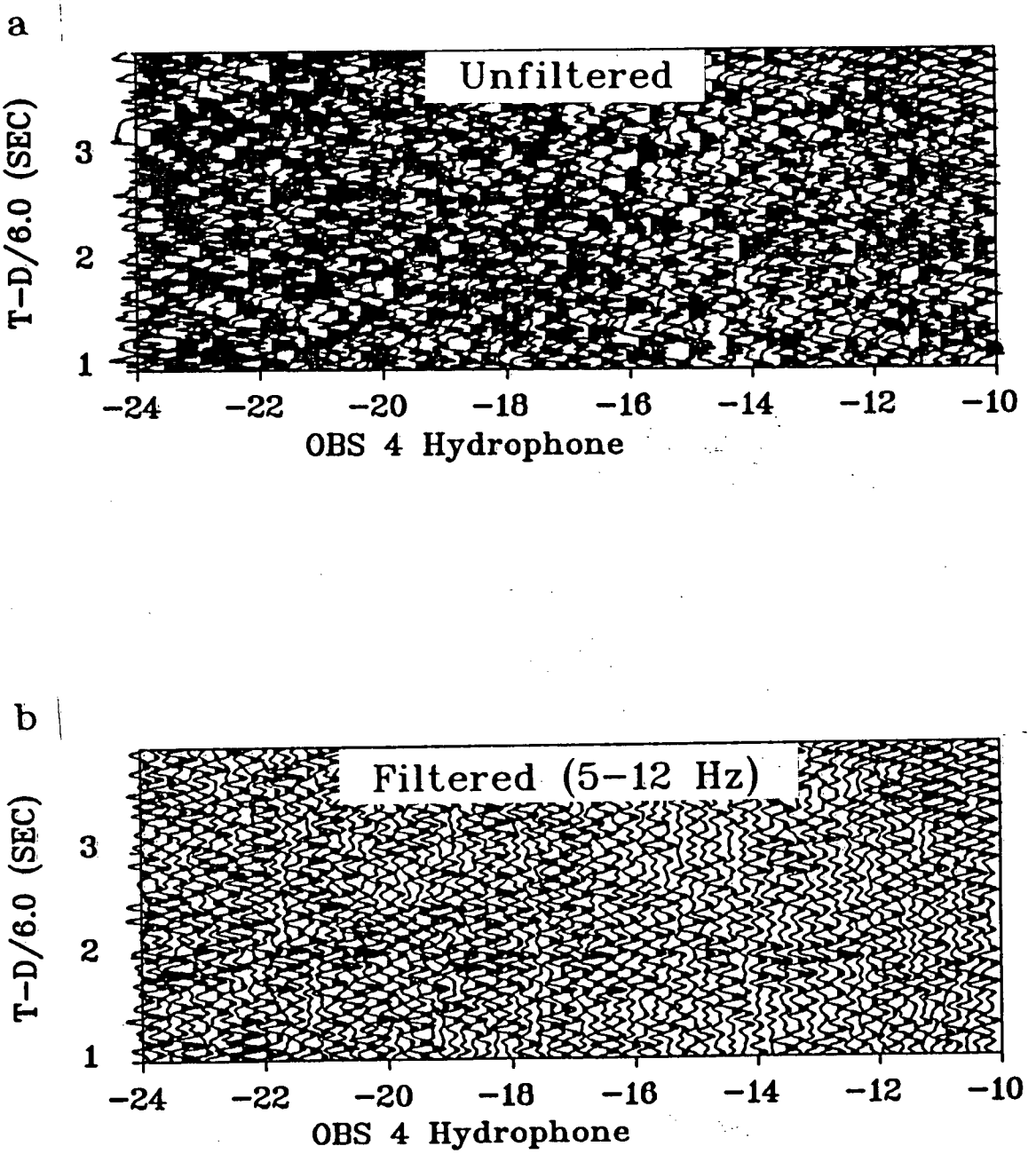

Figure 2.3 Comparison of unfiltered (a) and filtered (b) record sections for OBS 4 hydrophone. The record sections are plotted with the same scale factors The filter used for (b) was a 5–12 Hz bandpass filter.

forward and reversed travel times of the primary arrivals. The starting model may also be derived from models obtained in other experiments near the area of investigation. The initial model is then perturbed by adjusting its parameters to achieve a closer fit between the computed travel times through the model, and the observed travel times, based upon primary arrival events. This procedure is inherently non-unique, but may be constrained by adherence to other information gathered from wells drilled near the area of study, other seismic data and/or models and the regional geology of the area. A further refinement to the final travel time models may be accomplished by the modelling of the observed amplitudes in the record section. Models are very sensitive to changes in amplitude and care must be taken when comparing modelled amplitudes with observed amplitudes where the data have been compiled from many different receivers and/or sources. Furthermore, any positioning and timing corrections applied to traces, such as in-line corrections, do not include corrections for the amplitude of the shifted arrival.

The data in the present study were compiled in a common receiver format from a stable consistent source, which lends itself well to amplitude modelling. The inline corrections applied to the data preclude reliable amplitude modelling of arrivals within 4 km of the OBS. The interpretation of the data in this study employed a two-dimensional ray tracing routine developed at UBC (Spence, Whittall and Clowes, 1984). The computed travel times may be compared with those picked from the data by directly overlaying the computed values onto the observed data. The advantage of directly overlaying the data with the computed travel time curve is that the computed results can be compared in the context of the entire record section. Valuable insights can result from following this procedure as the interpreter is constantly reminded of other trends which may exist in the data. This is not the case when travel times are read into the program since the interpreter is then concerned with fitting only an isolated set of points. This idea is

not new to refraction modelling, since in refraction interpretation, particularly for poor data, the interpreter will often return to the data after gaining a clearer insight into the structure under investigation and repick the first arrivals.

To refine the model derived from the travel-time fit to the data, theoretical seismograms were calculated for the theoretical travel-time curves. Relative amplitudes across the synthetic record section were visually compared to the observed amplitudes. Amplitudes are particularly sensitive to velocity gradients and this feature provided additional control on the choice of velocity gradients for the model. Velocity gradients for the various layers in the model were altered until the amplitudes for the theoretical seismograms matched those in the data. Amplitude modelling also provided critical information for the analysis of particular phases observed in the data.

An alternative method for determining a 1-D velocity-depth structure directly from data sections was presented by Clayton and McMechan (1981). The author followed their procedure and developed an interactive computer program to implement the method. The work represents a new development at UBC. It also provides examples additional to, and different from, those illustrated in the original paper and insight into the effects of applying a 1–D interpretation to a data set which clearly represents a 2–D structure. Therefore, the method and its application to the airgun/OBS refraction data from Hecate Strait will be described in the next chapter.

CHAPTER III INVERSION BY WAVEFIELD CONTINUATION

3.1 Introduction

Inversion by wavefield continuation is an image analysis procedure by which a 1-D velocity-versus-depth structure can be extracted directly from a seismic record section. This is accomplished by projecting the observed wavefield, as represented by arrivals recorded at increasing offsets, back to zero offset. This backward projected wavefield then represents the arrival of wavefronts as a function of two-way travel time at the surface. This delay time function for the arrivals, along with the known stacking lines along which the backward projection was carried, may then be utilized to downward project the wavefield at the surface to the appropriate slowness medium from which it originated. The practical application of this method proceeds through two linear transformations; a slant stack (the back projection) and a downward continuation (the downward projected wavefield).

The inversion of refraction data by wavefield continuation has the desirable quality of an unbiased inversion, with the exception of the final velocity depth-pick. The observed data represent the input required by the program and the velocity depth function is obtained directly from the imaged wavefield.

Inversion of refraction data by wavefield continuation has been applied to real data examples exhibiting weak lateral velocity variations (Clayton and McMechan, 1981). The theory is based upon the solution to the one dimensional wave equation for the 1-D velocity versus depth model. Clayton and McMechan (1981) demonstrated the robustness of the algorithm in the treatment of earth models with weak two dimensional velocity structures.

A computer program based upon the theory as presented by Clayton and McMechan (1981) has been written with two objectives in mind : (1) to test the applicability of the procedure for examples with a greater degree of of lateral heterogeneity; and (2) to apply the procedure to a selected segment of the airgun/OBS data set for the purpose of comparing the results with those obtained from the 2–D modelling interpretation in Chapter IV. The data under investigation in this thesis offer an ideal opportunity to meet these objectives for two reasons. First, the data set satisfies the basic assumptions outlined in the development of the theory. Secondly, the data have been fully interpreted using the UBC 2–D ray tracing scheme (Spence, Whittall and Clowes, 1985). Therefore the resulting inversion, involving comparison of theoretical and observed seismograms, may be evaluated based upon these 2–D results.

Other inversion procedures will not be investigated as they are beyond the scope of this thesis. The reader is referred to various papers by Bessonova *et al.* (1974, 1976); Garmany *et al.* (1979); Wenzel *et al.* (1982); Carrion *et al.* (1984) and many others for more thorough discussions concerning the inversion of refraction data. The following development was undertaken as a separate study of interest, subsequent to results derived from the 2-D modelling interpretation described in Chapter IV.

3.2 The Linear Transformations

3.2.1 The slant stack procedure

To obtain the slant stack, the amplitudes are summed along lines of constant slope and intercept; the wavefield is then constructed by sweeping through all slopes and intercepts on a seismic record section. The slope of the line in the traveltime–offset

(t-x) domain is the inverse of the velocity $(\frac{1}{v})$, also known as the ray parameter p; the intercept is the two-way travel time at zero offset, usually referred to as τ. The amplitude summed along lines of constant slope p and intercept τ is then stored or plotted at its new coordinates (p, τ).

Having described how the slant stack is performed, it may not be apparent how it arises. An understanding of the slant stack procedure can be attained by considering the seismogram presentation itself. A function P(t,x), where P represents the amplitude at the point (t,x) in the $t - x$ domain can be defined. A straight line through these points, defined by

$$t = \tau_1 + p_1 x, \tag{3.1}$$

describes the travel time for points along the line. If this line intercepts an arrival, then the travel time to a receiver at an offset of x can be determined. Furthermore, this arrival also has a velocity in the form of the slope of the line through that point. However, this does not have much significance since a number of lines can pass through this arrival depending upon the choice of intercept and slope. The slant stack allows a weight to be attached to the arrival to determine the significance of the associated velocity. In practice this is done by redefining $P(t, x)$ by substituting t in (3.1) to obtain $P(\tau_1 + p_1 x, x)$ and then adding all the amplitude values which fall along the line defined by $\tau_1 + p_1 x$. This weighting function is defined by

$$S(\tau_1, p_1) = \sum_x P(\tau_1 + p_1 x, x), \tag{3.2}$$

and for a set of arrivals with the same apparent velocity as that of the slope of the line, S will add to large values while uncorrelated events will destructively interfere.

Weighting functions can be defined for the entire seismogram by varying both p and τ. This is the essence of the slant stack and in its practical form is given by

$$S(\tau, p) = \sum_{x} P(\tau + p\,x, x). \tag{3.3}$$

More formally stated, the slant stack is given by

$$S(p, \tau) = \int_{-\infty}^{+\infty} P(\tau + p\,x, x)\,dx. \tag{3.4}$$

where S is the $(p - \tau)$ wavefield.

The slant stack is more easily carried out in the time domain when trace spacing is not constant (McMechan and Ottolini, 1980). A correction for the frequency dependence of the stack must be made if waveforms are to be preserved. Phinney *et al.* (1981) showed how the frequency dependence arises through their derivation of the inverse slant stack. This dependence can be intuitively realized by considering that the summation of amplitudes along different portions of the wavelet, for many wavelets, effectively spreads the transformed wavelet. However, since the inversion scheme under consideration is only concerned with the tau curve described by the locus in the $\tau - p$ domain, this correction of the form $H(t)\,t^{-1/2}$ (Phinney *et al.*, 1981) need not be applied. Furthermore, the non-ideal 2-D case requires the slant stack and inversion to use all values of p along a particular raypath (Chapman,1981) which is beyond the scope of this study.

The slant stack decomposes the observed seismogram into its fixed p components which may then be downward continued separately. Figure 3.1a shows a theoretical seismic section generated from the asymptotic synthetic seismogram routine of Spence *et*

al. (1984) for a plane layered earth model with four layers. The four arrival branches can be seen in the theoretical seismogram. Only the refracted arrivals were considered; no precritical nor wide angle reflections were included. Table 3.1 shows the characteristics of the 1-D model.

LAYER	*DEPTH (km)*	*VELOCITY (km/s)*	*GRADIENT (km/s/km)*
I	*0.0*	*2.0*	*0.3*
II	*0.7*	*2.7*	*0.5*
III	*2.0*	*4.8*	*0.5*
IV	*4.0*	*6.0*	*0.3*

Table 3.1 1-D model used for inversion testing.

The arrivals from each layer have been labelled with the corresponding layer number in Figure 3.1a. The corresponding slant stacked arrival branches have been labelled by lower case roman numerals. If the arrival branches were represented by straight lines, each arrival branch would map to a point corresponding to the intercept and slope of the stacking line. However, extended loci of energy arise when extended wavelets are used and, as in this case, when the arrival branches possess curvature due to velocity gradients. The relationship between the branches and their transformed values can be easily seen. The layer I arrival branch transforms to the $p - \tau$ locus i which has its maximum energy concentrated at a point which represents the average velocity in the layer. Similar relationships can be seen for branches II and III . The last arrival branch (IV) was included to demonstrate the effects of stacking low amplitudes with apparent velocities close to a preceding branch. The rays bottoming in this layer are few and a correspondingly lower amplitude of their arrivals is indicated. The low gradient and

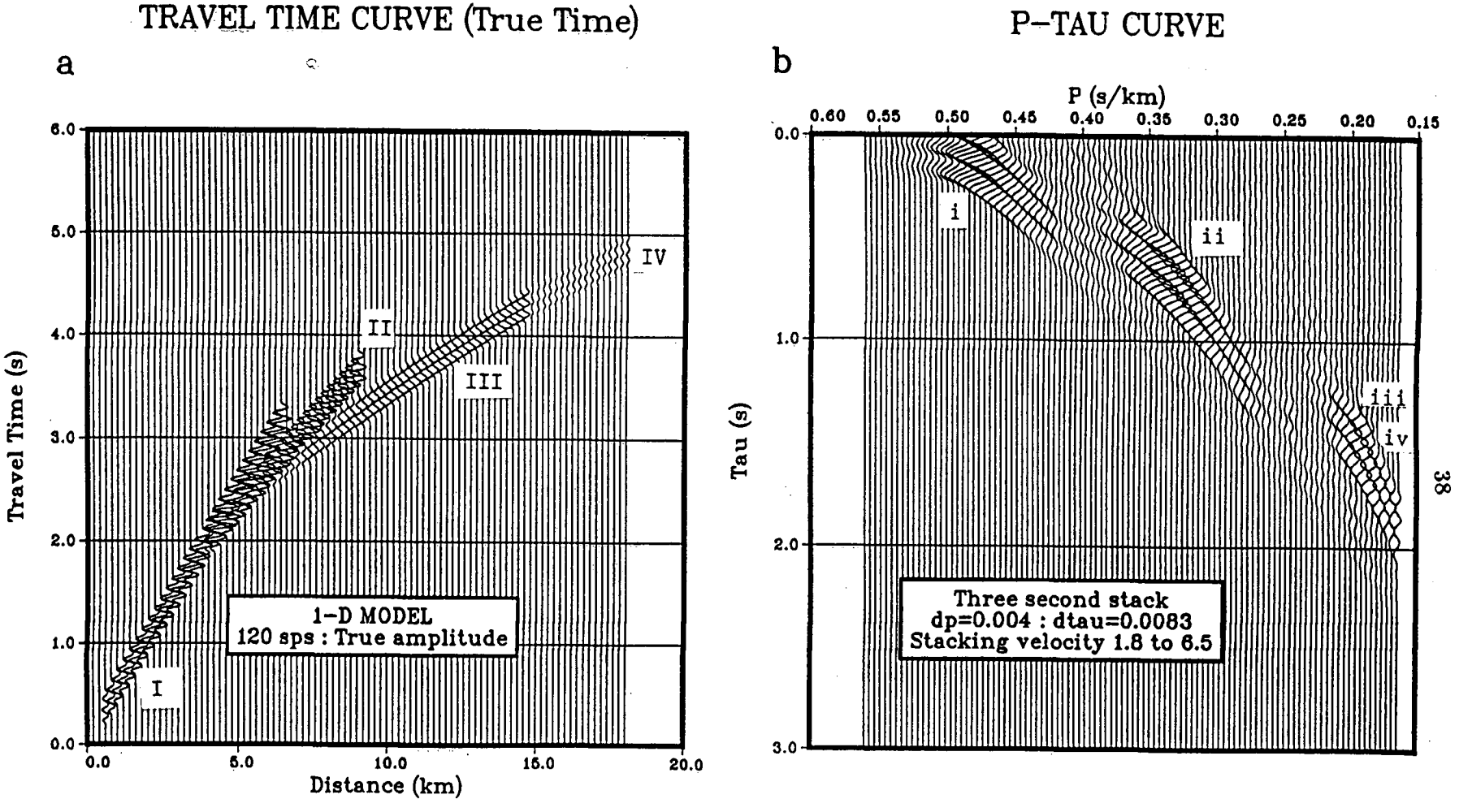

Figure 3.1 Slant stacked wavefield (b) for theoretical seismograms (a) computed for 1-D model in Table 3.1 . Lower case roman numerals are used to show the corresponding $p - \tau$ mapping for the equivalent arrivals identified by uppercase arrivals in (a). The slope for slant stack lines was incremented by 0.004 s/km and the intercept times were incremented by 0.0083 s or the reciprocal of the sampling rate (120sps). Stacking velocities ranged between 1.8 km/s and 6.5 km/s.

the far offset also affect the amplitude of these arrivals. When these amplitudes are summed, because no windowing was used, they are absorbed essentially by the effects from branch **III**. Thus, they are not clearly seen in the transformed wavefield. Where they should occur has been indicated by **iv**. They also have the effect of slightly lowering the amplitudes for the transformation of branch **III**. The artifacts seen as diagonal, low amplitude events running from left to right result from the finite aperture used, spatial aliasing and/or the lack of windowing the stack.

3.2.2 The downward continuation procedure

The development follows that of Clayton and McMechan (1981), except they implemented the downward continuation in the frequency domain, but following their recommendation, this study implements it in the time domain. The downward continuation is similiar to a depth migration but is applied in the offset domain as opposed to the common midpoint domain.

Claerbout (1976) and Gazdag (1978) show that the downward continuation of the wavefield observed at the surface can be implemented by a phase rotation in the frequency domain when the velocity varies only with depth. Writing the wave equation in the frequency domain gives

$$\left[\frac{\partial^2}{\partial z^2} + \frac{\partial^2}{\partial h^2} + 4\,\frac{\omega^2}{v^2(z)}\right] P(\omega, h, z) = 0.$$

The solution to this equation was given by Claerbout(1976) and Gazdag (1978)

$$P(\omega, k_h, z) = P(\omega, k_h, 0)\, \exp\left[-i\,2 \int_0^z \sqrt{\frac{\omega^2}{v^2(z)} - \frac{k_h^2}{4}}\, dz\right] \qquad (3.5)$$

where ω is the temporal frequency and k_h is the horizontal wavenumber. The first minus sign in equation 3.5 indicates that upcoming waves are being imaged.

The Fourier Central Slice theorem (Clayton and McMechan, 1981) is invoked to recast equation 3.4 in the frequency domain which demonstrates, more clearly, the relationship between equation 3.5 and the slant stack. Rewriting equation 3.4

$$S(\omega, p) = P(\omega, -2\omega p). \tag{3.6}$$

Equation 3.5 may then be converted to its slowness form by substituting $-2\omega p$ for k_h. Rewriting this equation yields

$$P(\omega, -2\omega p, z) = P(\omega, -2\omega p, 0)\, e^{-i\omega \Psi(p,z)}, \tag{3.7}$$

where

$$\Psi(p, z) = 2\int_0^z \sqrt{v^{-2}(z) - p^2}\, dz. \tag{3.8}$$

Using equation 3.6, equation 3.7 may be written as

$$S(\omega, p, z) = S(\omega, p, 0) e^{-i\omega \Psi(p,z)} \tag{3.9}$$

Inverse transforming this equation gives

$$S(\tau, p, z) = \int S(\omega, p, 0)\, e^{-i\omega[\Psi(p,z)-\tau]}\, d\omega. \tag{3.10}$$

This equation allows the specification of the $\tau - p$ wavefield at any depth z. $S(\omega, p, 0)$ is the slant stacked wavefield, obtained in section 3.2.1, which represents the delay time

function for upcoming waves at the surface. The exponential function is the downward continuation operator which is common in potential field analyses.

For the problem described, it is not necessary to have the wavefield for every depth z, only those depths satisfying the imaging condition for this problem must be met; the downward continuation process must stop when all plane wave components have reached their maximum depth of penetration or bottoming point. Mathematically, this occurs when $\tau = 0$ (the p of the ray equals the true slowness of the medium v^{-1}). Setting $\tau = 0$ in equation 3.10 yields

$$s(p,z) \equiv S(0,p,z) = \int S(\omega,p,0) e^{-i\,\omega\,\Psi(p,z)}\, d\omega, \tag{3.11}$$

where $s(p,z)$ is defined as the slowness plane.

Equation 3.11 is in the form utilized by Clayton and McMechan (1981) in their algorithm for implementation. Their program was run on an array processor but they suggest recasting equation 3.11 in the time domain for general purpose machines. The program written for this study uses the time domain representation of equation 3.11 which is given by

$$s(p,z) = S[\tau - \Psi(p,z), p, 0]. \tag{3.12}$$

Equation 3.12 arises by taking the first minus sign in equation 3.10 inside the brackets, using the shift rule (Chapman, 1978) and writing equation 3.12 directly. The domain in which equation 3.11 or 3.12 is applicable has a branch cut which is remedied by altering the definition of Ψ to

$$\Psi(p,z) = 2\int_0^z \left| v^{-2}(z) - p^2 \right|^{1/2} dz, \tag{3.13}$$

which prevents attenuation of the wavefield below depths where p is greater than v^{-1}.

As recommended by Clayton and McMechan (1981), a phase shift of $5\pi/4$ was then applied to the downward continued wavefield. This phase shift embodies three correction factors to compensate for (1) the far-field radiation condition (Aki and Richards, 1980, p 417); (2) the 2-D representation of wave propagation in three dimensions (Chapman, 1978); and (3) an average factor of $\pi/2$ to compensate for the range of reflection coefficients expected for reflections and refractions (Clayton and McMechan, 1981). This last point may cause confusion as reflection coefficients have been implied for refraction. The image formed by applying equation 3.11 is composed of wavelets whose shapes are defined by the phase shift associated with the reflection coefficient at each z (Clayton and McMechan, 1981). McMechan and Ottolini (1980) show that the $p-\tau$ curve for a refraction branch is formed by the envelope of $p-\tau$ curves for the reflections. Chapman (1978) also states that a refracted ray can be treated as having a reflection coefficient of $-isgn(\omega)$.

The downward continuation procedure represented by equations 3.11 and 3.12, with the phase shift applied, was implemented on the Amdahl 5850 computer at the UBC Computing Center. Since the downward continuation equation requires a velocity versus depth curve as an input, it is necessarily an iterative procedure. The program has been designed to automatically input an initial velocity versus depth curve for the downward continuation of the $p-\tau$ wavefield. The velocity versus depth curve used was 1.8 km/s for all depths. The downward continued wavefield is then displayed on the terminal. To operate the procedure in an interactive mode, a means of inputting the subsequent user picked velocity depth curves was required. The user obtained these new curves by picking points along the locus of maximum amplitude, now at minimum depth (z) in the downward continued wavefield or $p-z$ wavefield. This was implemented using the cross

hairs on the graphics terminal. The program instructs the computer to accept graphic input and the computer responds by displaying cross hairs. The user then positions the cross hairs over the desired amplitudes and hits any key to input the values. The picking session ends when the user selects a p value less than 0.55 s/km (this can be altered if required). The control then returns to the program which converts the picked p values to the velocities and resamples them at the desired sampling interval through a simple linear interpolation. This new curve is used to downward continue the original $p - \tau$ wavefield again. Thus, any new curve does not depend on the results of the previous curve since the program always returns to the original $p - \tau$ wavefield. The new $p - z$ wavefield is then displayed and the process can be continued. Usually 4 to 5 iterations are necessary to obtain a $p - z$ wavefield that converges to a single solution. The advantage of implementing the inversion in an interactive manner is that the resultant $p - z$ curve, for each downward continuation iteration, is immediately displayed. Hence, the user can quickly gain experience in interpreting the $p - z$ wavefields. Changes observed by the user in a short period can be better assimilated and an acceptable solution is reached sooner. Each p-depth curve is output to a file for later review.

3.3 Examples

McMechan and Ottolini (1980) and Phinney *et al.* (1981) provide an excellent discussion on the analysis of transformed record sections and the reader is referred to these papers. However, two specific points in the application of the inversion procedure should be noted. The results of the inversion deteriorate for cases in which (i) the data are spatially aliased and (ii) where the waveforms are not phase correlated or coherent

along a slant stack. Spatial aliasing of the data can be avoided if the source/receiver separation is less than one half of the wavelength of the highest frequency one wishes to resolve.

3.3.1 The plane-layered synthetic example

The wavefield in Figure 3.2 was obtained by downward continuing the $p-\tau$ wavefield of Figure 3.1b. Superimposed on the figure is the $p-z$ function used for the downward continuation. This inverse velocity depth function is also the one used to construct the plane-layered model from which the theoretical seismograms were derived (Figure 3.1a). This example illustrates the relationship between the downward continued wavefield and the true velocity depth function. In this example the $p-z$ wavefield images the true p-depth curve but there are some minor differences. The $p-z$ curve (solid line) between 0.5 and 0.455 s/km does not coincide with the large amplitude event. This could be due to spatial aliasing and the effects of using an average phase shift of $\pi/2$ for the reflection coefficients (see Section 3.2.2). The agreement improves for the deeper values. The small velocity jumps at 4.0 km depth are difficult to see but may be indicated by the small downward shift in the first arrivals for the last two traces. In any event, it would be missed in a real data case.

To illustrate the iterative nature of the procedure a full run using the plane-layered synthetic seismogram was performed and the results are depicted in Figure 3.3 a to e. To obtain these results the theoretical seismic section was read into the program, slant stacked (decomposed into its fixed p components) and the slant stacked wavefield was then downward continued (each p separately) using a constant velocity of 1.8 km/s for the zero-order iteration for all depths. Once the downward continued $p-z$ wavefield

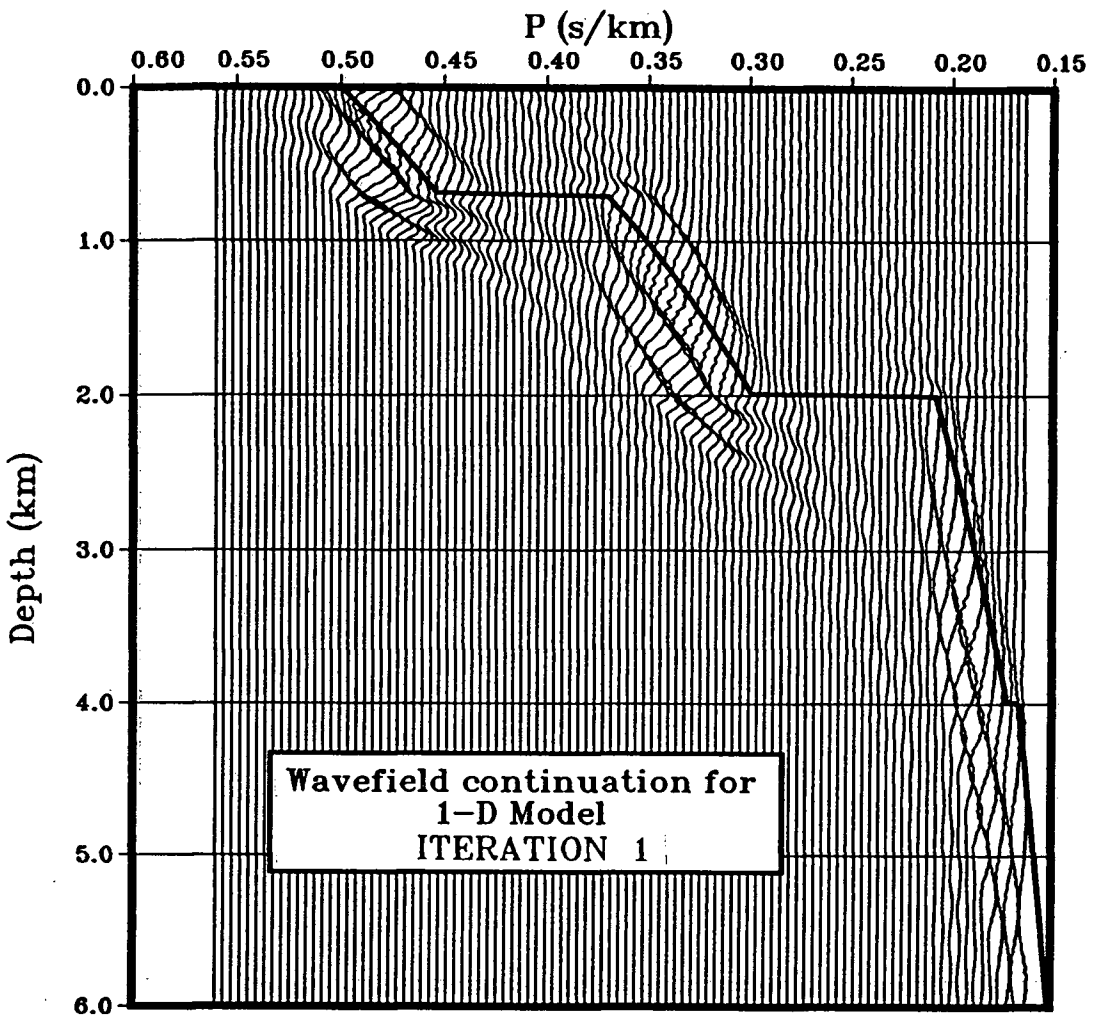

Figure 3.2 Downward continuation of the $p-\tau$ wavefield in figure 3.1b computed for the exact p–depth function (thick solid line). The relationship between wavefield and input p–depth function is illustrated for this best case in which the true p–depth function is known.

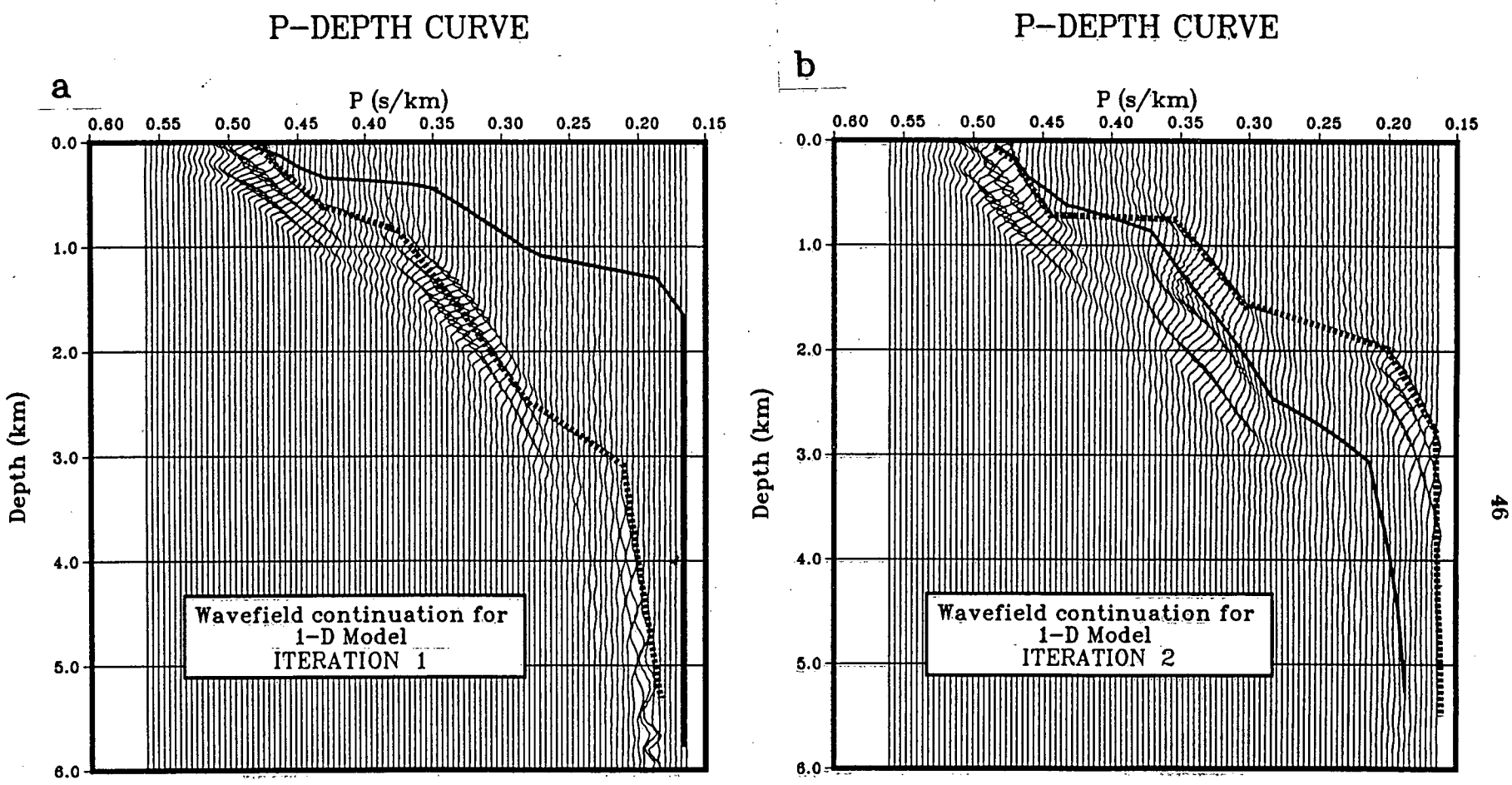

Figure 3.3 The figure panels (a) to (e) on this and the following two pages depict the iterative series for the downward continuation of the $p-\tau$ wavefield in figure 3.1b. Each panel shows the $p-z$ wavefield computed from the $p-\tau$ wavefield using the $p-z$ function (thick solid line) selected from the previous downward continued ($p-z$) wavefield. An initial $p-z$ wavefield was computed using a constant p or inverse velocity for all depths. This wavefield was then picked and the resulting $p-z$ function (thick solid line in (a)) was used to compute the wavefield in (a). This wavefield was then picked (the dashed line in (a)) for the next iteration (b) where it is now plotted as a thick line. This process continues until convergence is obtained (see text for detailled explanation).

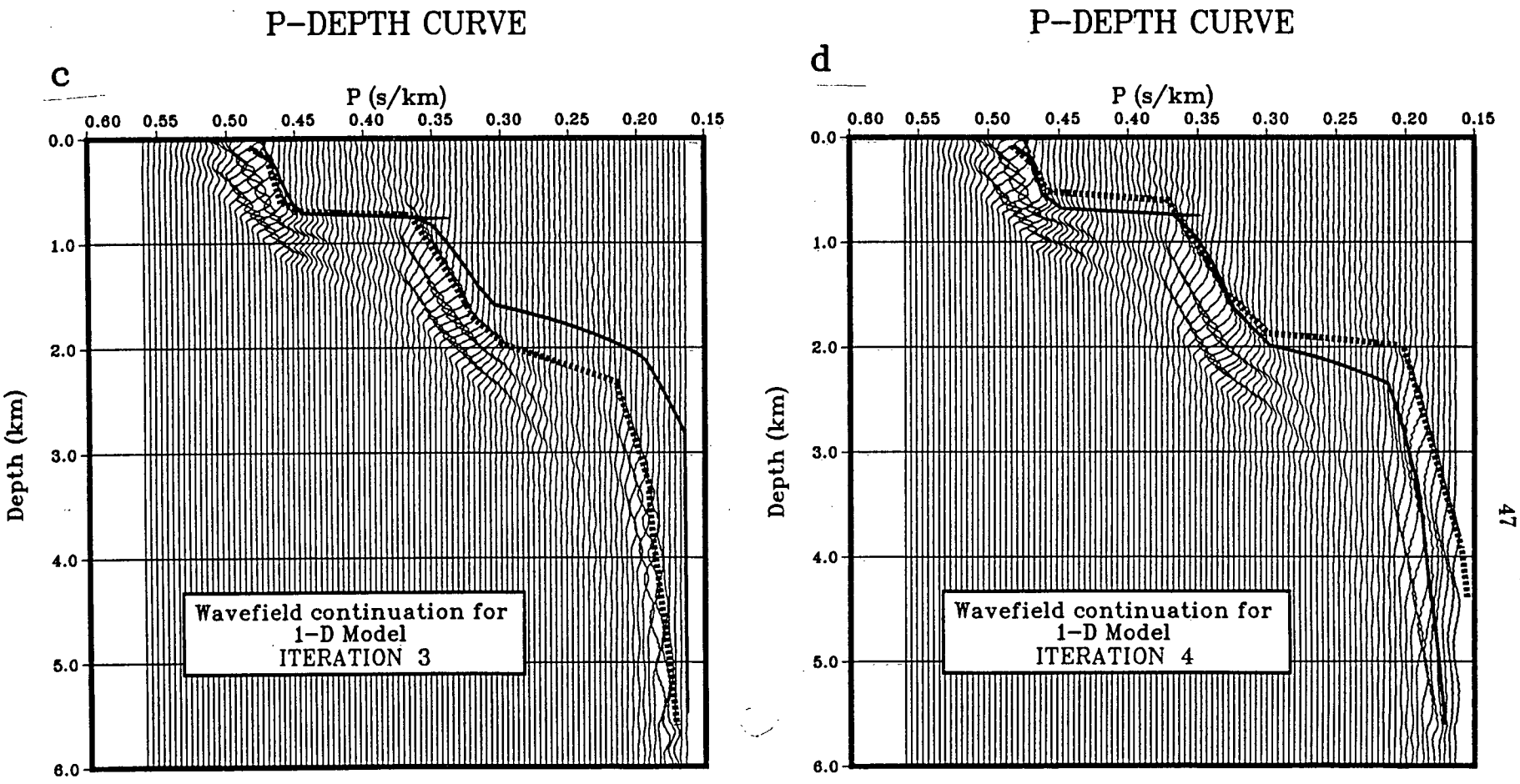

Figure 3.3 c & d Downward continued $p - \tau$ wavefield computed for $p - z$ function from Iteration 2 (c) and Iteration 3 (d).

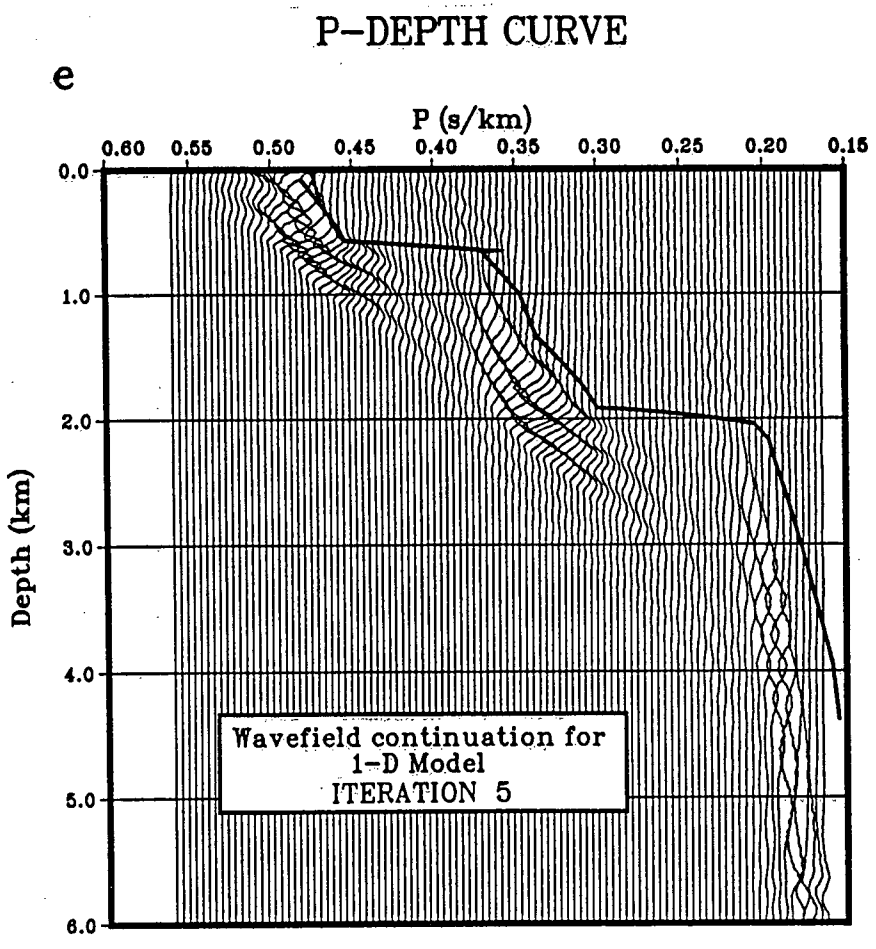

Figure 3.3 e Downward continued $p - \tau$ wavefield computed for $p - z$ function from Iteration 4.

was displayed on the terminal, control returned to the user. The user then proceeded to input new velocity versus depth curves by picking values as per section 3.2.2, until convergence was obtained. As each new iteration is carried out, the solution oscillates between high p at low z values and low p at high z values (Figure 3.3a-e).

Convergence can be recognized by two means. The first occurrs when a single $p-z$ curve is obtained for two or more iterations. The second occurs when two curves or successive iterations have the property such that inputting the high p, low z curve will yield the previous low p, high z curve and *vice versa*. Clayton and McMechan (1981) use this property to select a solution which is the average of these two curves. The two curves form an envelope which contains an optimal solution, but this is not to be confused with uncertainty in the result which is based on the width of the $p-z$ image at convergence (Clayton and McMechan, 1981). This is similar to other inversion schemes which attempt to define the envelope of all possible solutions (McMechan and Wiggins, 1972; Bessonova *et al.*, 1974). A further indication of convergence is the focussing of the amplitudes along the $p-z$ image. As convergence is approached, this image 'brightens'.

Figure 3.3a has been labelled iteration 1 and is the result obtained by picking the image in the initial $p-z$ wavefield for the constant velocity depth curve. Therefore, iteration 1 refers to that iteration which follows from the first user picked $p-z$ curve, indicated by the solid line. The dashed line in Figure 3.3a is the curve picked for this display of the wavefield. This convention is followed for all the examples given; the dashed line represents the present pick while the solid line represents the previous pick. In the picking of the $p-z$ images for this and the other examples, the point corresponding to the maximum amplitude at minimum z was selected. Also, a small number of points were picked and the program linearly interpolated between them to give a result similar to that used to define the model (layers with linear velocity gradients).

In Figure 3.3a the basis for picking the $p-z$ curve for the first 0.7 km in depth is clear. At this depth the amplitudes of this first locus continue but it must be remembered that we are looking for the 1-D $v-z$ curve. Thus, the point chosen was the maximum peak at the next monotonically lower z value. This is at a value of 0.370 s/km. The next point chosen was at the lower end of this second major locus, but such that it was not lower than the amplitude for the wavelets in the third major locus. This is the general procedure used for the entire picking process for all the examples given in this chapter. The results of picking the dashed curve in Figure 3.3a are shown in Figure 3.3b. The $p-z$ image now mostly appears above that of the previous pick (the solid line, Figure 3.3b) for depths below 1 km. This process continued for Figure 3.3 b to e. The final panel (Figure 3.3e) was not picked as it represents the final iteration based upon the previous pick. This is how the interactive session would normally terminate since the result of any pick is applied before control returns to the user. During the picking process, a possible guide to jumping the low amplitude regions from one major locus to the next are the "knees" which form at the base of each linear gradient (see Figure 3.3c at $z = 0.6$ and $p = 0.45$).

The $p-z$ curves from the last two iterations (the solid lines in Figure 3.3d and e) are shown in Figure 3.4 along with the correct velocity depth function. The lack of agreement in the upper 1.0 km of depth is probably due to spatial aliasing of the data. For these depths and velocities, a trace spacing of 110 meters would be required, but for this example a trace spacing of 200 m was used.

Between a depth of 1 and 2 km, agreement between the correct curve and the downward continued wavefield is very good. Below this depth the last two iterations form bounds on the correct solution. The resolution of the graphics video display device used in the interactive session also contributed to the poorer results for the velocity

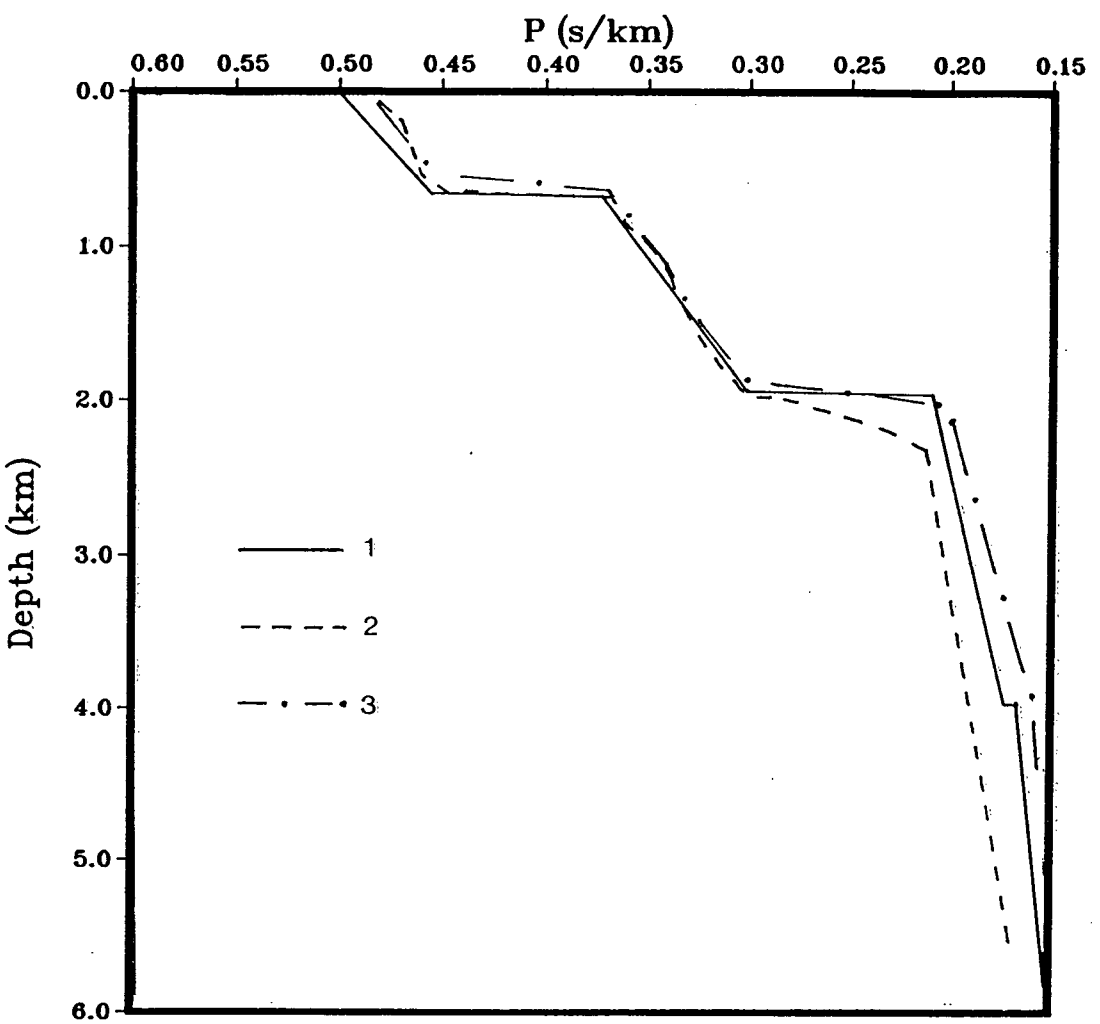

Figure 3.4 Comparison of $p - z$ functions from figure 3.3d (line 2) and e (line 3) with exact $p - z$ function (line 1) from 1-D model.

values picked at depths greater than 2.0 km. Furthermore, as noted in section 3.2.1, the rays did not densely sample the layer and this contributes to the poorly determined values at deep z.

3.3.2 The 2–D synthetic example

The 2–D synthetic example is from the modelling results for the OBS 3 to OBS 2 record section in chapter IV. Inverting the 2–D synthetic example served as an instructive guide prior to inverting the real data example. Knowing the actual structure of the model from which the seismograms were calculated allowed for comparisons between the two methods, particularly with respect to the effect of applying this inversion to a 2–D case.

The synthetic seismogram section, generated by the asymptotic ray theory method as described by Spence *et al.* (1984), is shown in Figure 3.5a. The slant stacked wavefield is illustrated in Figure 3.5b. The transformed branches corresponding to the travel time curves have been labelled as in Section 3.3.1. The extended nature of the transformed branches is due to the curvature of the travel time branch which results from the velocity gradients in the model. The travel-time branches **II** and **III** appear to be a single branch but a slight change can be observed at a model distance of 6.0km. Similiarly for the transformed branches, a slight change can be seen between **ii** and **iii**. Arrival branch **IV** transforms to the clear, but low amplitude, $p-\tau$ branch **iv**. The multiple event **V** transforms to the $p-\tau$ event **v** appearing lower in the transformed wavefield and therefore does not interfere with the primary $p-\tau$ event. By slant stacking the amplitudes within a specified window the destructive interference effects from the extended wavelets of events outside this window could be diminished. This would have

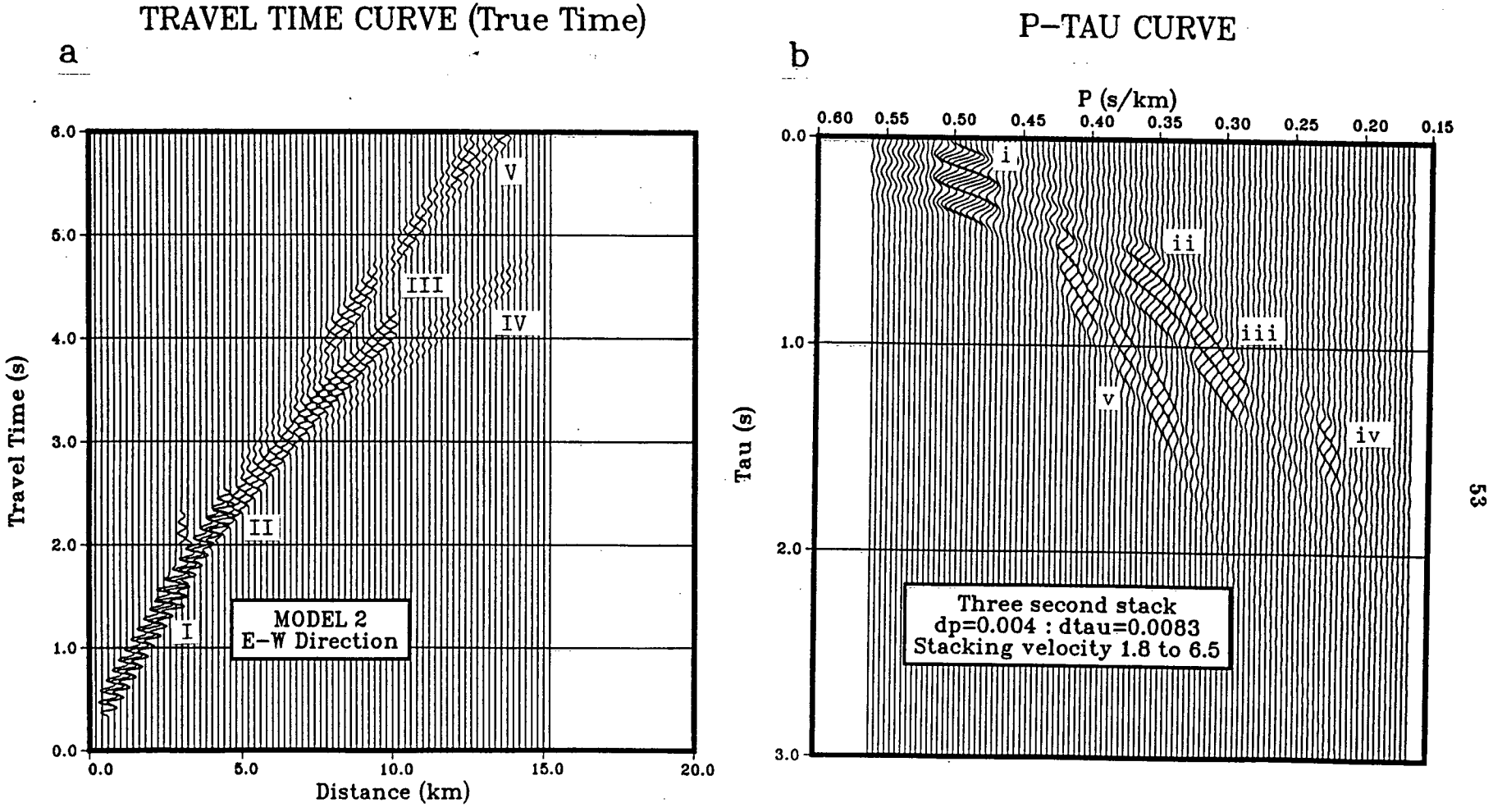

Figure 3.5 Slant stacked wavefield (b) for theoretical seismograms (a) computed for 2-D velocity sub-model of Chapter IV, section 4.3.2 (see figure 3.2 for explanation of symbols).

the desirable effect of increasing the range of larger amplitudes for each transformed branch. An example would be the $p - \tau$ branch iv. The amplitudes at the upper end of the branch could have been depressed by the interference from the amplitude in the wavelet for travel-time branch III.

For the downward continuation of the $p - \tau$ wavefield shown in Figure 3.5b, the same procedure as outlined in section 3.3.2 was followed. For each iteration, the maximum amplitude at minimum z was picked from the $p - z$ wavefield and used for the next iteration. The final three iterations are displayed in Figures 3.6 a to c. The solid line in Figure 3.6a was the input $p - z$ pick used to downward continue the wavefield presented in this figure. The dashed line represents the pick made from this wavefield in the interactive session for the next iteration shown in Figure 3.6b (it now appears in this figure as the solid line). A similar description applies to Figure 3.6c. A decision was then made to choose which of these results represented convergence. The dashed line in Figure 3.6b was chosen as the first indicator. This choice was made because the amplitudes increased significantly between the wavefields shown in Figure 3.6a and b. The small velocity jump, which recurs at a depth of 3.8 km was based upon the weak amplitudes extending horizontally, combined with the severe decrease in amplitude observed after the trace indicated by the arrow. Analysis of these amplitudes is only made possible by the noise-free data. The second curve picked (dashed line, Figure 3.6b) was chosen as the second and final indicator for convergence. It is shown as the solid line in Figure 3.6c. In general, the amplitudes are weaker than those seen in the wavefields for Figure 3.6a and b. Based upon these two observations, the solid lines of Figure 3.6 b and c (or conversely the dashed lines of Figure 3.6 a and b) were chosen as the two curves defining convergence.

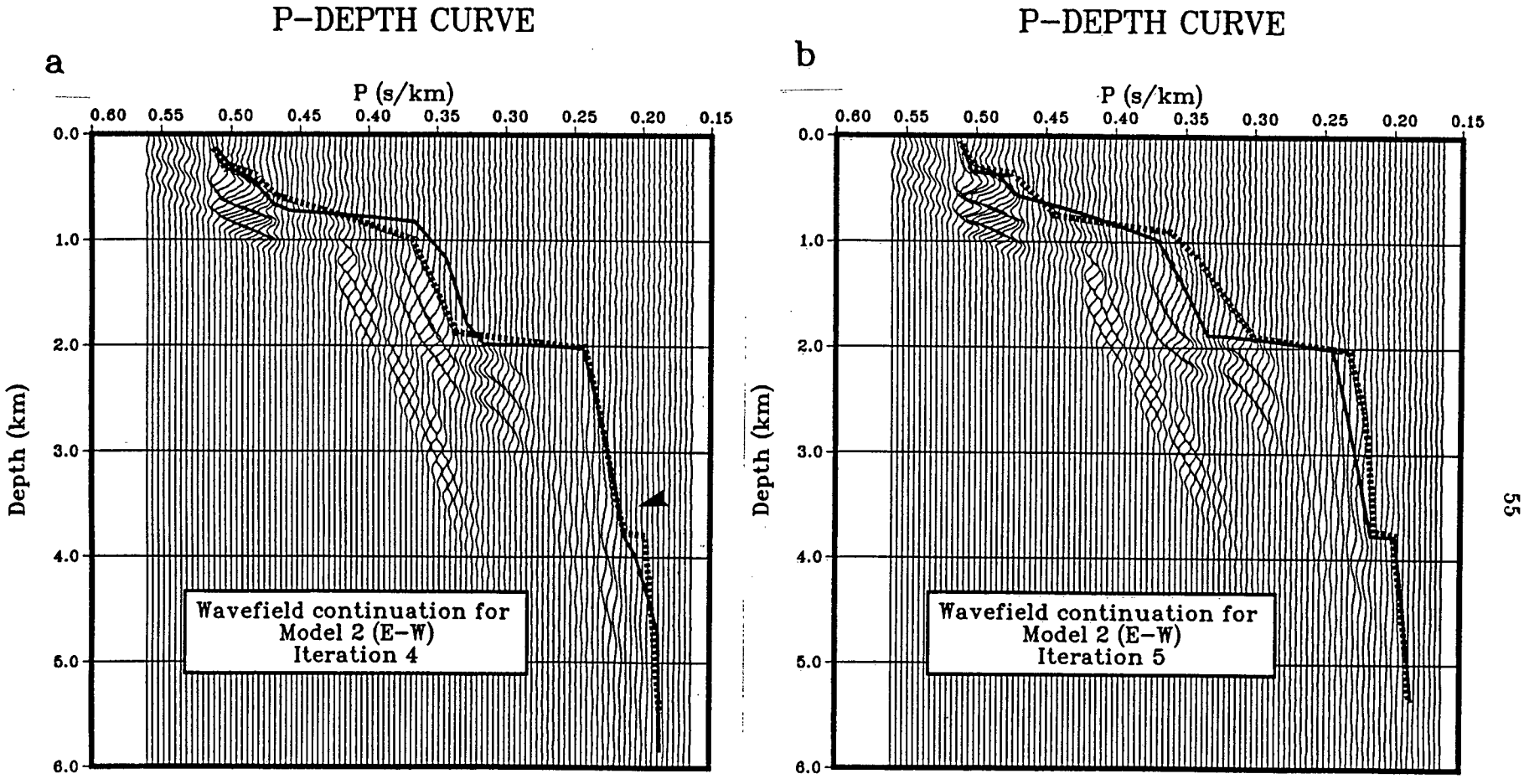

Figure 3.6 The figure panels (a) to (c) depict the final three iterations for the downward continuation of the $p - \tau$ wavefield in figure 3.5b . (see figure 3.3 and text for explanation)

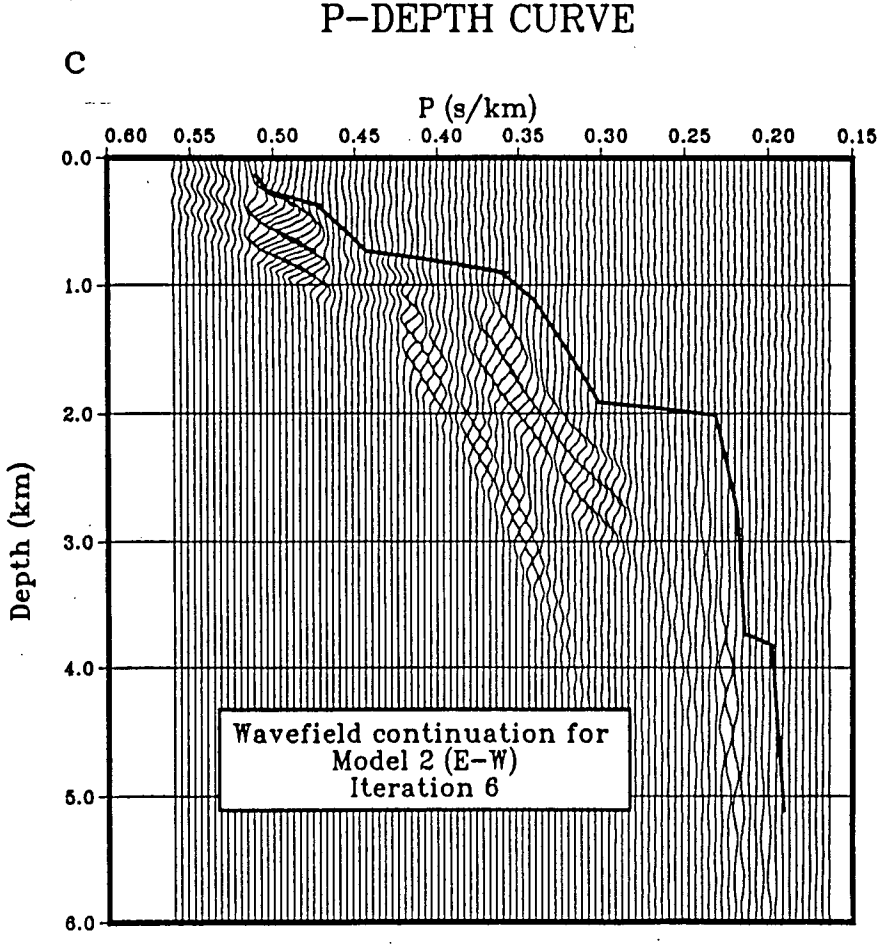

Figure 3.6 c Downward continuation of $p - \tau$ wavefield for Iteration 6 .

Five p-depth functions were selected from the 2–D model, where it was sampled by the rays, and averaged. The average p-depth function and those for the last two iterations are shown in Figure 3.7. Comparing the three curves in this figure shows how the downward continued wavefield solutions (curves 2 and 3) appear to have averaged the velocities across the model. This result can be described as a 1–D kinematic equivalent for the actual 2–D velocity structure.

The minor discrepancies observed can be attributed to the effects of not windowing the stack, spatial aliasing, the resolution of the graphics terminal at high p, low z values, and the 2-D nature of the model itself. A plane-layered model constructed from an average of these curves could easily be perturbed to fit the 2-D model. We might then expect that for the real data example the imaged result will represent a 1-D kinematic equivalent for the 2-D earth model. As the subsurface structure more closely approaches a laterally homogenous model, the result will begin to reflect a more accurate representation of the subsurface velocity distribution.

3.3.3 A real data example

In this last example, observed data, the interpretation of which led to the theoretical data used in section 3.3.2, were used in the wavefield transformation procedure. The record section and the slant stacked record section are shown in Figure 3.8a and 3.8b. The primary arrivals transform to the maximum amplitude locus at minimum τ. The large amplitude event, lower amplitude event and the multiple event are labelled as in previous diagrams. The larger amplitude artifacts appearing above the primary $p - \tau$ event in Figure 3.8b may in part be due to transformed precritical reflections not clearly evident in the seismogram. Clayton and McMechan (1981) observed similiar

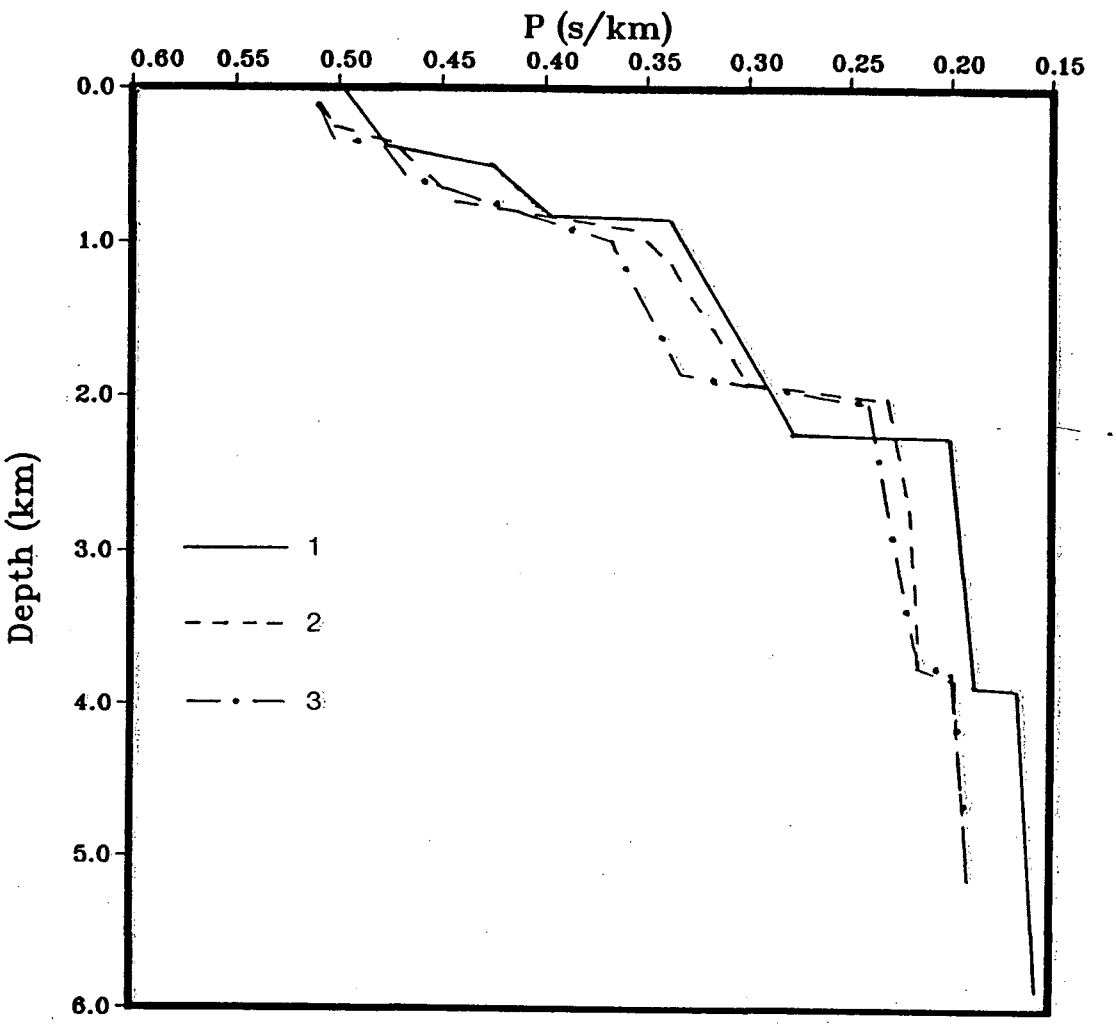

Figure 3.7 Comparison of $p - z$ functions from figure 3.3b (line 2) and (c) (line 3) with average $p - z$ function for 2-D model (line 1). The average $p - z$ function was calculated for five $p - z$ curves selected along the 2-D sub-model in figure 4.11b where it is sampled by simple refracted ray paths.

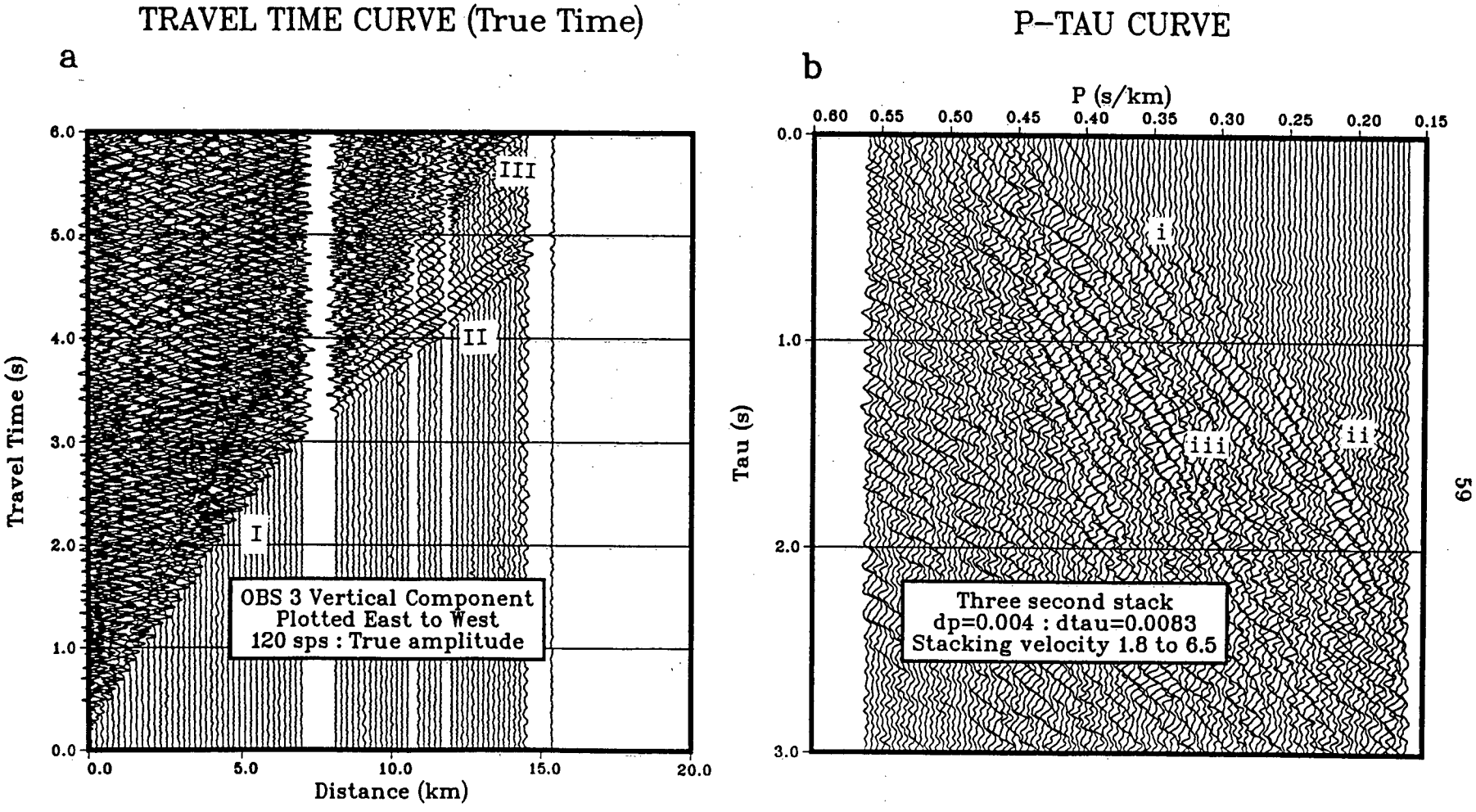

Figure 3.8 Slant stacked wavefield (b) for OBS 3 reverse profile (a) (see section 4.3.2) plotted from east to west. (see figure 3.1 and text for explanation of figure)

features for their examples. The reverberatory nature of the seismic signal contributes to reverbations in the $p - \tau$ section, but below the transformed primary arrivals. The data gaps do not appear to have had an adverse effect on the slant stack. Their main effect would probably be reducing the potential amplitude of arrivals which fell along the slant stack line.

The downward continuation steps are depicted in Figure 3.9a–e. The interpretation of the real data set presents some new problems. The recognition of the true transformed primary is sometimes confused by the noise in the data. However, one clear gain in the real data case is in terms of the focusing effect on the downward continued wavefield. It is much more pronounced than in the synthetic example and this helps to counteract the adverse noise effect. In Figure 3.9a, the solid line shows the peak from the zero-order (constant velocity) downward continued wavefield. At a depth of 2.0 km the p depth curve was extended to fill the data space. This is simply a requirement of the resampling routine in the program.

The dashed line shows the pick for the use in the next iteration. The picks are based upon the maximum amplitude at minimum z. Where the amplitude shifted downward in z for an adjacent trace, a point was selected at the top and the bottom of this jump (see the arrow in Figure 3.9a). Otherwise, the same procedure as described in the previous section was followed. The blocky straight line approach was used where possible. That is, not every peak was picked, nor need be, but key points in the curve were picked and the program interpolated between these points. The process continued until the $p - z$ wavefield was deemed to have converged. Iterations 4 and 5 (Figure 3.9 d and e) were identified as the two convergent indicators. In this example the curve, picked from the wavefield in Figure 3.9d, actually fits the downward continued wavefield of Figure 3.9e. This result figured strongly in the decision to terminate the iterative

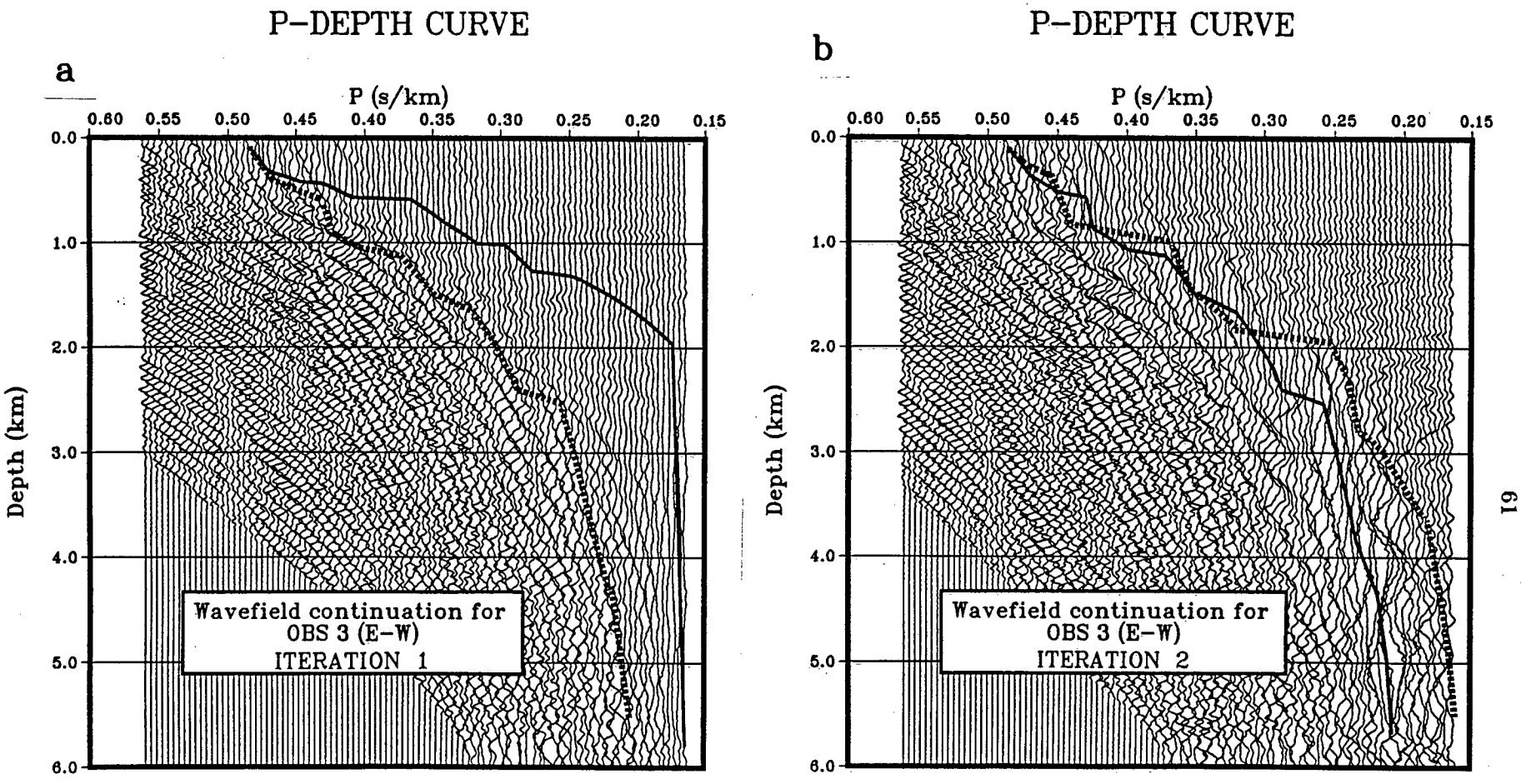

Figure 3.9 Figure panels (a) to (e) depict the iterative series for the downward continuation of the $p-\tau$ wavefield in figure 3.8b.(see figure 3.3 and text for explanation)

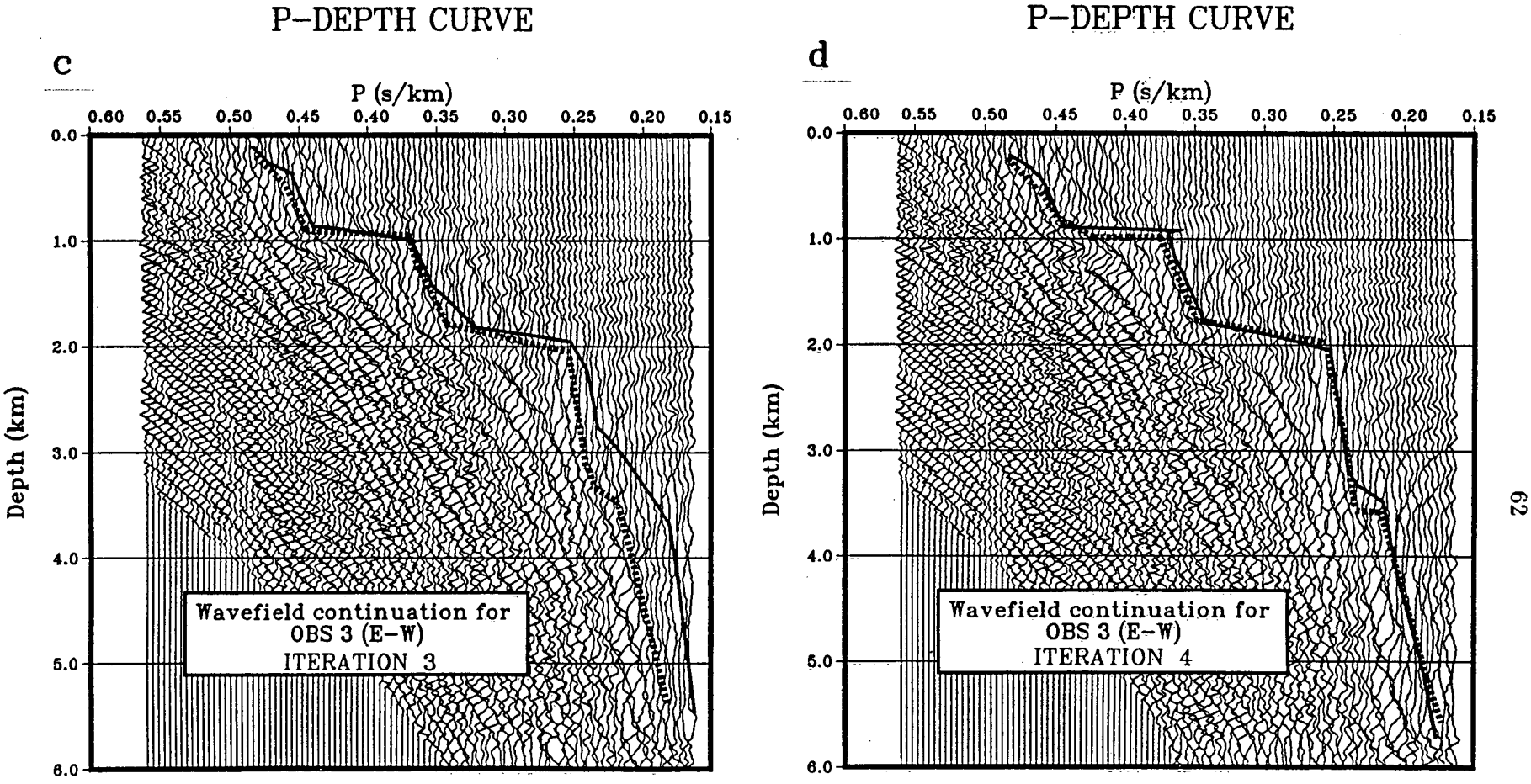

Figure 3.9 c & d downward continued $p - \tau$ wavefield for Iteration 3 (c) and Iteration 4 (d).

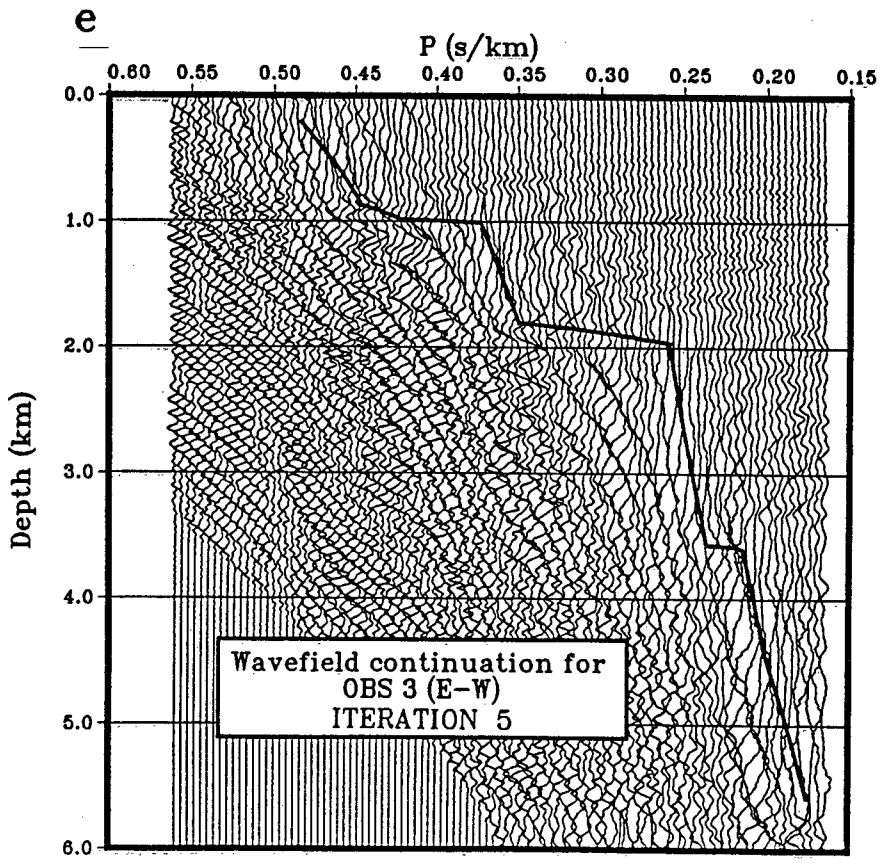

Figure 3.9 e Downward continued $p - \tau$ wavefield for final iteration. The $p - z$ pick from the previous downward continuation is also consistent with this one so convergence has been achieved.

process. The final two results (the solid lines from Figures 3.9 d and e) are shown in Figure 3.10 along with the same p-depth curve from the previous section (see Figure 3.7). The velocity gradients and velocity increases for the inversion curves match those for the averaged velocity-depth curve from the 2–D model quite well. In general the inversion gave $p - z$ values that were lower than the $p - z$ curve for the 2–D modelling. This could be attributed to the previously outlined problems and for this case, problems associated with the accurate identification of the maximum event and minimum depth for the transformed primary arrival event. Noise may have contributed to incorrectly identifying the lower amplitude $p - z$ events during the picking process. For depths below 2.0 km, the strong lateral heterogeneity of the 2–D model would indicate that this factor has the largest effect on the final result (see Figure 4.11b).

3.3.4 Summary

The inversion procedure yielded the correct velocity depth curve for the plane layered case. The result was obtained quickly and in an unbiased fashion. When the subsurface earth model diverges from a plane layered case the solution obtained from the wavefield continuation appears to represent a 1–D kinematic equivalent for the 2–D velocity model. Effects of noise, at least at low levels, and reverberations in the data do not appear to degrade the results for the example considered. This is principally because the first arrival amplitudes in the $t - x$ domain transform into amplitudes which have minimum p and z values.

What are the implications of these findings? There appear to be several. As shown by Clayton and McMechan (1981), the inversion of seismograms recorded over areas known to have a nearly plane-layered velocity structure yields valid results. A second

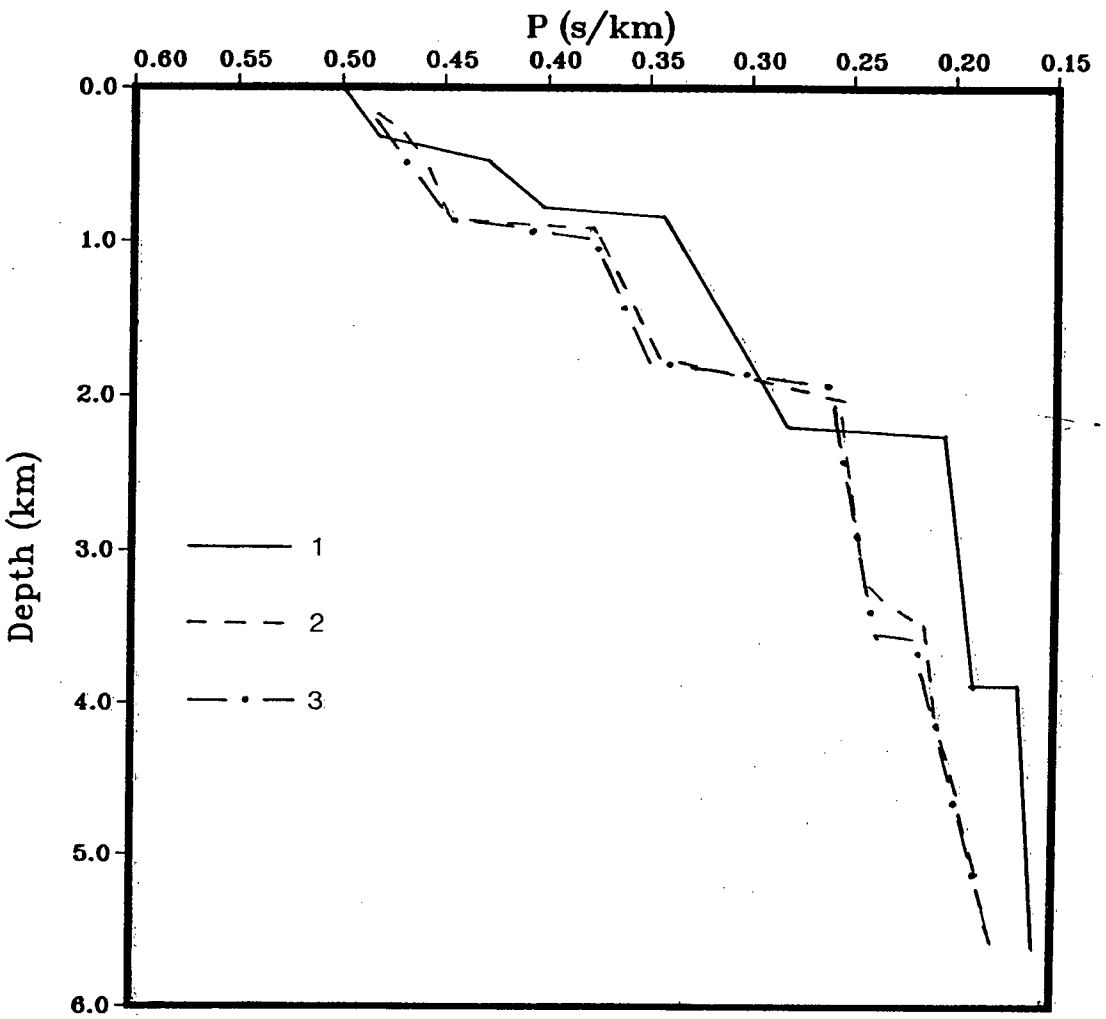

Figure 3.10 Compasrison of $p-z$ functions from figure 3.9d (line 2) and (e) (line 3) with average $p-z$ function from 2-D model as per figure 3.7 .

result from this study is that the method can be applied to velocity structures with an even higher degree of lateral variation if an approximate function is the objective. In other words, if only an initial model is desired for further perturbation by a 2–D modelling scheme, this method can provide a quick and efficient means of obtaining the starting model. A dipping layered model may be obtained by inverting both the forward and reverse profiles. The density of rays sampling the subsurface at either end of the profile will be weighted for that end. If there is structure, then the results from a forward and reverse profile inversion will be slightly different and could be used as the basis for an initial 2-D model

An important observation is that extreme caution is advised in the application of this inversion method to a data set recorded over an area where little or nothing is known about the subsurface. Clayton and McMechan (1981) inverted a real data example as a demonstration of the robustness of the method for cases where weak lateral velocity variations exist. The data indicated only weak local velocity effects and an interpretation from a nearby profile supported their results. If the theoretical seismograms of Figure 3.5a are considered, the primary arrivals are observed to increase smoothly along the trajectory described by these arrivals. Yet the model (see Figure 4.11b) from which these seismograms were generated is 2–D. These observations suggest that the indiscriminant application of a 1–D inversion to data judged by their own merit as representing arrivals from a plane layered earth would lead to an erroneous solution. It is clear that the real data set inverted in this chapter indicated no severe effects due to a strongly two-dimensional velocity structure. Yet subsequent results from the 2-D modelling indicate otherwise. Although the modelling process is non-unique, it is constrained by forward and reverse profiles and supported by results from previous

studies (Shouldice, 1971, 1973; and Stacey and Stephens,1969) as described in Chapter IV.

Based on the program written for this study, and its application to synthetic and real data, several recommendations can be made. For the slant stack operation, the stack should be windowed to reduce the effects from arrivals not associated with the stacking velocity. Secondly, for the airgun signature which has a stronger amplitude in the second cycle of the arrival, the program could be designed to use this amplitude for the inversion. This could be accomplished by applying a phase shift to move this peak to the right depth. Clayton and McMechan (1981) do something similar when they use multiples to extract the velocity vs depth curve. They accomplish this by using the fact that the multiples have twice the τ of corresponding primaries and implement the appropriate phase rotation by doubling the frequency. This allows the multiples to be used to extract the p-depth curve. Therefore, a phase shift of possibly a quarter of a wavelength may allow the user to utilize the strong maximum in the airgun signature to extract the p-depth curve. Filtered data and $p - \tau$ sections were tested using a zero-phase bandpass filter, but the side lobes interferred with the recognition of the first maximum amplitudes at minimum z in the downward continued wavefield. The zero phase characteristic of the filter may have been the problem. Further investigation is recommended.

CHAPTER IV MODELLING OF THE AIRGUN-OBS DATA

4.1 Introduction

The airgun-OBS data were modelled in three segments using the 2-D ray trace synthetic seismogram algorithm described by Spence *et al.* (1984). The segments were defined by the data sets between OBS 1 and OBS 2, OBS 2 and OBS 3 and OBS 3 and OBS 4. The forward and reversed profiles were modelled simultaneously for each segment of the airgun line. None of the seismic record sections presented in this chapter have been filtered unless otherwise indicated. A $r^{1/2}$ geometrical spreading factor, where r is the offset, has been applied to both the theoretical and observed amplitudes for each seismogram. The amplitudes on the observed seismograms were oversuppressed by its application for seismograms within 3.0 km of the receiver. This occurs because the actual receiver was never directly below the source whereas this must be the case for a 2-D model. However, this oversuppression diminishes beyond the 3.0 km source-receiver distance. The travel time fits should be reliable after a 1.0 km source-receiver distance.

The modelling for each segment will be discussed separately for the forward and reverse profiles. This will be followed by a summary of the model that was developed for that segment plus a brief geological interpretation. Throughout the following discussion only the vertical component for each data set is presented. However the horizontal and hydrophone components were used when they provided constraints for questionable events on the vertical component seismogram. Appendix II includes record sections for all components. The final velocity model is presented in Figure 4.1 for reference during the following discussions. Where values for velocities and/or gradients are uncertain

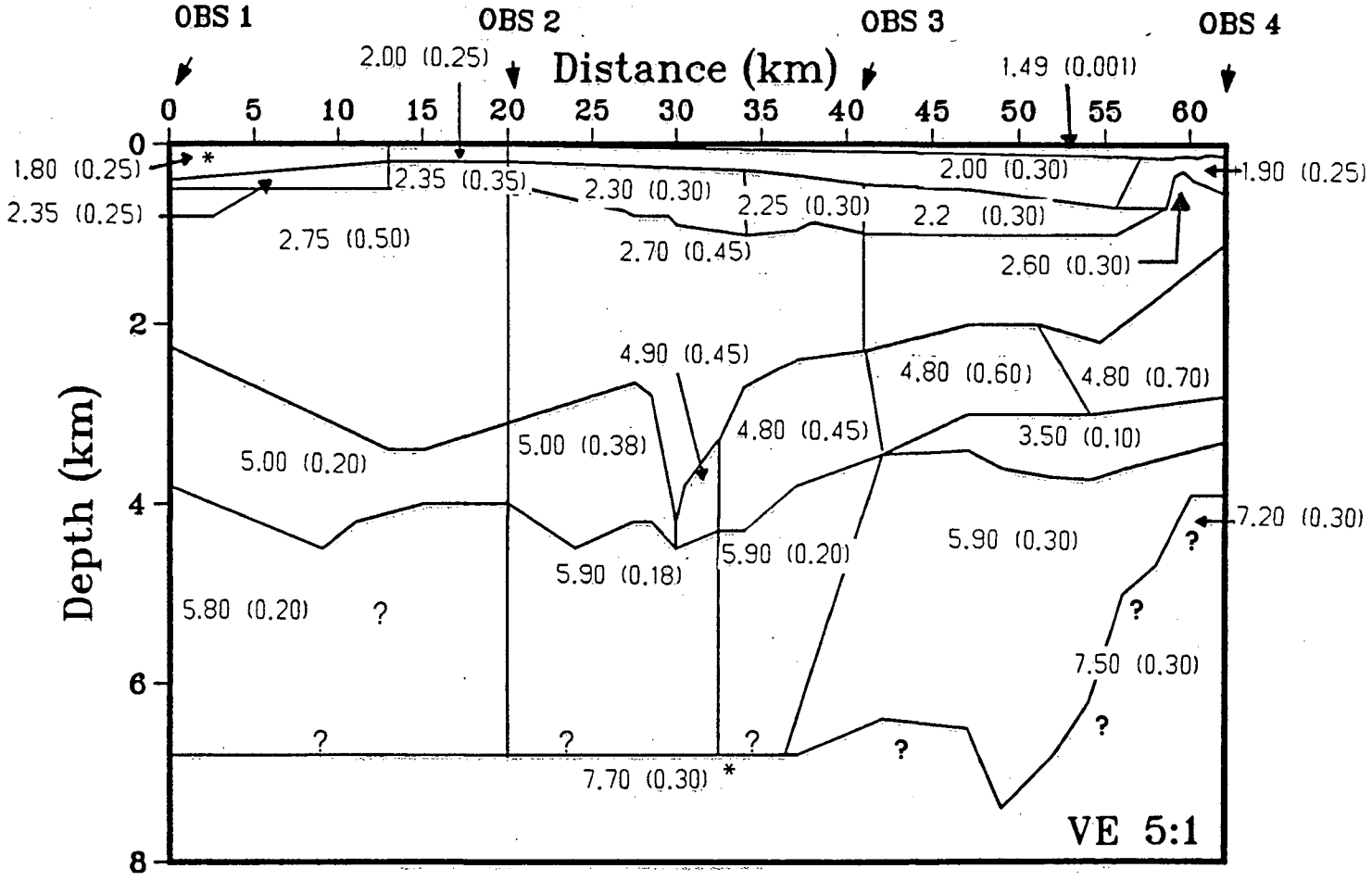

Figure 4.1 Final velocity model for airgun/OBS survey. Velocities for each polygonal block apply to the upper boundary or the uppermost boundary segment when indicated. Velocity gradients for the blocks are enclosed in brackets and increase downwards along a line perpendicular to the upper boundary. The location of the OBSs with respect to the final composite model are indicated at the top of the model. The model is plotted with a vertical exageration of 5:1 . Uncertainties in the values derived from the model are indicated by (*) while undefined regions of the model are marked by (?).

have been indicated by an asterisk. Question marks are used to indicate regions where little control exists for the velocities and gradients used.

4.2 Initial Constraints

The isopach for the Tertiary Skonun sediments (Shouldice 1971, 1973) derived from industry reflection and refraction seismic data along with wells drilled in the Queen Charlotte basin provided constraints for the model. The sonic logs from these wells provided the necessary justification for the choice of large velocity gradients. Where data processing affected the near offset traces (see Chapter II) such that interpreted velocities were not reliable, sonic logs from wells near the airgun line were used to constrain the velocity for the upper sedimentary layers. A gravity survey (Stacey and Stephens, 1969), nearly coincident with the airgun line, also provided justification for the gross structural characteristics of the model observed at its eastern end. The initial model was constructed by projecting the position of the OBSs onto the model presented by Shouldice (1971) and using the velocities from the wells combined with the velocities derived from considering the forward and reverse profiles.

4.3 OBS 1— OBS 2 Submodel

For the purposes of this and the following sections, the *Forward profile* refers to the record section where the source-receiver distance increases from west to east. The *Reverse profile* refers to source-receiver distances that increase from east to west. The relative position of the OBS that recorded the seismogram is indicated by the insert in either the upper left corner of the record section, as for the *Forward profile* or the upper right hand corner, as for the *Reverse profile*. Any distances quoted in the following

discussions will be indicated by the qualifiers *MD* for model distances and *SRD* for source-receiver distances.

The theoretical travel time curves have been superimposed as solid curves on the observed seismograms and are labelled by lower case letters. The model through which rays are traced appears directly below the seismogram. The ray groups reach the surface below their corresponding travel time curves on the seismogram. In a following figure the data are also presented above the theoretical seismograms derived from the model. In this case, the travel time curves have been omitted from the real data display so as not to detract from the amplitude comparison between theoretical and observed seismograms.

4.3.1 Forward profile

The record section for the forward profile is shown in Figure 4.2A. Figure 4.2B shows the ray traced model for the OBS 1 to OBS 2 segment, see Figure 4.1 and Figure 2.1.

The analog data were digitized for only the near offset arrivals (first 7.0 km *SRD*) as the noise level completely obscured the seismic signal beyond this range. The high noise levels for OBS 1 may be attributed at least partly to the shallow depth of this particular OBS.

The model is separated into two basic units, the lower velocity sedimentary unit and the higher velocity crystalline unit although the latter is not defined by the forward profile but by the reversed one (section 4.3.2). The lower velocity sedimentary unit is further divided into three low velocity layers. The energy from the upper layer was modelled by refractions through a layer with a velocity of 1.8 km/s. The theoretical travel time branch, a, matches the observed arrivals but the sonic logs from nearby

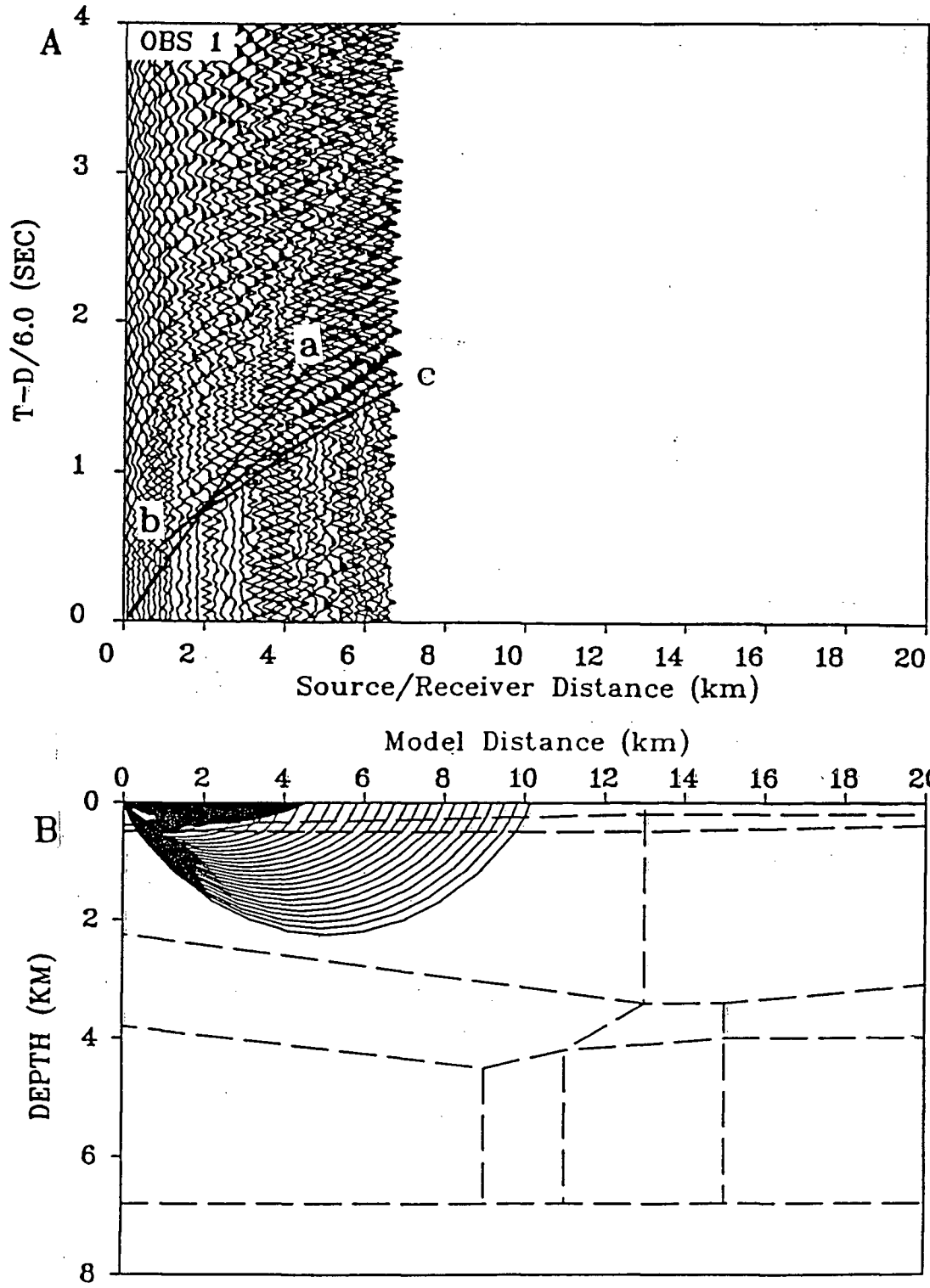

Figure 4.2 The data for OBS 1 (A) are displayed above the ray tracing diagram for the OBS 1—OBS 2 sub-model (B). The source/receiver distance *SRD* is plotted along the horizontal axis for the data. Model distance *MD* is plotted along the horizontal axis for the ray tracing diagram. The data are plotted in reduced time format such that arrivals with an apparent velocity of 6.0 km/s appear horizontal. The travel time curves, labelled **a** to **c**, superimposed on the data were computed from the corresponding ray groups appearing below each curve. The relative position of the OBS is indicated by the label in the upper part of the record section (see text for discussion).

wells indicate a velocity of 2.0 km/s for the upper sediments. The discrepancy may be attributed to the processing of the data. Good fixes on the position of the OBSs improve where split spread information is available. Furthermore the near offset traces are more strongly affected by residual 3-D effects associated with their true offline position after the 2-D projection (see Chapter II).

Refractions through the 2.35 km/s layer in the model are not seen to emerge as primary arrivals but the precritical reflections from the top of the 2.75 km/s layer, curve b, do match the large secondary arrivals seen between 1.0 and 1.7 km *SRD*. The refractions through the 2.75 km/s layer, branch c, emerge as the first set of primary arrivals seen after branch a. The thinness of the 2.35 km/s layer, less than 100 meters, probably accounts for this. This layer may or may not be present at this end of the sub-model but is observed in the other sub-models and therefore has been incorporated into the interpretation . Since the accuracy of the results at near offset are affected by the data processing, elimination of this layer was not justified. The data are noisy but a bandpass filtered (5-12 Hz) record section plus the good response on the horizontal geophone, aided in the determination of the first breaks.

The theoretical seismograms are compared with the observed data in Figure 4.3. A gradient of 0.50 km/s/km in the 2.75 km/s layer was chosen to give a good relative match between the observed and the synthetic amplitudes. For the Queen Charlotte basin, gradients in excess of 1.0 km/s/km are observed from the sonic well logs.

4.3.2 Reverse profile

The reversed profile shown in Figure 4.4a recorded seismic energy out to 17 km *SRD*. Only this profile extended across most of the range between OBS 2 to OBS 1.

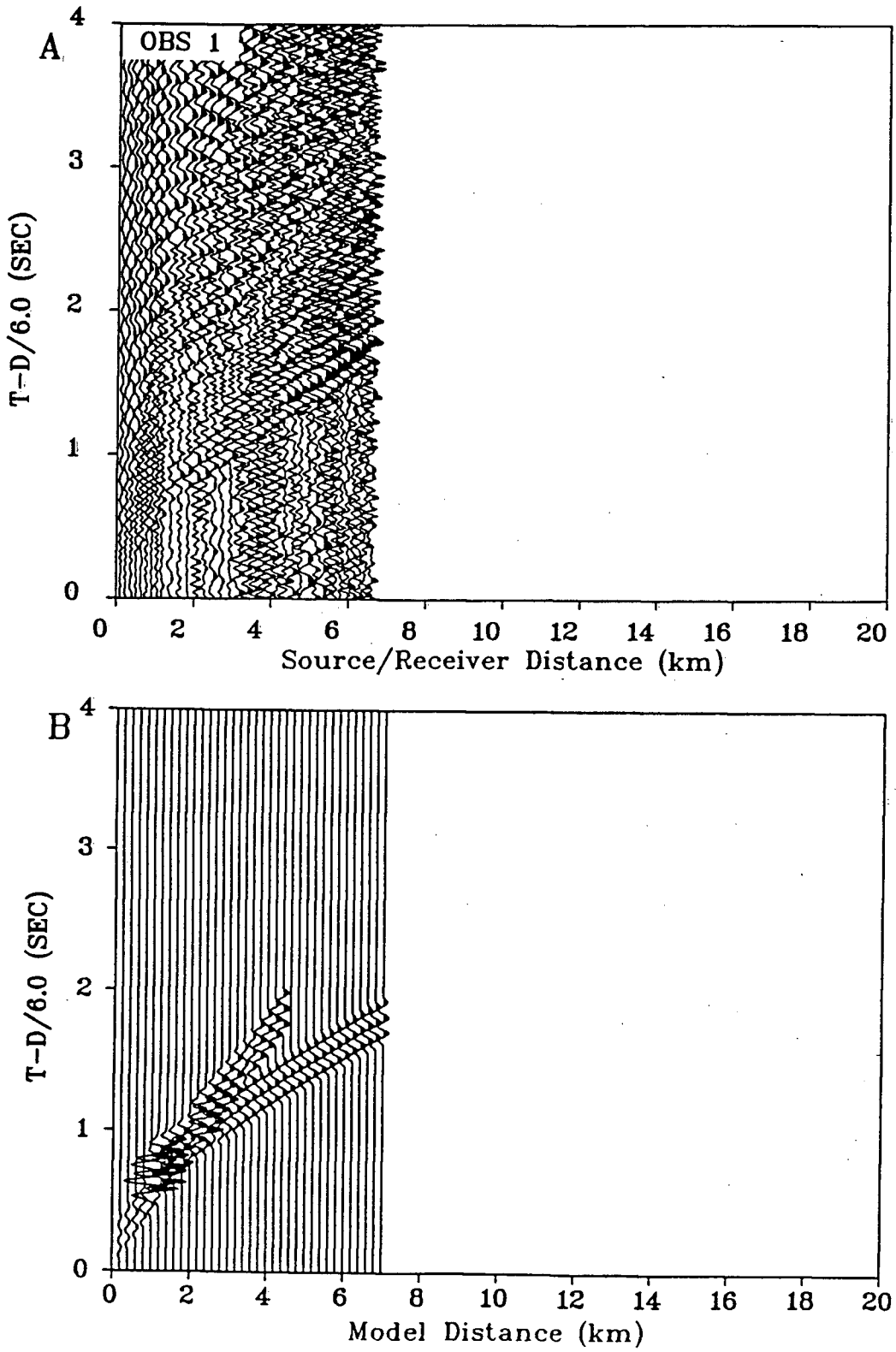

Figure 4.3 Data for OBS 1 (A) is compared with the synthetic seismograms (B) computed for the ray tracing diagram in figure 4.2B. Both the data and the synthetic seismograms are plotted with the same scale factors. The *MD* plotted along the horizontal axis of the synthetic seismograms corresponds to those of the ray tracing diagram.

The isopach of the Tertiary sediments and the known basinward dip extrapolated from the geology observed on the Queen Charlotte Islands provided the needed constraints for the sub-model.

The amplitudes of the first arrivals are strong out to 10 km *SRD* where they then drop off quite suddenly. Beyond 10 km *SRD*, the seismic signals are very weak. The onset of a higher velocity branch can be seen between 10 km and 11 km *SRD*.

Rays traced through the 2.0 km/s layer generated theoretical traveltimes that matched the observations between the 0 and 1.0 km *SRD*, curve a in Figure 4.4A. This value is consistent with the velocities for the upper sediments measured by the sonic logs. Energy refracted through the 2.35 km/s layer, slightly thicker near OBS 2, emerge as primary arrivals between 1.0 km and 1.8 km *SRD*, (curve b). A gradient of 0.35 km/s/km was required for this layer to match the observed amplitudes and produce a model consistent with that from the adjoining sub-model (OBS 2—OBS 3).

The arrivals between 2.0 and 10.0 km *SRD* were modelled by rays traced through a thick layer with a velocity of 2.75 km/s and a gradient of 0.50 km/s/km (curve c). The theoretical seismograms and the observed data are shown in Figure 4.5. The theoretical amplitudes that correspond to curve c actually remain large for an additional number of traces beyond where the amplitudes decrease abruptly. Considering the amplitudes at this offset (between 6 and 8 km *MD*) they appear to be large and end more abruptly than for the real data at equivalent offsets. The actual structure along the top of the 5.0 km/s layer may be responsible for this but the unreversed portion of this segment and the weak amplitudes for arrivals from this lower unit did not justify a more complex boundary.

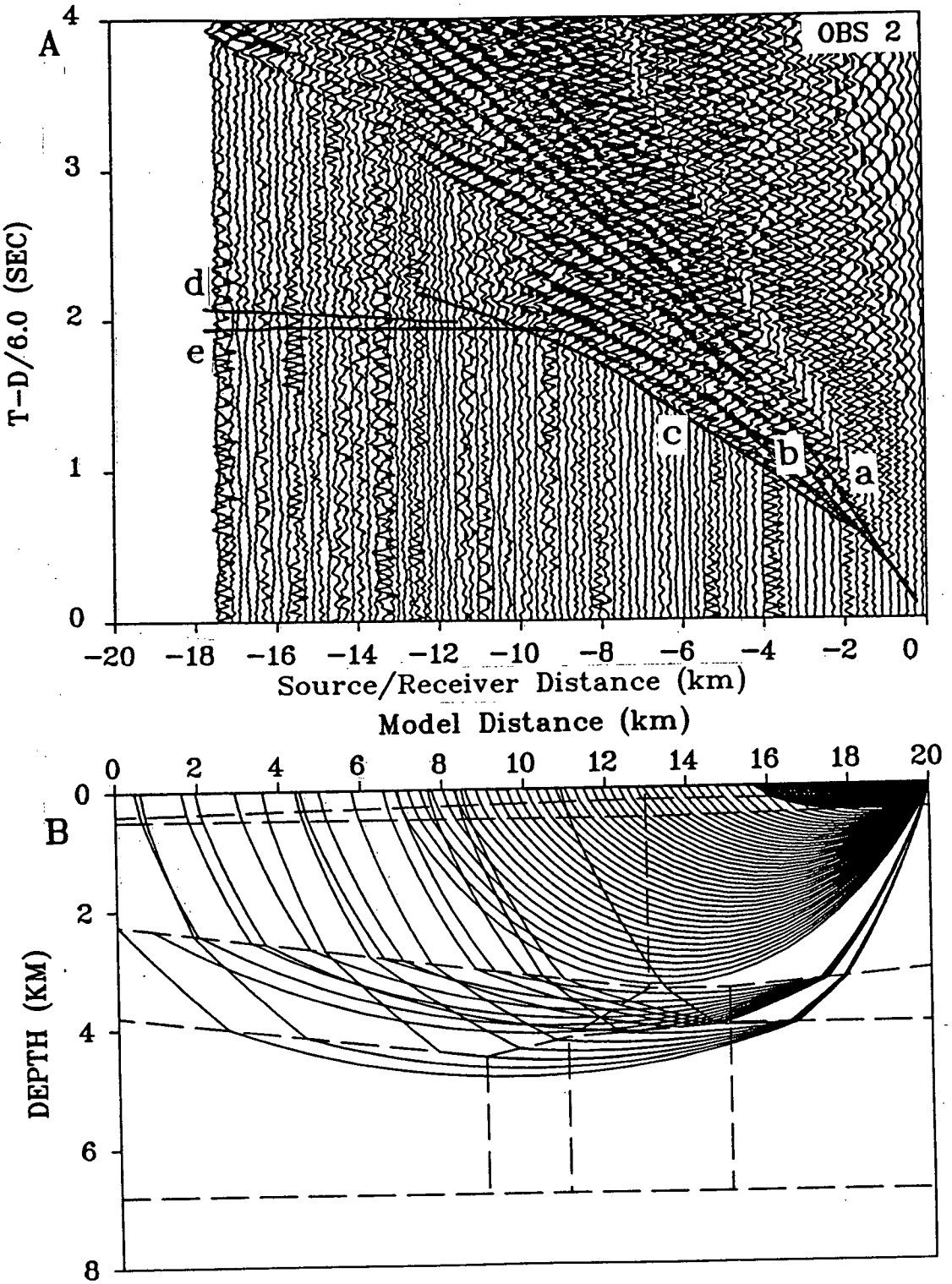

Figure 4.4 Data for OBS 2 reverse profile (A) and ray tracing diagram for OBS 1—OBS 2 sub-model (B). (see figure 4.2 for explanation)

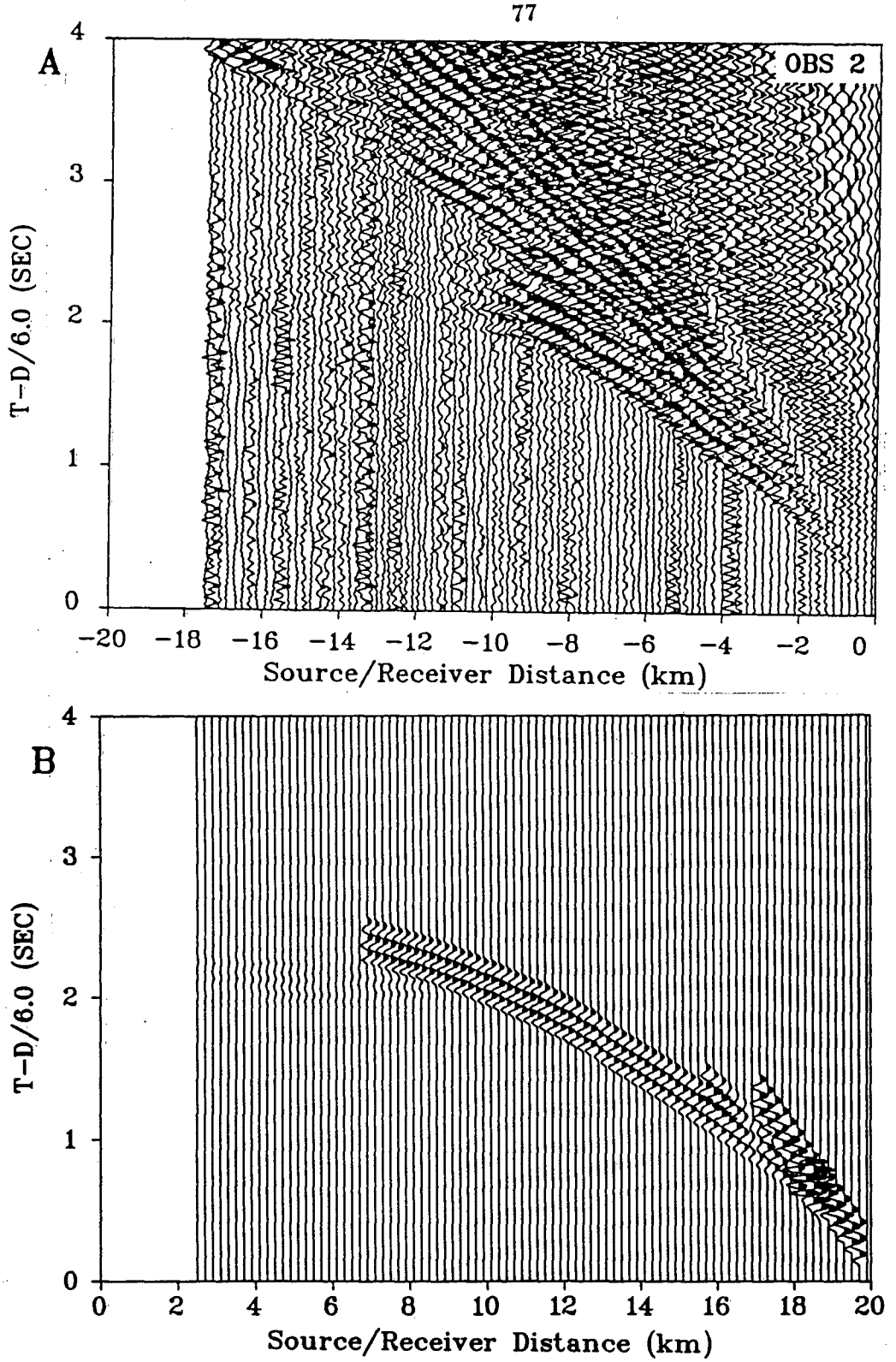

Figure 4.5 Comparison of data for OBS 2 reverse profile (A) with synthetic seismograms (B) computed for ray tracing diagram in figure 4.4B. (see figure 4.3 for explanation)

The velocity and depth of the 5.0 km/s and 5.8 km/s layers were constrained by the sonic log from the Tyee well (Figure 2.1) and the isopach trend. The neighbouring sub-model provided an additional constraint by requiring that the model features be continuous beneath OBS 2. The theoretical amplitudes, Figure 4.5B, show the weak amplitudes for the arrivals from these two layers. This indicates that the seismic signal in the data may be obscured by the noise. The theoretical travel time curve, e, coincides with the onset of the higher velocity arrival near the beginning of the curve. This energy can not be seen clearly to extend beyond about 11 km *SRD*, although some weak coherent energy may be discernible.

4.3.3 Summary

Figure 4.6 shows a three dimensional representation of the velocity changes along the sub-model between OBS 1 and OBS 2. Velocity and depth profiles were selected from different locations along the model and plotted in a 3–D display. The selected velocity-depth profiles are the solid curves increasing in a particular velocity-depth plane at fixed distance values. This presentation of the velocity information illustrates the overall velocity structure of the model, including velocity gradients.

The geological interpretation for each velocity unit is also shown. The thick 2.75 km/s unit is interpreted as the Tertiary Skonun sediments (Sutherland Brown, 1968). Thickening of this unit across the basin is supported by the isopach for the sediments (Figure 1.1). The sonic log from the Tyee well (Figure 2.1) is compared in Figure 4.7 with the velocity versus depth curve from the 15 km *MD* location. A visually smoothed average of the sonic log is also indicated by the thick solid line. The two compare quite favourably. The velocity from the sonic log has measured the characteristics of

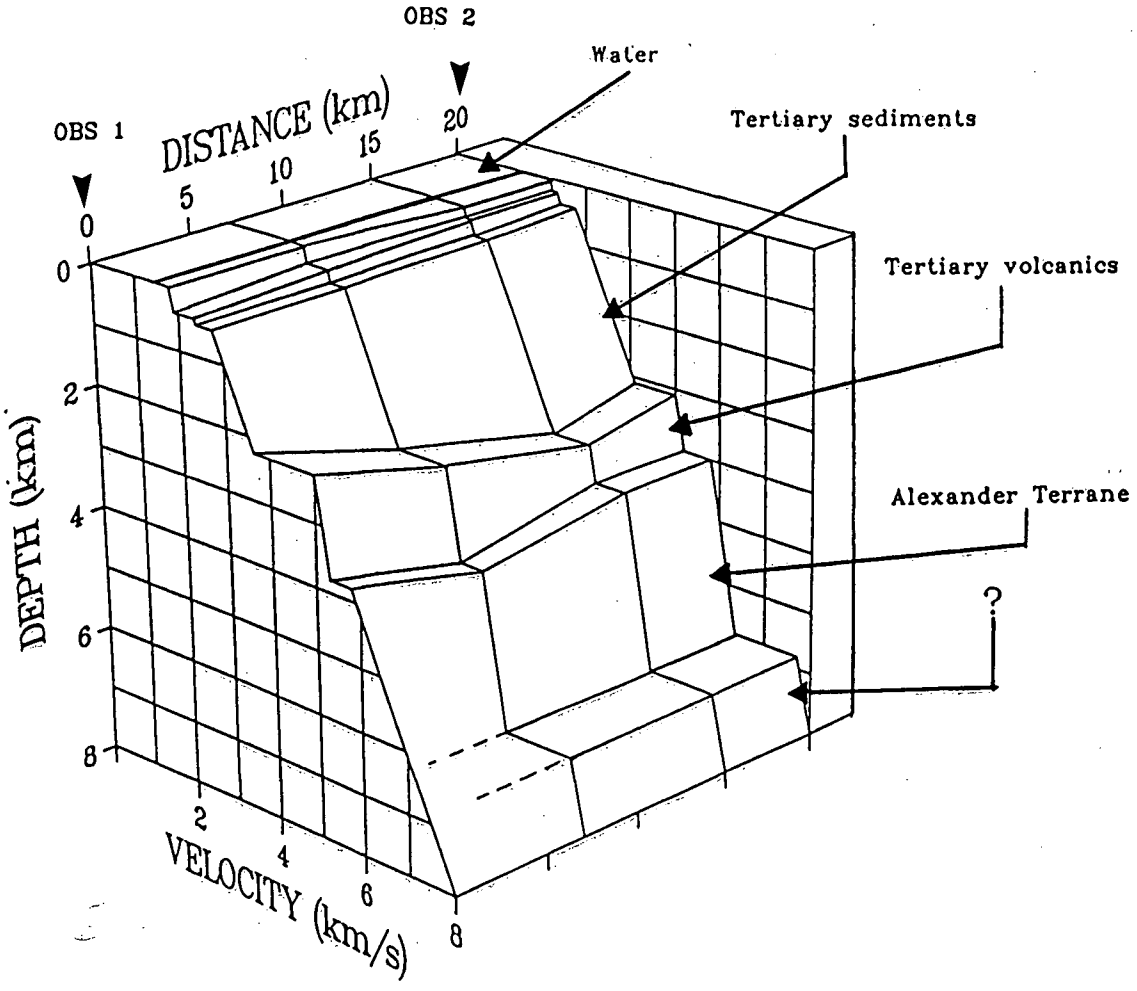

Figure 4.6 Velocity cube for OBS 1—OBS 2 sub-model with a brief geological interpretation. Model distance is plotted at the top of the diagram along the axis projecting into the page. The depth axis is plotted along the vertical axis. Velocity is plotted at the base of the diagram along the axis projecting out of the page. The velocity cube was constructed by selecting five velocity depth profiles from the sub-model at 0, 7, 15 and 20 km *MD*. The relative position of the two OBSs is indicated at the top of the diagram.

vertical wave propagation over distances of meters whereas the refraction method tends to provide horizontal velocity information over distances of kilometers. The velocity and the gradients can change significantly over short distances, a fact which also could be responsible for the differences in the velocity depth function between the two different locations. Such a characteristic is obvious when one compares the three sonic well logs for the Coho, Tyee, and Sockeye wells which are near the airgun line (Figure 4.8). Gradients in excess of 1.0 km/s/km are observed in the Sockeye well. This observation provided some of the justification for the large gradients that were sometimes required to model the amplitudes of the observed arrivals.

The 5.0 km/s unit underlying the Tertiary sediments of Figure 4.7 is interpreted as Tertiary volcanics, possibly the Masset formation (Sutherland Brown, 1968). The 5.8 km/s unit below this, although not well defined for this sub-model, is interpreted as the Paleozoic Alexander Terrane (Yorath and Chase, 1981). The velocity jump below this has only been included as a continuation of a unit from the adjoining sub-model and does not represent a true subsurface boundary for this sub-model.

4.4 OBS 2—OBS 3 Sub-model

In Figure 4.1 the sub-model for this segment of the airgun line corresponds to the range between 20 and 41 km *MD* as indicated by positions of the two OBSs. Pre-critical reflections could not be modelled as they were not observed in the data due to their reverberatory nature.

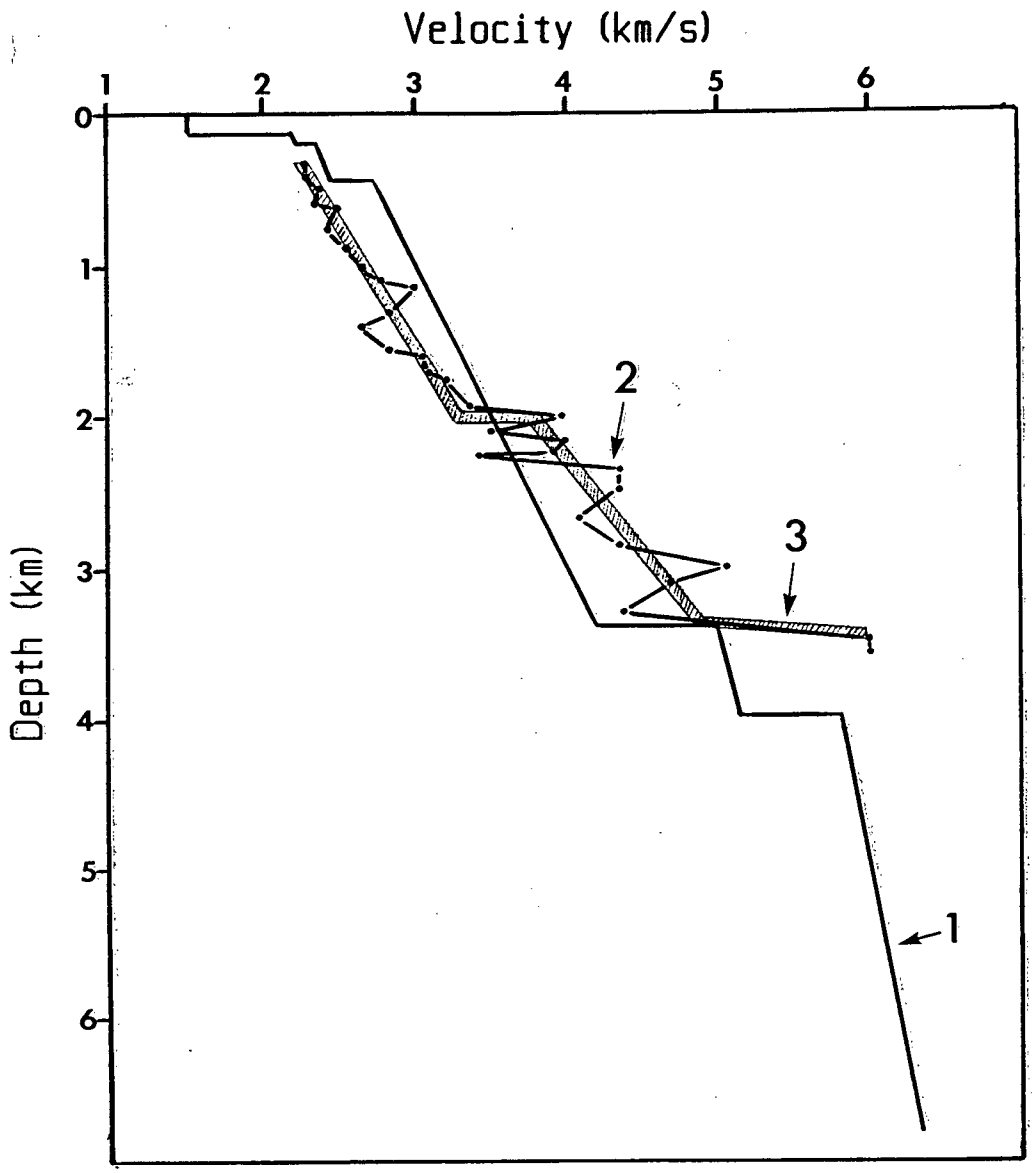

Figure 4.7 Comparison of velocity versus depth profile (curve 1) from OBS 1—OBS 2 sub-model at 15 km *MD* and the sonic log from the Tyee well (curve 2) and its visually smoothed version (curve 3).

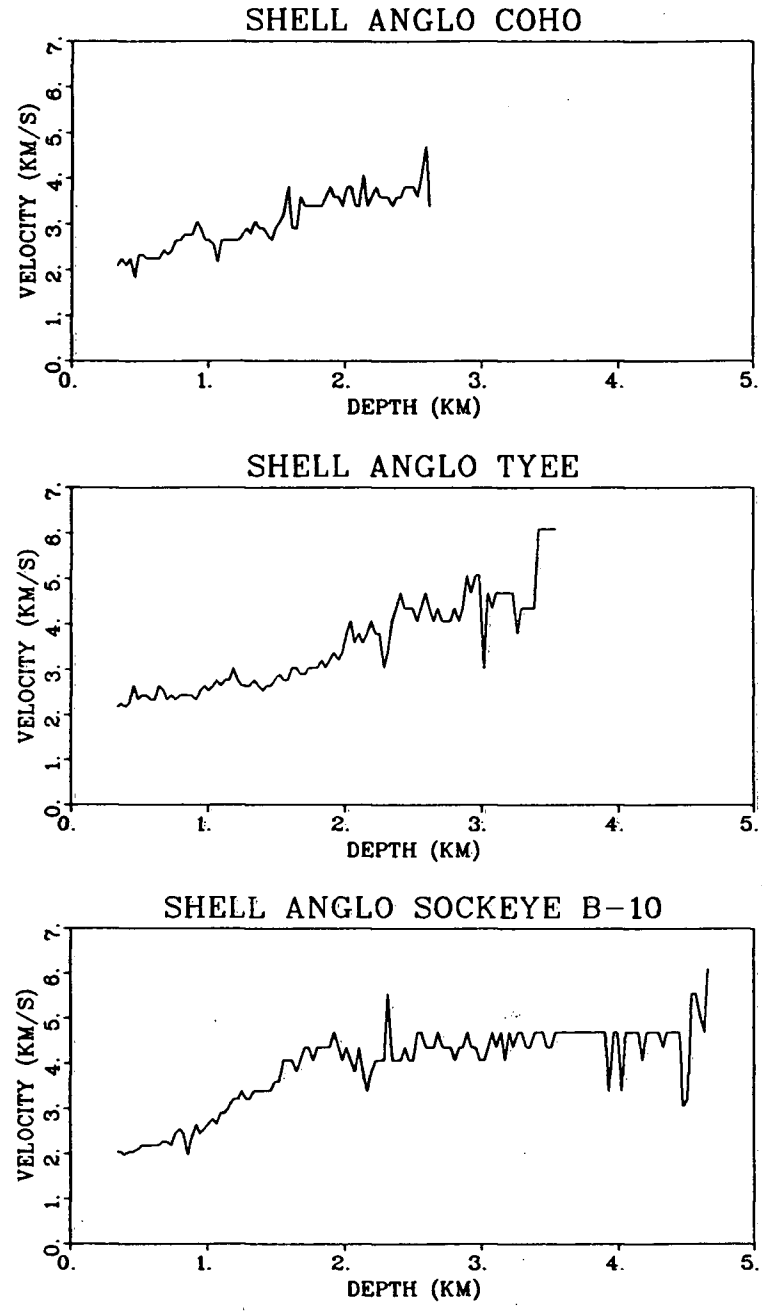

Figure 4.8 Sonic logs from the three wells (Coho, Tyee and Sockey B-10, figure 1.1) nearest the airgun/OBS line.

4.4.1 Forward profile

Results of the travel time fit to the data and the corresponding ray trace model are shown in Figure 4.9A and 4.9B, respectively. Curve **a** shows the fit to the observed travel times modelled by tracing rays through the upper 2.0 km/s layer. A gradient of 0.3 km/s/km was required to produce the proper curvature and match the amplitudes of these arrivals beyond the 3.0 km *SRD*(Figure 4.10b). The second theoretical travel time curve, **b**, modelled the energy arriving from the 2.30 km/s layer.

The gap in the data between 3.8 and 5.8 km *SRD* resulted from an airgun malfunction for approximately 20 minutes. An emerging higher velocity branch can be seen between 3.0 and 3.8 km *SRD* which can be followed and picked up along a continuous curve through the gap at 5.8 km *SRD*. Curve **c** models these arrivals as refractions through the Tertiary sediments (referred to in the previous sub-model). The amplitudes of the observed arrivals beyond 8.0 km *SRD*, Figure 4.9A and 4.10A, are weaker and, at the level of the noise, degrading the first break picks for this branch. These amplitudes die off sooner and more gradually than their theoretical counterparts. This may be due in part to the interference of other arrivals such as refracted multiples of possibly diffracted energy. The cut off in amplitudes was modelled by requiring that the volcanic unit (5.00 km/s layer) truncate the ray group for branch **c** (Figure 4.9). The theoretical travel time, curve **d**, for the group of rays that have travelled through the Tertiary volcanic unit emerge as a slightly weaker set of arrivals extending to 15.4 km *SRD* (Figure 4.9A and 4.10A). The lower apparent velocity for these arrivals was modelled by the drop off in depth of the surface of the volcanics. Previous studies (Shouldice, 1971, 1973; Yorath and Hyndman, 1983) show the top of the Tertiary volcanics to have been eroded during a period of uplift. There were even instances where the volcanics were

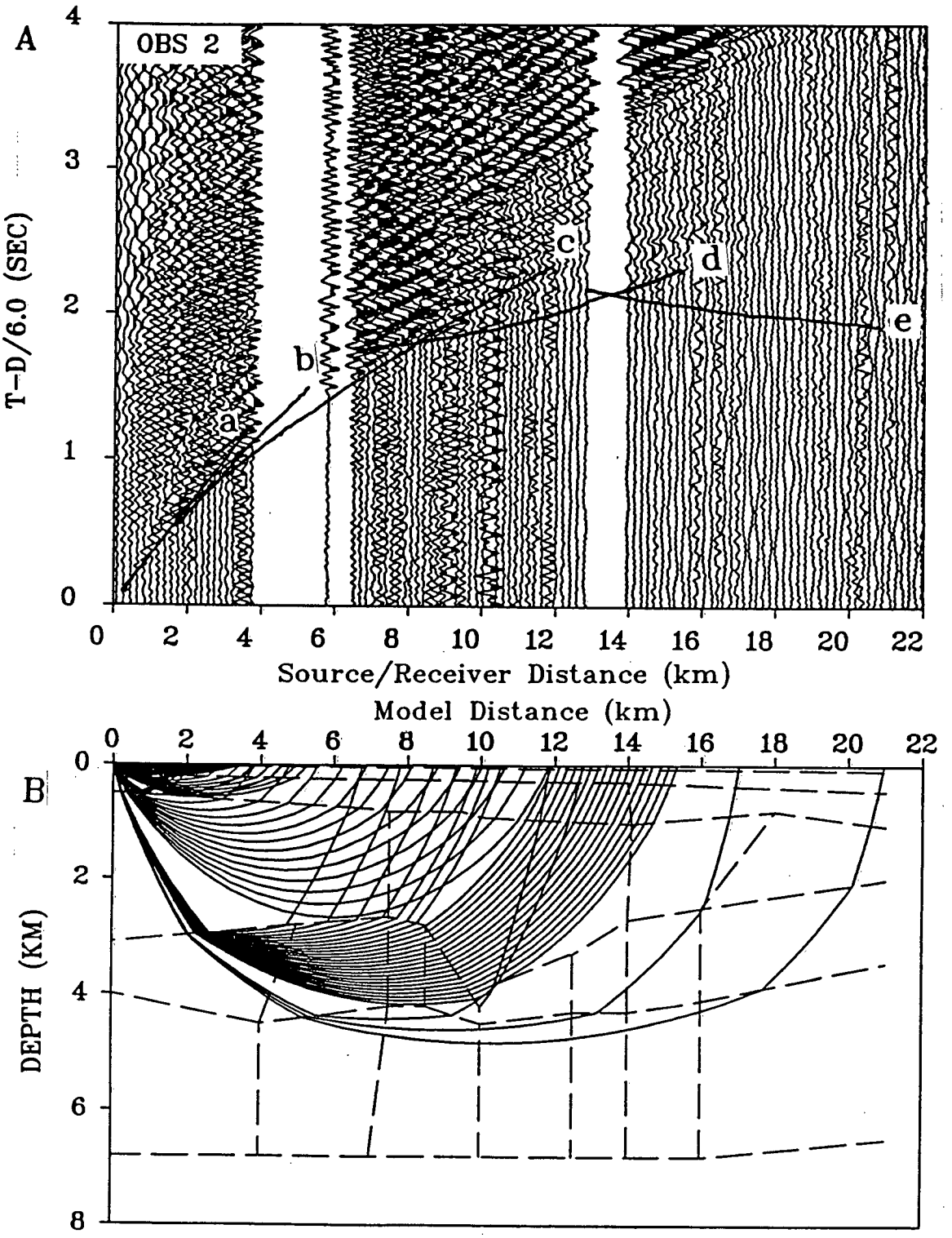

Figure 4.9 Data for OBS 2 forward profile (A) and the ray tracing diagram for OBS 2—OBS 3 sub-model (B). (see figure 4.2 for explanation)

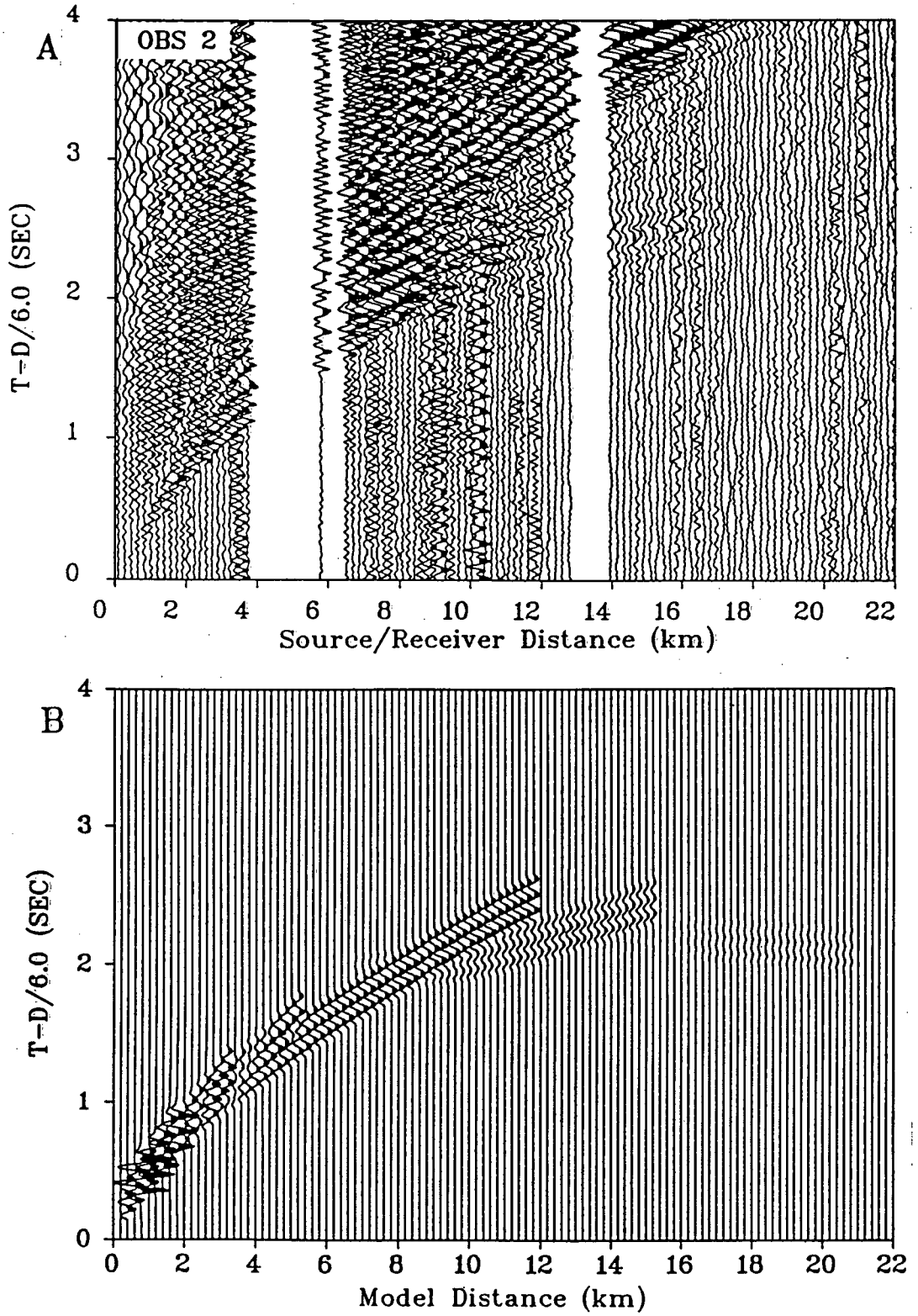

Figure 4.10 Comparison of data for OBS 2 forward profile (A) and synthetic seismograms (B) computed for ray tracing diagram in figure 4.9B (see figure 4.3 for explanation).

not present in some of the wells. Shouldice (1973) also indicates that the steep dips seen on the reflection seismic data may also be fault related.

The lower unit of the model, 5.9 km/s layer, models the energy thought to have just sampled the upper part of the interpreted Alexander Terrane, curve e. Observed arrivals can not be clearly seen in the data but when these data were bandpass filtered weak correlated arrivals could be discerned at the appropriate range and time, but the location of the first breaks could not be determined. The synthetic amplitudes for curve e Figure 4.9B indicate that these arrivals are weak. The theoretical seismogram, Figure 4.10B, and the observed seismogram, Figure 4.10A, compare well in their overall response.

4.4.2 Reverse profile

OBS 3 recorded strong seismic signals, with a good signal to noise ratio (SNR) (Figure 4.11A and 4.12A). It was located 21 km from OBS 2 at the eastern end of the sub-model. The model at this end can be seen to be changing slightly. The upper two sedimentary units were modelled as for the forward profile, except that the lower unit required a lower velocity (2.25 km/s) beneath OBS 3 to provide some continuity between the adjacent sub-models at this location. The theoretical travel times for arrivals from these two layers in the sub-model are shown in Figure 4.11A, curves a and b. The water depth increases towards the east and a corresponding thickening of the uppermost sediments is observed in the sub-model. The theoretical travel time curve, c, modelled observed arrivals as due to ray travel paths through the Tertiary sedimentary layer (2.7 km/s). To match the observed arrivals out to 9.0 km *SRD*, the sediments were required to thicken towards the west. This thickening of the sediments

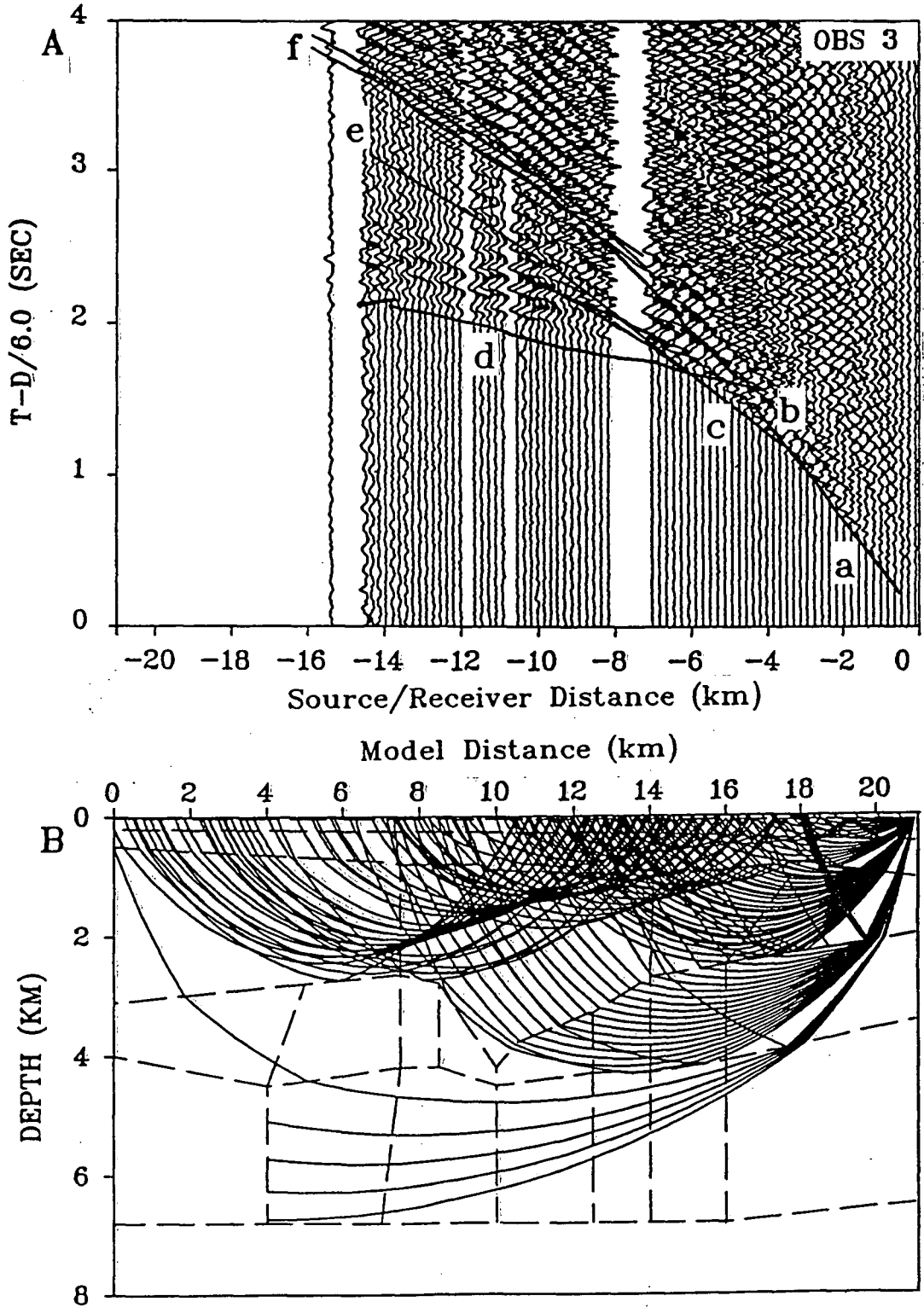

Figure 4.11 Data for OBS 3 reverse profile (A) and ray tracing diagram for OBS 2—OBS 3 sub-model (B). Arrivals e and f correspond to the complex set of internally reflecting ray groups, (B), introduced to model the prominent secondary arrivals in (A) (see text for explanation).

was accomplished by thinning the underlying volcanic unit. A further thinning of this unit was then required to match the low apparent velocity of the arrivals from this layer, curve **d**. A velocity of 4.8 km/s was required and would seem reasonable, as the depth of burial decreases beneath OBS 3. At greater depths, the velocity increases to the 5.0 km/s value observed for the forward profile. The theoretical seismograms (Figure 4.12) match the amplitudes for both the **c** and **d** arrivals. The cutoff in the amplitude of the arrivals for branch **c** show very good agreement for this case. The undulating nature of the arrivals (curve **d**), as modelled by rays through the volcanic layer, was achieved by slight variations of the upper boundary of the 2.25 km/s layer and the upper surface of the Tertiary volcanics.

Unfortunately, the airgun malfunction referred to in the previous sections is also responsible for the premature end of the seismic traces at the western end of the record section. Rays traced through the model, Figure 4.11B, sparsely sample a region of high velocity (5.9 km/s). A portion of the travel-time curve for this sparse group of trays is indicated by the very short solid line near the end of the data. The complete travel time curve for this ray group was omitted beyond the range of the recorded data.

The clear distinct secondary arrivals recorded by this OBS provided a good opportunity to investigate the nature of these arrivals (see arrivals along curves **e** and **f**). The record sections for this and other marine surveys have been found to exhibit these secondary arrivals. The amplitudes are relatively strong and the arrivals appear as multiples of the near offset primary arrivals. They also exhibit some move out, similiar to that observed for reflections. These events are subsequently interpreted as multiple refractions, generated when the refracted energy was internally reflected during its upcoming travel path from a boundary with a large velocity contrast across it. Three of

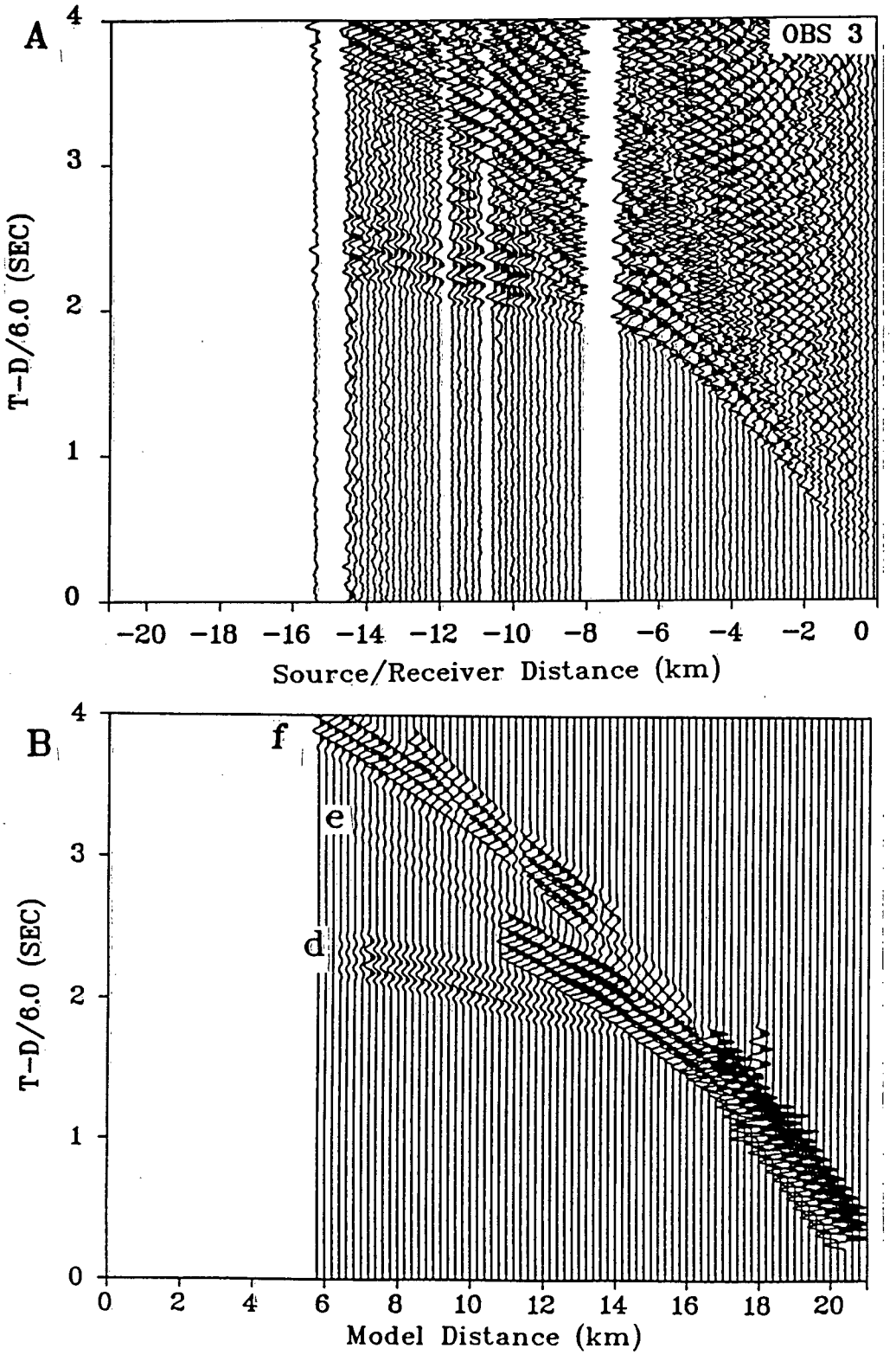

Figure 4.12 Comparison of data for OBS 3 reverse profile (A) and synthetic seismograms (B) computed for ray tracing diagram in figure 4.11B. Arrivals labelled **d**, **e** and **f** correspond to similiarly labelled travel time curves in figure 4.11A.

these boundaries can be found in typical marine surveys: the air–water interface, the water–sediment interface and the sediment–basement interface.

The group of curves, labelled **f**, are the travel time curves for rays internally reflected from the air–water interface and the sediment–water interface. The amplitudes of these arrivals are strong and persist for all displayed traces (Figure 4.12B). The result of reflecting the energy refracted through the 2.7 km/s layer, from the interface between it and the overlying layer, matches the weaker of the secondary arrivals on the data (see curve **e**).

The arrivals labelled on the synthetic seismogram correspond to the curves shown in Figure 4.11A . The amplitudes for the **e** and **f** arrivals match the relative amplitudes of the secondary arrivals in the data remarkably well. The weaker amplitudes for arrivals labelled **e** are expected since the contrast for this internally reflected set of rays was smaller than that for the air–water or water–sediment interface.

The modelling of these secondary arrivals gives an added degree of confidence to the models since the model is now doubly sampled for some of the upper units. In general, theoretical travel time curves matched observed arrivals to within the error of picking the first breaks for these arrivals. The worst case showed a misfit of no more than $\pm 0.20s$ for the secondary arrival fits.

4.4.3 Summary

The velocity profile cube for this sub-model is shown in Figure 4.13. Seven profiles were selected along the model since it exhibited large lateral velocity variations. Geological interpretation of the various units is shown; the units follow continuously from the OBS 1–OBS 2 sub-model considered in section 4.3 . The lateral velocity variations

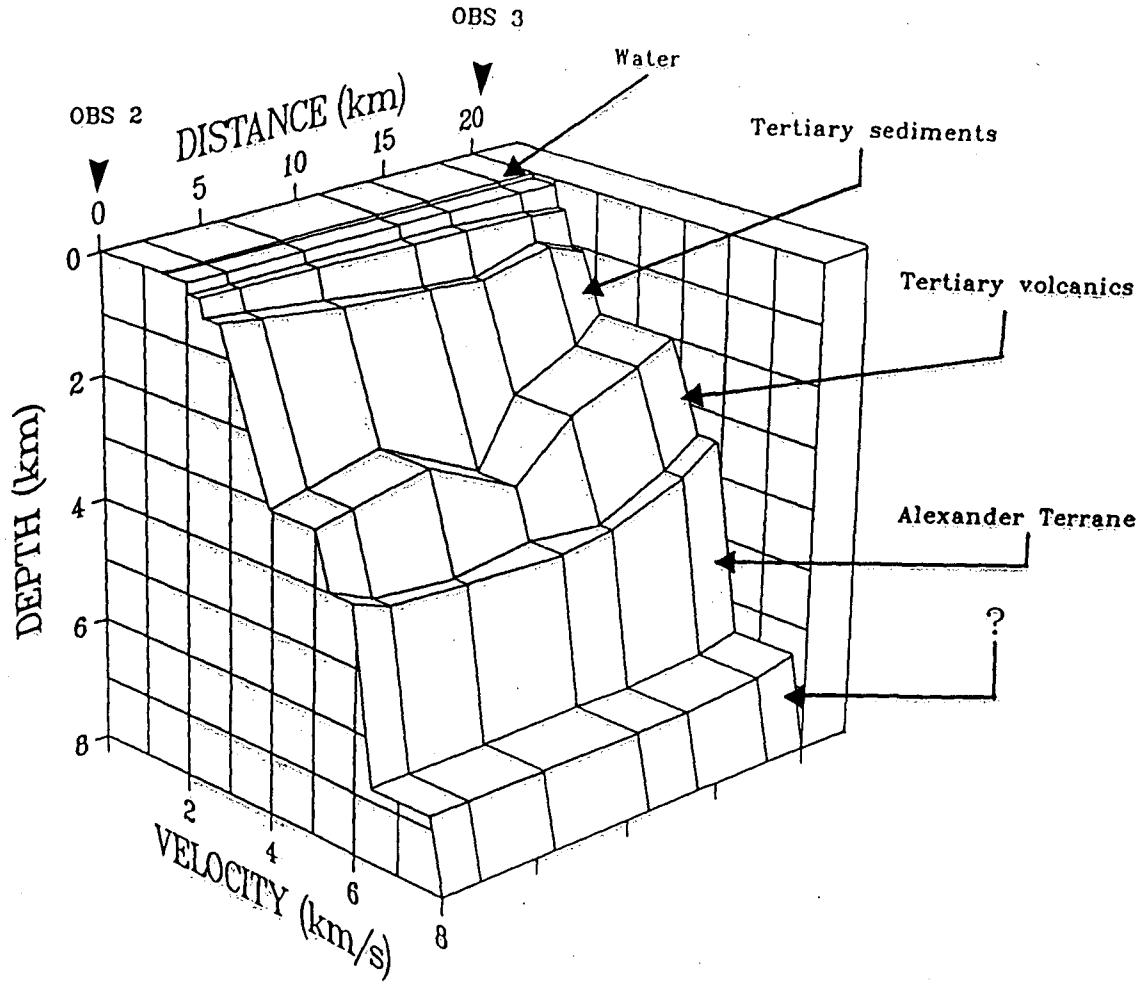

Figure 4.13 Velocity cube for OBS 2—OBS 3 sub-model. Seven velocity versus depth profiles were selected from the sub-model (see figure 4.6 for explanation).

can be followed easily in this display. The thinning of the Tertiary volcanic layer can be seen as the 4.8 to 5.0 km/s velocities shift to greater depths. Other features also become evident — the upper sedimentary layers thicken and the thicker sedimentary unit begins to show less of a velocity contrast with the overlying thin units. As with the previous sub-model, the lower unit, indicated by the ?, is not defined for this sub-model.

4.5 OBS 3—OBS 4 Sub-model

This third and final sub-model is located between 41 km and 62.5 km *MD* in Figure 4.1. The forward and reverse profiles recorded across this segment of the airgun line contain several striking anomalous features and a large noise level. One would expect to see unusual events in the data as the subsurface structure has been shown to change rapidly at the eastern margin of the basin (Shouldice, 1971, 1973; Stacey and Stephens, 1969; Yorath and Cameron, 1982; Young, 1981). However some features were not anticipated. Modelling for a consistent travel time and amplitude match for both the forward and reverse profiles proved to be difficult. This was due to the obvious differences in the data sections recorded at OBS 3 and OBS 4 (Figures 4.14A and 4.16A).

4.5.1 Forward profile

The data for the forward profile and the ray trace model are shown in Figure 4.14. Strong amplitudes extend to 9 km *SRD* for the refracted arrivals. The amplitude suddenly drops off, then a delayed signal appears between 14 and 18 km *SRD*. These characteristics are shown more clearly by the hydrophone component (Figure II.11, Appendix II).

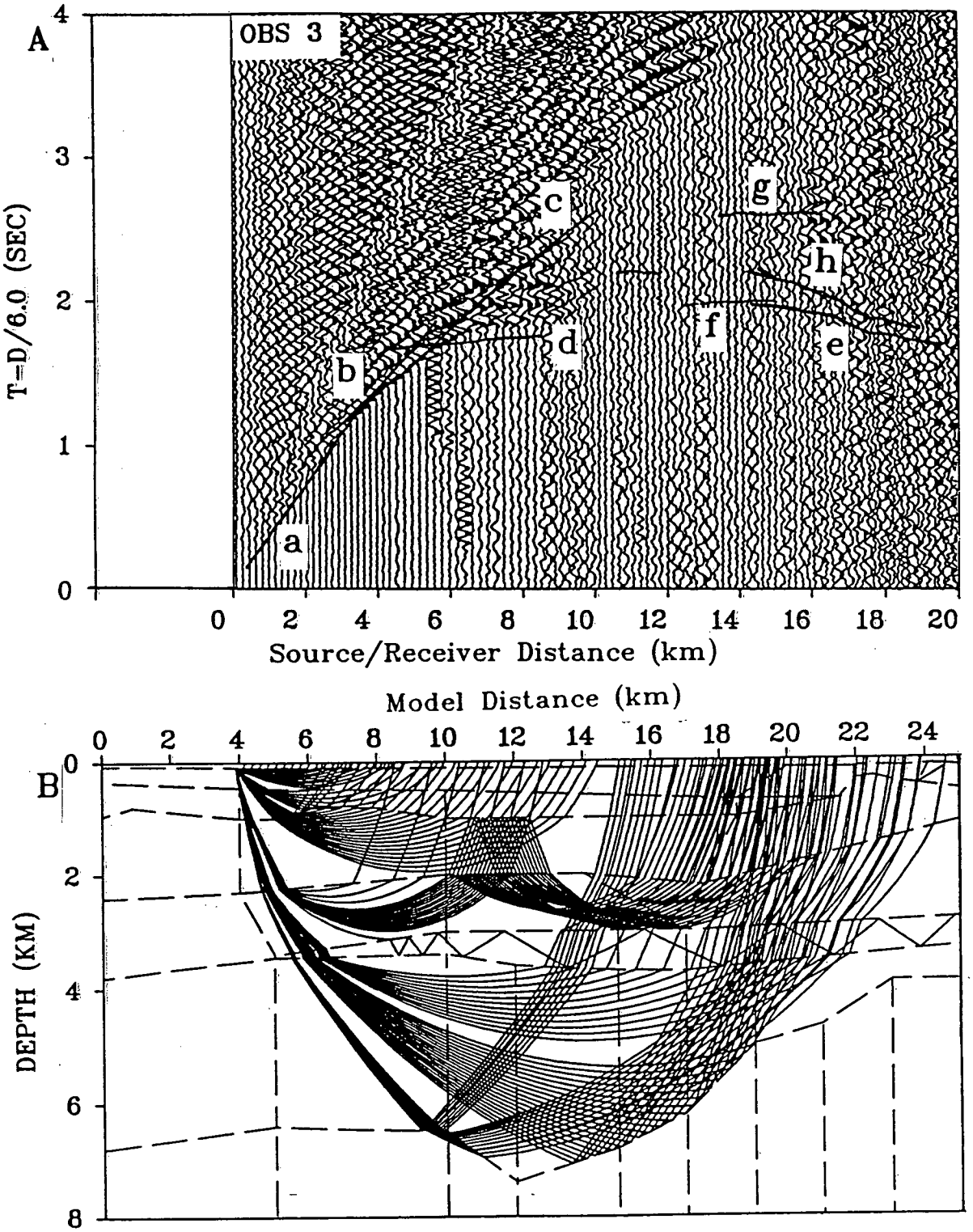

Figure 4.14 Data for OBS 3 forward profile (A) and the ray tracing diagram for OBS 3—OBS 4 sub-model (B). Some reflected refraction ray paths have been included in an attempt to model particular features (see figure 4.2 and text for explanation).

Modelling for the sedimentary layers proceeded as before and the traveltimes are shown, curves a and b, in Figure 4.14A. The velocity of the middle sedimentary unit, that is truncated by the thick Tertiary unit, required a lower velocity of 2.2 km/s. The velocity contrast between the upper layers and this middle unit diminishes to zero towards the eastern end of the model due to the velocity gradient and increasing thickness of the uppermost layer (see Figure 4.19). Rays through the lower sedimentary unit, the Tertiary sediments, (velocity 2.6 km/s) generate the theoretical arrival branch c. In this part of the model, the interpreted Tertiary volcanic layer is shallower, as required by the travel time characteristics of the data and the isopach information (Shouldice, 1971). Curve d shows the theoretical travel times for this unit.

The sudden decrease in the amplitude at 9 km *SRD* necessitated the introduction in the model of a feature which could cause the observed characteristic. A faulted block or a low velocity layer are typical mechanisms chosen to cause the desired effect. The fault solution was considered but did not yield a model consistent with the reverse profile. Furthermore, there is no evidence to support major faulting in this region. A low velocity zone which pinches out to the west was introduced immediately below the Tertiary volcanics. The synthetic seismogram section (Figure 4.15B) shows that the amplitude for the arrivals for phase d drops off sharply at about 9 km it SRD, as observed on the data section. A velocity of 3.5 km/s was chosen for this low velocity zone to be consistent with a similarly interpreted low velocity layer from the Charlotte sub-basin (Clowes and Gens-Lenartowicz, 1985). The low velocity/thickness combination was consistent with the delay observed in the arrivals beyond 11 km *SRD*. In addition, the introduction of the low velocity zone was consistent with data from the reverse profile as discussed in the next section.

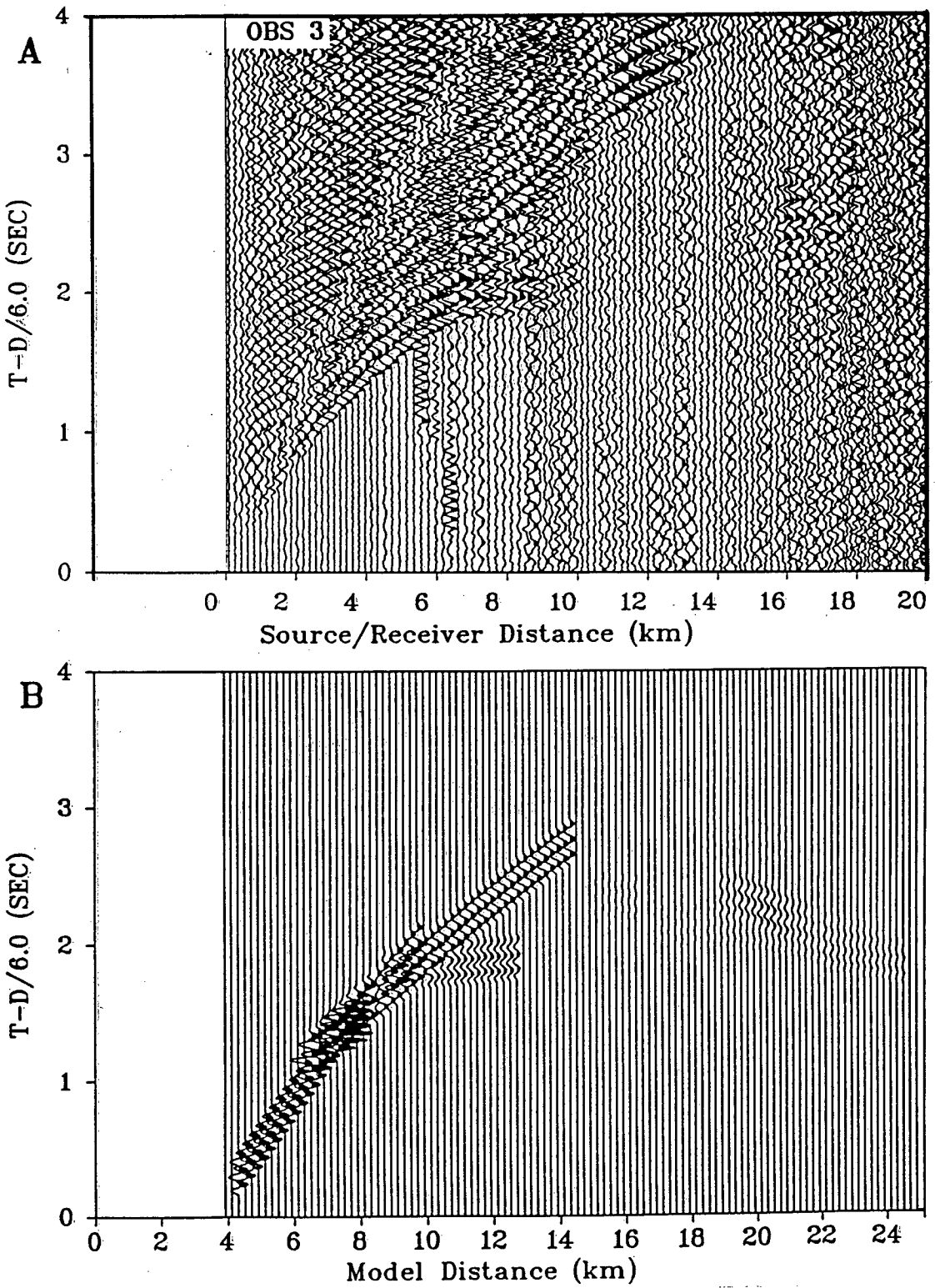

Figure 4.15 Comparison of data for OBS 3 forward profile (A) and synthetic seismograms (B) computed for ray tracing diagram in figure 4.14B (see figure 4.3 for explanation).

The somewhat isolated burst of high amplitude energy observed on the record section at about 2.5s and between 14 and 15 km *SRD*, is more pronounced on the hydrophone component (Figure II.11, Appendix II). Simple refractions through the Alexander terrane (5.9 km/s layer) below the low velocity zone did not generate amplitudes corresponding to those on the observed section. Consequently the burst of energy was interpreted to represent a local focussing effect. An attempt was then made to focus the energy by selecting a number of travel paths to give the same travel times. First, rays were internally reflected from the base of the 2.2 km/s layer. Travel times for this ray group are shown in Figure 4.14A as curve **g**. But because of the time spent in the Tertiary sediments and the low velocity contrast between this layer and the 2.2 km/s layer, these arrivals were delayed by too much and had weak amplitudes (Figure 4.14A and 4.15B). Next rays were reflected from the base of the sediment–basement boundary (Figure 4.14B and curve **h** in Figure 4.14A). These arrivals represent the portion of curve **h** out to 16 km *SRD* and, as can be seen in Figure 4.15B, contribute the most to the large amplitudes that are observed.

The direct arrivals through the Alexander terrane, curve **e**, are modelled for the weak amplitude arrivals observed at this range. The hydrophone component shows the arrivals more clearly, but the first breaks could not be determined because of the low amplitudes and the noise. These low amplitudes are evident as first arrivals on the theoretical seismograms and are clearly not responsible for the focussed energy at this range . Therefore, rays were reflected from the base of the Alexander Terrane to augment those on curve **h**. These reflections form curve **f** and the rest of curve **h**, with some overlap between the two groups making up curve **h**. The lower set of reflected energy contribute to the overall amplitudes observed in the theoretical seismograms. A portion of these rays, from the deep reflecting group, actually refract through the

uppermost part of the unit (7.5 km/s) where velocities and gradients are unconstrained by the data.

The concave shape of the lower reflecting boundary is significant for the resulting travel times. In order to get an appropriate set of arrivals, the structure had to have a concave shape. In the model without this shape, the combination of the thinning of the sedimentary layer and the shallowing of the Tertiary volcanic unit caused the theoretical arrivals to have larger apparent velocities. To match the apparent velocity of the observed arrivals, a means of increasing the travel times as the offset increased was needed. The concave structure provided the necessary mechanism and focussed the energy. However, the travel times do not appear to match any specific set of arrivals in the energy burst (Figure 4.14A). Nevertheless, the theoretical seismograms do match the overall characteristics of the observed seismic section (Figure 4.15). It is this observation which leads to the conclusion that these arrivals represent a focussing of energy, most likely due to constructive and/or destructive interference from various arrivals.

4.5.2 Reverse profile

The reversed profile was modelled simultaneously with the forward profile. The data and velocity structure, with traced rays, are depicted in Figure 4.16. Noise levels were relatively high for this data set and required analysis of record sections for all three components. Bandpass filtering was applied when necessary. The modelling of the primary arrivals between 0 and -8 km *SRD* followed that for the forward modelling but now, arrivals from the uppermost sedimentary unit, are immediately followed by those from the thick Tertiary sediments (curves a and b) due to the truncation of the middle unit. To model the first arrivals, curve a, and generate the necessary velocity

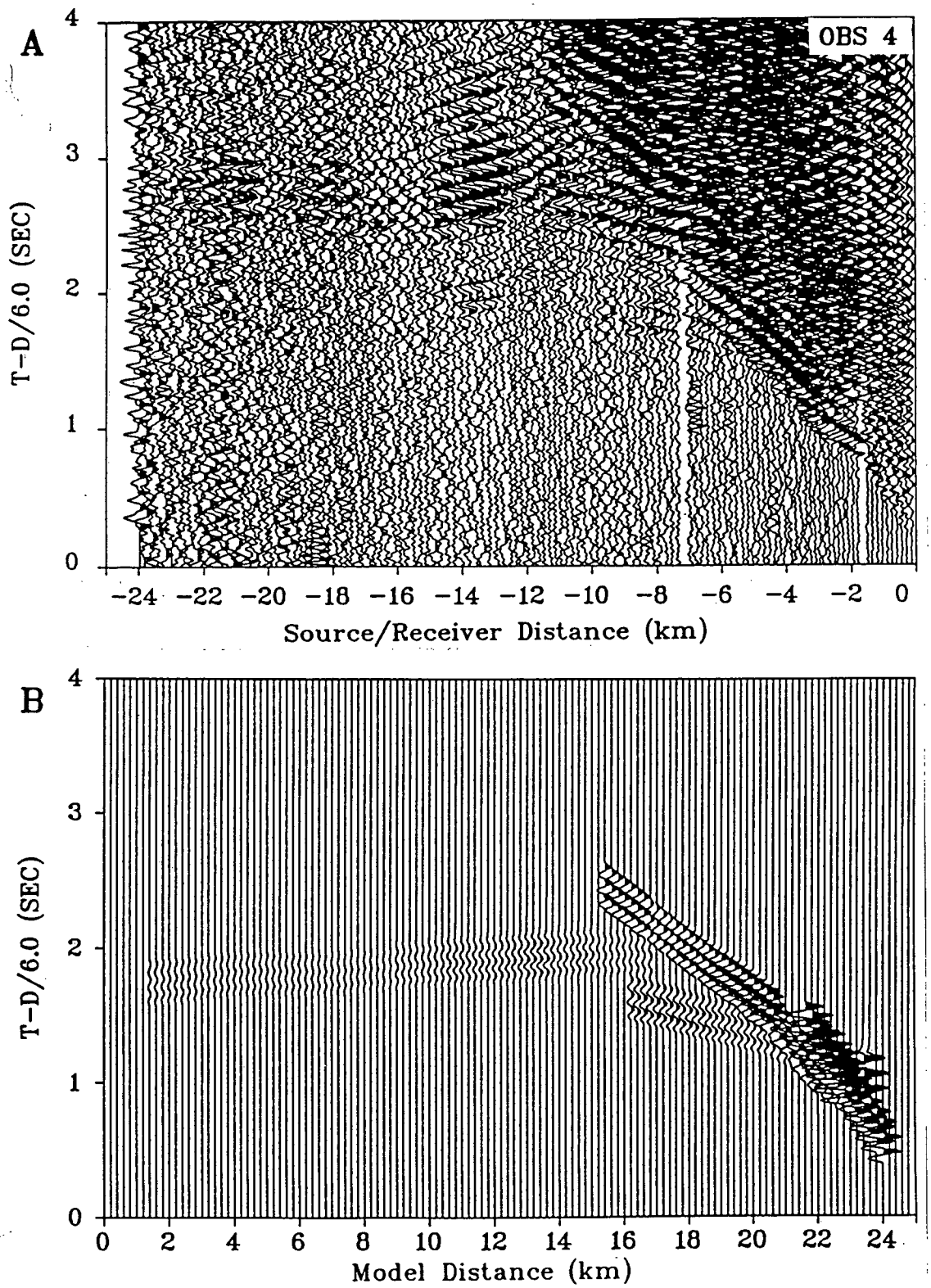

Figure 4.16 Data for OBS 4 (A) and ray tracing diagram for OBS 3—OBS 4 sub-model (B) (see figure 4.2 for explanation and the text for an explantion of events labelled D).

contrast to model the bump-like feature observed in the data between 2 and 4 km *SRD*, the velocity of the sediments below OBS 4 were decreased to 1.9 km/s. By directing the rays through a structural high on the Tertiary sedimentary layer after travelling through the 1.9 km/s layer, the arrivals experience an increase in apparent velocity, curve b. This is immediately followed by a decrease in apparent velocity as the rays enter the upper 2.0 km/s layer. The theoretical seismograms match the bump-like feature well in amplitude and shape of the travel time curve (Figure 4.17). The 2.2 km/s layer is pinched out by the rise of the structure representing the Tertiary sediments. The extension of b as a secondary arrival results from ray paths through the Tertiary sediments, the 2.6 km/s layer.

The computed travel times, curve c, for the 4.8 km/s layer are truncated by the extension of the low velocity layer introduced in the forward profile. The amplitude of the arrivals in the data do not appear to drop off as fast as those from the forward profile but this cut off is also supported by the filtered hydrophone component (Figure II.12, Appendix II). Theoretical amplitudes for the arrivals from the Tertiary volcanics are larger than the first break arrivals for the observed data. However, for the hydrophone component, the amplitudes of the arrivals, c, are more clearly seen even though the signal is at the noise level. Therefore a gradient of 0.70 km/s/km was chosen to maintain a balance between the amplitude observed on the vertical component and those observed on hydrophone component.

A time delay can be observed for the arrivals matched by curve d. The low velocity layer may be the Upper Cretaceous sediments that were deposited across the suture zone defined by Yorath and Chase (1981) as the *post suture assemblage*. As mentioned in section 4.5.1, a similiar low velocity layer was required in a model from the Charlotte

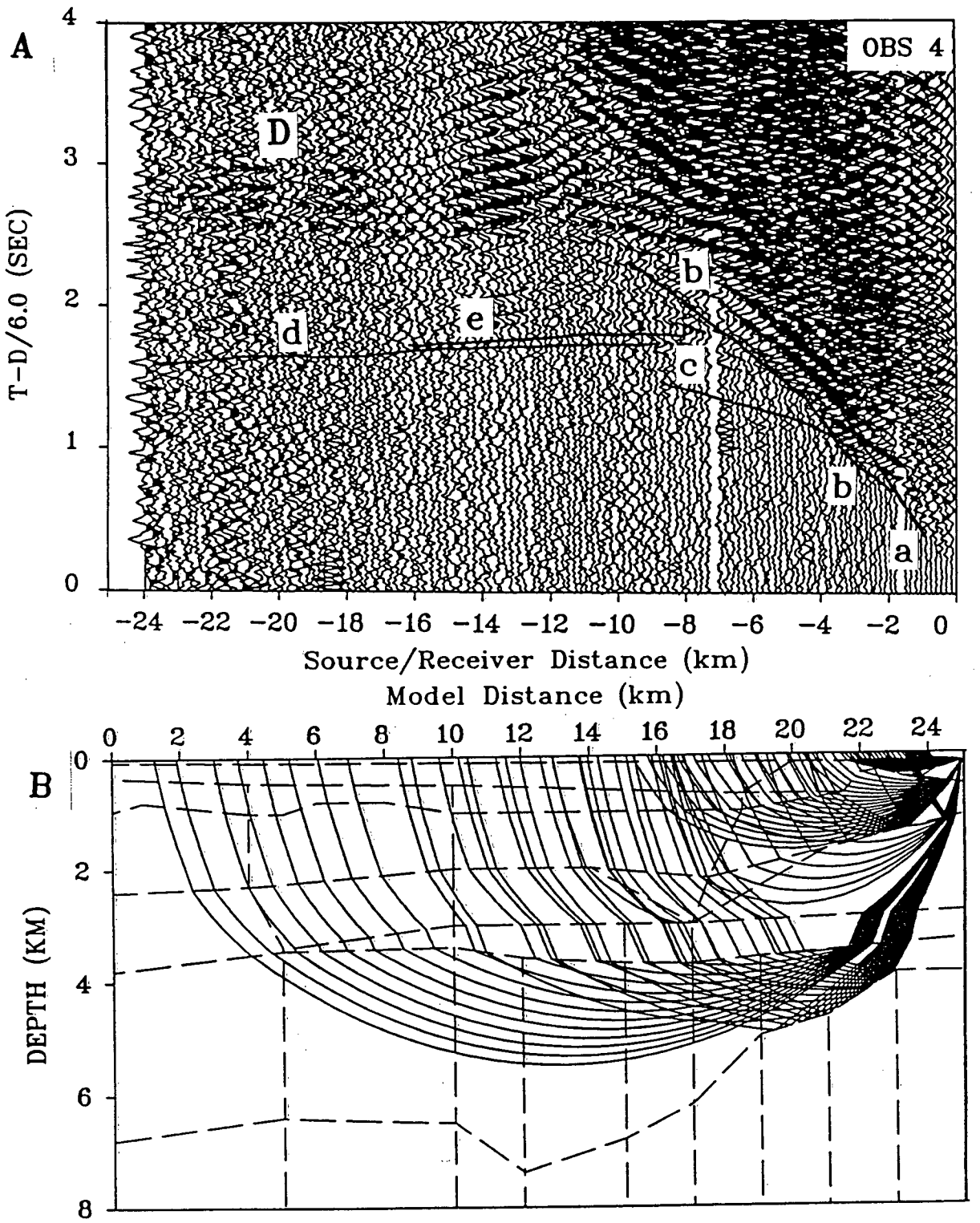

Figure 4.17 Comparison of data for OBS 4 reverse profile (A) and synthetic seismograms (B) computed for ray tracing diagram in figure 4.11B (see figure 4.3 for explanation).

sub-basin and has been interpreted as the *post suture assemblage* (Clowes and Gens-Lenartowicz,1985).

The theoretical travel time, curve **d**, was computed by tracing rays through the block interpreted as the Alexander terrane. Poor signal-to-noise ratios prevented an accurate determination of the first breaks for this branch. The hydrophone component of the data was bandpass filtered between 5 and 12 Hz and succeeded in bringing out the primary arrival branch (Figure II.12, Appendix II) which aided in the final determination of its position (curve **d**). As shown on the theoretical seismograms (Figure 4.17B), the slight increase in amplitude has been modelled fairly successfully by the addition of reflections from the top of the 7.2 km/s layer (curve **e** on Figure 4.16A)

The data in Figures 4.16A and 4.17A show a strong set of secondary arrivals, event **D**, which have not been modelled explicitly. This large amplitude event ranges from 13 to 24 km *SRD* at a reduced time of 2.5 seconds. To explain the nature of this event more easily, the order in which the investigation proceeded will be described.

Initially the event was thought to represent a strong set of primary arrivals and were modelled as such. However, the resulting model was found to be inconsistent with the interpretation of the forward profile. The general structure of the units below the sediments were required to have an eastward dip, which is not in accord with the accepted regional geology of the area. Upon a closer examination of the data, weak arrivals parallelling event **D** with an arrival time approximately 0.8 seconds earlier were noted and subsequently modelled as described. This raised the question—what situation will give rise to weak primary arrivals followed by large amplitude secondary arrivals? The first attempt to solve this problem was to model the earlier events as head waves and the secondary event as reflections from the base of the layer generating the head

waves. This solution failed to generate the observed amplitudes and the parallel nature of the two events.

A solution which adequately explained the observations evolved following examination of the three components for this data set. Figure 4.18 shows the three components of data for OBS 4 within the range and time window of interest. The vertical component, Figure 4.18c, and the horizontal component, Figure 4.18b, were plotted with the same scale factor which is three times greater than the factor used for the hydrophone component, Figure 4.18a. Comparing Figure 4.18 b and c, the large amplitude event **D** is stronger and more coherent on the horizontal component. Comparing Figure 4.18a and 4.18c the weak primary arrivals, **d** are observed to extend across both record sections. Event **d** is not seen on the horizontal component, while event **D** is not present on the hydrophone component. Finally the parallel nature of the two events suggests a relationship between them and the travel-time difference between them is consistent with wave conversion at the basement sediment basement. These observations are diagnostic of converted S-wave arrivals. There is a larger horizontal component of the incoming wave and it is not transmitted through the water. A review of the literature supports the premise that the later, stronger amplitude arrivals could be converted phases. Converted S–wave arrivals have been shown to be characteristic of a number of marine seismic refraction surveys (White *et al.*, manuscript in preparation 1986; Cheung and Clowes, 1981; Au and Clowes, 1984), although all of these were in deep water environments. White and Stephens (1980) reviewed the properties for shear wave conversion. Mode conversion between P and S waves occurs when the P or S wave encounters an interface with large velocity contrast. In marine environments there are two such interfaces, the water–sediment interface and the basement–sediment interface. The P to S

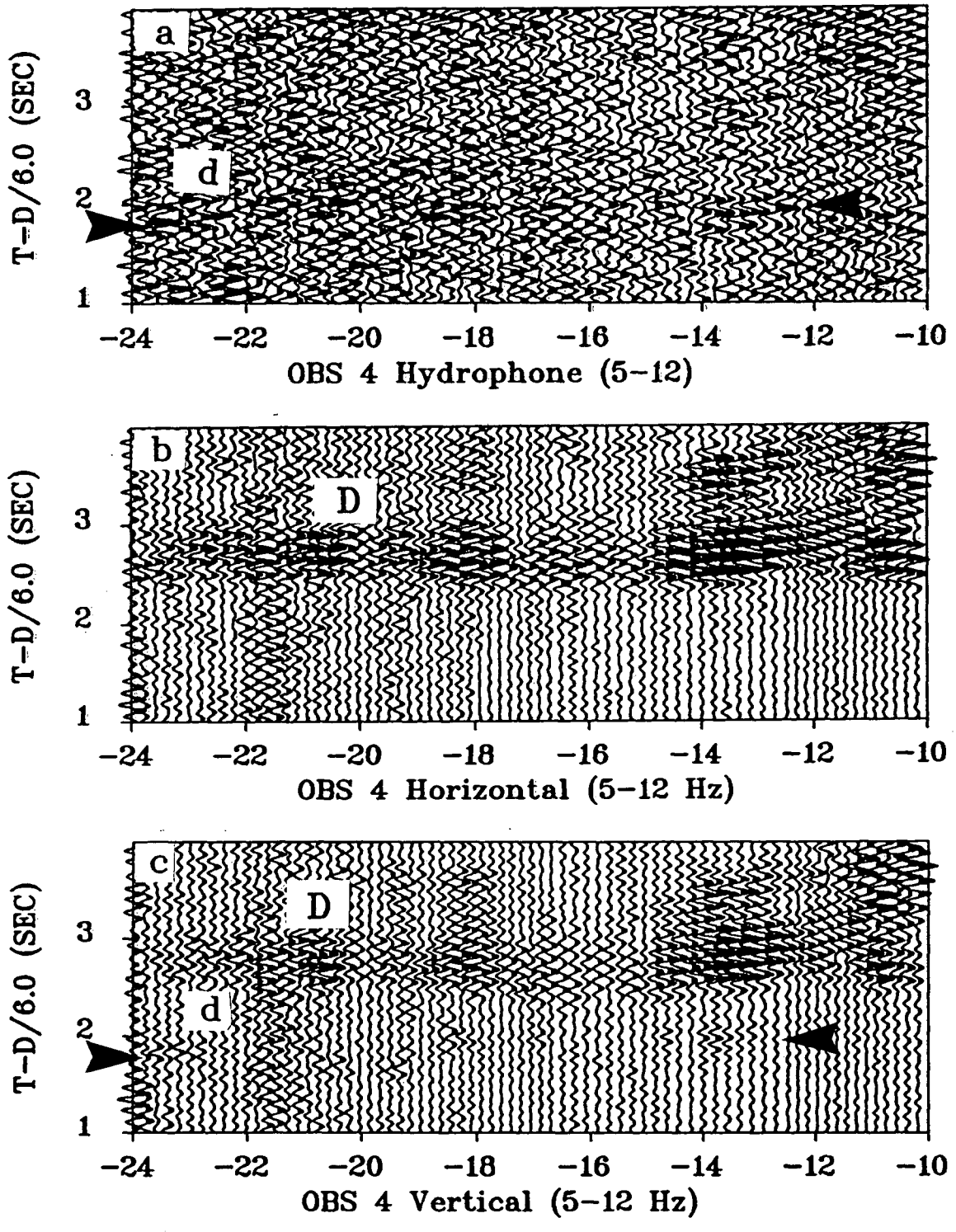

Figure 4.18 Comparison of filtered hydrophone (a), horizontal (b), and vertical (c) components for OBS 4. The source/receiver distance is plotted along the horizontal axis. The data is plotted from 1 to 3 seconds in reduced time format. Primary arrival events are labelled with **d** and secondary P to S converted phases are labelled by **D** (see text for explanation).

conversions at the basement–sediment interface have been observed to yield S-wave arrivals that are much larger than the P-wave arrivals (Cheung and Clowes, 1981; White *et al.*, manuscript in preparation 1986). Cheung and Clowes used these large amplitude arrivals to determine the position of the weak P-wave arrivals. White *et al.* modelled these conversions using 1-D WKBJ synthetic seismograms which included an option for phase conversions (Chapman, 1978). Where conditions enhance the conversion of P to S waves for the basement–sediment interface, they reduce the efficiency for S to P wave conversions at the water–sediment interface (White and Stephens, 1980). The lack of a doubly converted phase (P to S to P) on the hydrophone may be due to such an effect.

4.5.3 Summary

Figure 4.19 shows the velocity cube display for this sub-model along with the geological interpretation for the major units. The Tertiary sediments thin substantially as the Tertiary volcanic basement structure rises. This factor may account for the presence of the P to S wave arrivals seen only on OBS 4. The low velocity unit has been interpreted as Upper Cretaceous sediments. This unit pinches out at 5.0 km *MD*. This pinch-out was required as there was no evidence for a low velocity layer in the adjoining sub-model for OBS 3–OBS 2. The Alexander Terrane is nearly truncated by the lowermost unidentified unit, for which only the position of its upper surface is even partly constrained by the data.

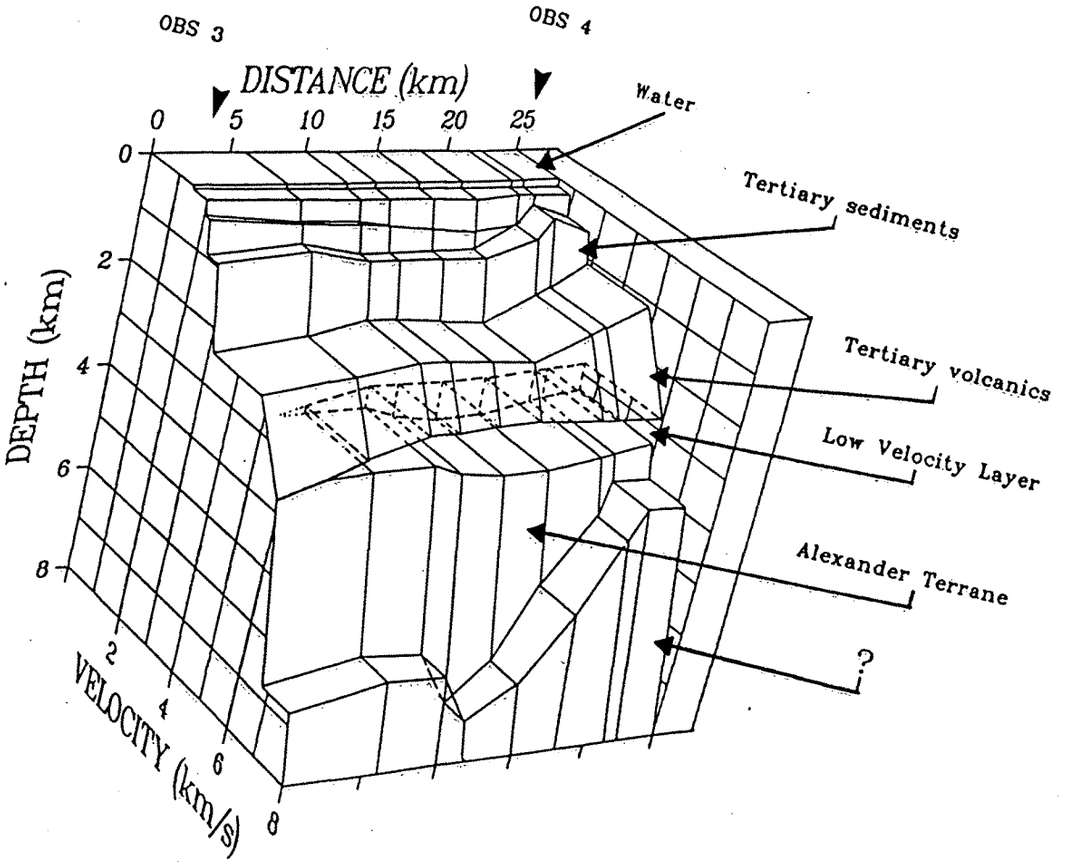

Figure 4.19 Velocity cube for OBS 3—OBS 4 sub-model. Nine velocity versus depth profiles were selected from the sub-model (see figure 4.6 for explanation).

CHAPTER V DISCUSSION AND CONCLUSIONS

5.1 Discussion of the Final Composite Model

The final velocity model was compiled from the three sub-model segments of Chapter IV . Figure 5.1 shows the composite model with a 5:1 vertical exaggeration and the same model with no vertical exaggeration. A legend, relating the various units to the velocities, appears below the model. During the compilation of the final model from the three submodels, minor discrepancies occurred at their common boundaries beneath OBS2 and OBS3. The composite model was adjusted to make the sub-model boundaries all consistent. The various individual velocity blocks, shown in Figure 4.1, have been replaced by average velocities and gradients representing the major units.

The interpretation is non-unique, but is based on a careful evaluation of the comparison of observed and theoretical travel times and amplitudes for reversed profiles. Small lateral variations in velocity and gradient appear to be necessary although their representation by discrete boundaries in Figure 4.1 is an artifact of the model input for the asymptotic ray theory modelling program.

The thickening of unit D at about 30 km distance is a feature introduced to account for amplitudes and apparent velocities of primary and secondary arrivals on both the forward and reverse profiles for OBS 2–OBS 3. This seemed to be a necessary feature of the model as did the introduction of large velocity gradients (up to 0.5 km/s/km). Clowes and Gens-Lenartowicz (1985) used similiar gradients for a lower sedimentary unit for one of their models from Queen Charlotte Sound and the sonic logs (section 4.3.3) support the existence of large and varying gradients for the sediments. Similiarly the rise of unit E to the east and the existence of a low velocity zone (unit F) below are features

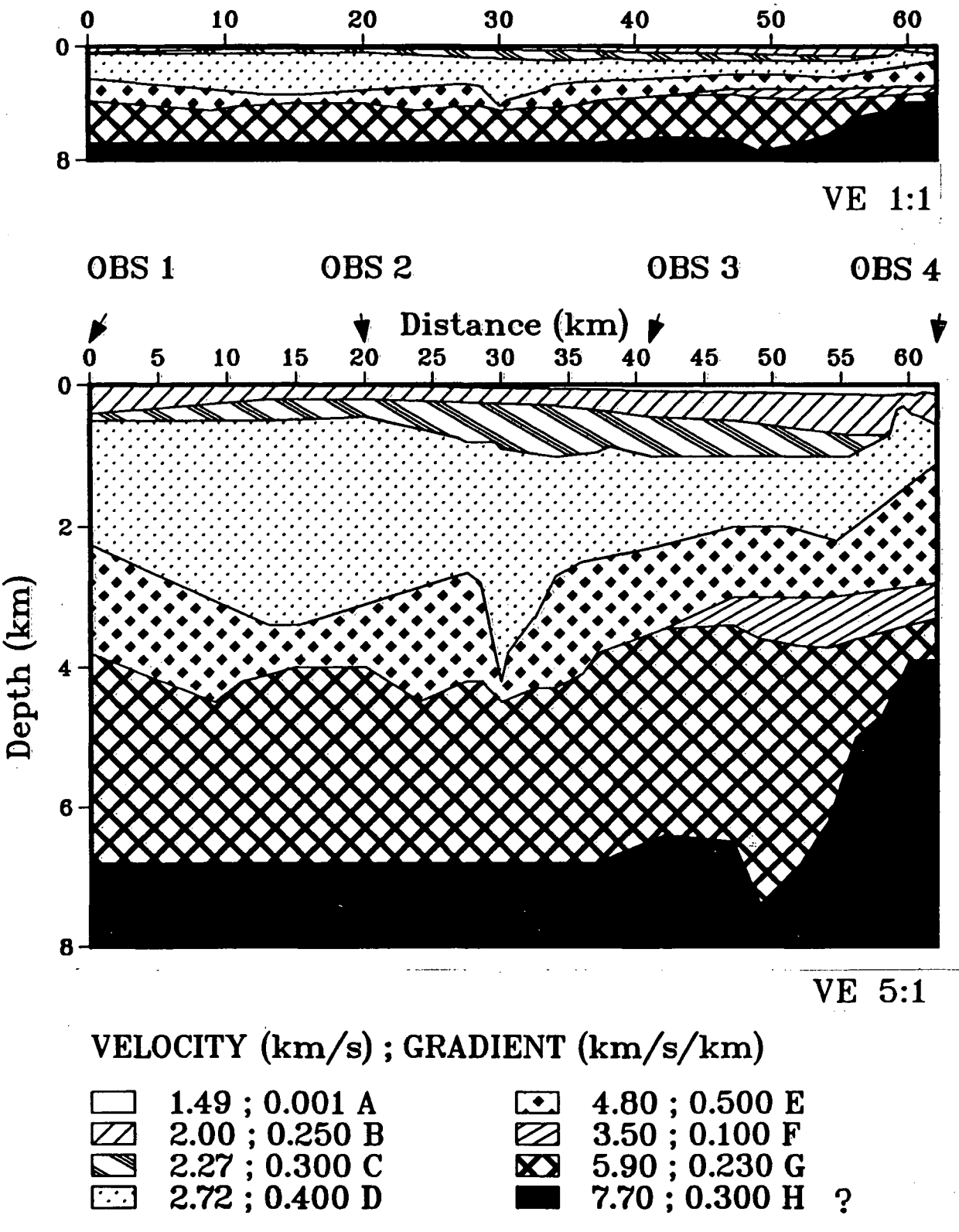

Figure 5.1 Final composite structural velocity model. The model is displayed with no vertical exaggeration (top insert) and a vertical exaggeration of 5:1 . The legend at the bottom of the figure related the symbols for the structural units to the velocities and gradients for those units. Features in this model below 5.0km are either poorly constrained or completely unconstrained (see text for explanation).

of the model which were introduced to account for particular data characteristics. The velocity for unit **E** was modelled as 4.8 km/s with an average gradient of 0.5 km/s/km. This gradient decreases from large values in the east (0.7 km/s/km) to smaller values (0.2 km/s/km) in the west. The velocity for the upper surface has been indicated as 4.8 km/s, but increases to 5.0 km/s with increasing depth of burial.

The introduction of low velocity layers into models developed from seismic refraction interpretations presents the interpreter with a greater degree of freedom in determining the final model. This arises because low velocity zones represent a hidden problem for seismic refraction methods. The same delayed travel-time can be generated for many velocity and thickness combinations. To achieve a common baseline for the comparison of these results with others a velocity for the low velocity layer was chosen to match that used by Clowes and Gens-Lenartowicz (1985) in their model. By using similiar velocities, the comparison of the model described here with that for Queen Charlotte Sound will not be diminished by the non-uniqueness associated with the inclusion of the low velocity zone.

OBS 3–OBS 4 reverse profile (Figure 4.16 and 4.17) shows an unequivocal arrival with an apparent velocity of 6.0 km/s. As this is the only profile where this phase exists, unit **G** is poorly defined elsewhere and essentially inferred. Unit **H** is not defined between 0 and 40 km and only poorly defined beyond that range. Reflections from the top of the layer beyond 40 km were introduced to satisfy particular events for OBS 3–OBS 4 interpretation but the unit itself was never sampled. Velocities were chosen to produce a reflection coefficient necessary to generate reasonable amplitudes to match the energy burst discussed in section 4.5.1 . In summary, the lower 3 to 4 km of the model shown in Figure 5.1 are either poorly constrained or unconstrained.

UNIT	*STRATIGRAPHIC INTERPRETATION*
A	*Water*
B	*Pleistocene Sediments*
C	*Pleistocene and/or Pliocene Sediments*
D	*Tertiary Skonun Sediments*
E	*Tertiary Masset Volcanics*
F	*Upper Cretaceous Sediments*
G	*Paleozoic Alexander Terrane*
H	*Plutons ?*

Table 5.1 Summary of stratigraphic interpretation.

Table 5.1 summarizes the stratigraphic interpretation of the various units. Units B and C can be considered collectively, especially in light of the loss of a velocity contrast between 50 km and 58 km where the lower one pinches out. These have been interpreted as Pleistocene and/or Pliocene sediments laid down in a nearshore depositional environment. The maximum thickness reaches approximately 1.0 km between 30 and 40 km. The velocities and the combined thickness of these units are similar to models from Queen Charlotte Sound (Clowes and Gens-Lenartowicz, 1985). Unit D has been interpreted as the Tertiary Skonun Formation (Sutherland Brown, 1968; Shouldice, 1971, 1973). These are Upper Miocene sediments deposited in near shore marine and non-marine environments. The Tertiary sediments represent the thickest sedimentary unit for the Hecate Strait model, reaching a maximum thickness of approximately 3.0 km. The combined maximum thickness for all the sedimentary units is about 4.0 km, similiar to that defined by Shouldice (1971, 1973) for Hecate sub-basin and Clowes and Gens-Lenartowicz (1985) for Charlotte sub-basin.

Unit E has been interpreted as the Tertiary Masset formation which consists of subaerially erupted volcanics. This unit also exhibits features of a buried erosional surface. Using information collected from the wells in Hecate Strait by Shouldice (1971, 1973),

Yorath and Chase (1981) suggest that this formation had been previously uplifted and eroded between Upper and Lower Miocene times. The Tyee well (see Figure 1.1) showed no Tertiary Masset volcanics; however it did penetrate a high velocity material which has been interpreted by Shouldice (1971, 1973) as a Paleozoic intrusive. This is consistent with the model presented here since Shouldice (1973) indicated that erosional channels had removed the overlying material. Tertiary Masset volcanics have been logged in other wells and have been inferred from reflection seismic data (Shouldice, 1971, 1973). Clowes and Gens-Lenartowicz (1985) have inferred Tertiary volcanics beneath Queen Charlotte Sound based on a similar refraction survey. These range in thickness between 1.5 and 3.5 km as compared with 0.2 and 1.8 km for the volcanics beneath Hecate Strait. The velocities assigned to this unit (4.8-5.0 km/s) compare favourably with the 5.2 km/s velocity for the Tertiary volcanics beneath Queen Charlotte Sound. The isopach for Hecate Strait (Figure 1.5) shows thinning of the sediments in the west to less than 0.1 km. The isopach is not well defined in this area and the results here would favour an eastward shift for the basin edge.

Unit F, which only appears beneath the Tertiary volcanics at the eastern end of the model, was interpreted as the Upper Cretaceous Queen Charlotte Group of the post suture assemblage (Yorath and Chase, 1981). They recognized Upper Cretaceous sediments (their post suture assemblage) in the Tyee well which lies close to the air-gun/OBS line. They also observe that no Tertiary volcanics were penetrated by this well. The present study did not require the extension of the low velocity zone from the eastern end to the portion of the model near the well, but the velocity unit interpreted as the Tertiary volcanics is required to extend across the basin. The Tertiary volcanics, where present in the Hecate sub-basin, unconformably overly the Upper Cretaceous

sediments (Sutherland Brown, 1968; Shouldice, 1971, 1973) and it is not unusual for the latter unit to be absent.

Unit G has been interpreted as the Paleozoic rocks of the Alexander Terrane which are believed to underly the Hecate sub-basin. The velocity and gradient for this unit were modelled as 5.9 km/s and 0.23 km/s/km, respectively. The velocity compares favourably with the value of 6.0 km/s from the sonic log of the Tyee well (see Figure 4.2). Clowes and Gens-Lenartowicz (1985) define a velocity of 6.0 km/s for the Mesozoic Wrangellia Terrane beneath Queen Charlotte Sound. Based upon these results, it would appear that the velocities for the Wrangellia and Alexander Terranes are comparable.

Unit H has been tentatively interpreted as representing plutons, but as noted earlier, while its presence is indicated, little can be inferred about its properties. The upper boundary of this unit beyond 40 km appears to have a complex structure which rises abruptly at the eastern end of this model. This is consistent with the results of gravity from a profile coincident with the airgun/OBS line (Stacey and Stephens, 1969). Their interpretation is shown in Figure 5.2 for comparison with the gross characteristics of the velocity model.

5.2 Conclusion

A seismic structural velocity model has been developed for the Hecate sub-basin. This model was found to be consistent with previous studies from Hecate Strait and Queen Charlotte Sound. The interpretaton is also consistent with the geology expected beneath Hecate Strait based on geological structures extrapolated from the Queen Charlotte Islands. The nature of the surface of the Tertiary volcanics suggests an erosional surface similiar to that for the Tertiary Masset volcanics on Graham Island and in the

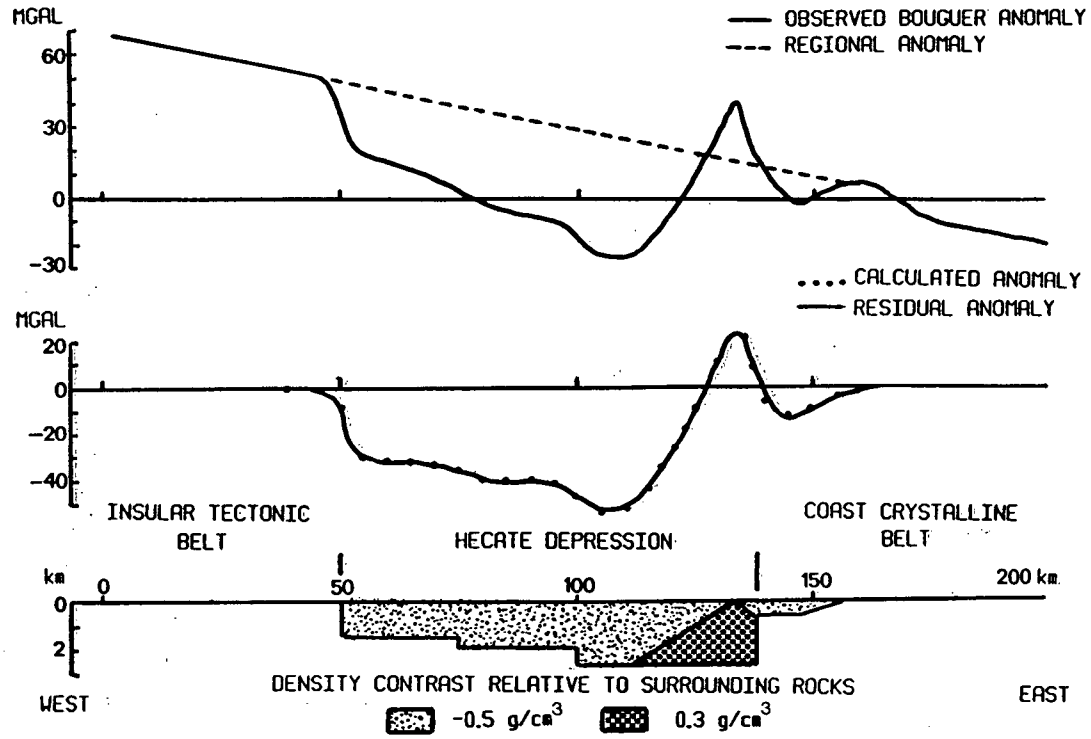

Figure 5.2 Proposed geological structure for Hecate depression based on gravity profile coincident with airgun/OBS line (after Stacey and Stephens, 1969).

Shell Canada Ltd. wells. The extreme thinning of the volcanics below a narrow depression filled with sediments (30 km distance on Figure 5.1) also supports this premise.

Tertiary volcanics are observed on the Queen Charlotte Islands to unconformably overlie Cretaceous sediments. The Cretaceous sediments and the Tertiary volcanics may appear together or with either one absent. Therefore the low velocity Cretaceous sediments observed to occur only at the eastern end of the profile is not inconsistent with available information.

The lowermost unit can only be described in terms of its presence as a complex rising structure at the eastern edge of the basin. The gravity interpretation (Stacey and Stephens, 1969) is very similiar to the gross structure for the velocity model. The gravity interpretation yielded a simple two block model for the Hecate depression. The basin infill was modelled with a density contrast of -0.5 g/cm^3 while the wedge-like block has been modelled as having a density contrast of $+0.3g/cm^3$ with the surrounding rocks. The results of this gravity survey combined with those from the refraction modelling may be indicating geological features which arrive from the collision of Alexander and Wrangellia with the continental margin. On the basis of this supposition, the lowermost unit of the model has tentatively been described as plutons.

The low velocity layer may be representative of the post suture assemblage of Yorath and Chase (1981). This assemblage is discussed in Chapter I as being comprised of Upper Cretaceous sediments of the Queen Charlotte Group. This group contains good reservoir rocks, the Honna Formation, and trapping mechanisms for hydrocarbons within these units themselves and also above them. The low velocity layer, as defined, is located in a favourable position for the accumulation of hydrocarbons. However, the thickness of the overlying Tertiary volcanics could make exploration a costly venture. Furthermore, the thermal history does not seem to favour the generation of oil but only

gas and unfortunately no source rocks are known to exist in the Paleozoic Alexander Terrane (Yorath and Cameron, 1982). A refraction survey from the Charlotte sub-basin (Clowes and Gens-Lenartowicz, 1985) also found evidence for a low velocity zone interpreted as upper Cretaceous sediments.

The Hecate and Charlotte sub-basins appear to be similar in their makeup for the upper units. The Masset volcanics which occur in both areas support the belief that this volcanic episode was very widespread. The Upper Cretaceous sediments of the post-suture assemblage variously appear and disappear irregularly throughout the Queen Charlotte basin. In general the formations appear to be thicker in the Charlotte sub-basin, south of the present study area.

In Chapter III, an independent study involving the inversion of refraction data by the method of wavefield continuation was undertaken. A segment of data from the air-gun/OBS survey, under study as the major part of this thesis, was inverted to obtain the one-dimensional velocity-depth structure. The method was found to produce reasonable 1-D velocity-depth structures for these examples. These findings would support the application of this inversion method to obtain initial velocity versus depth estimates for use by 2-D modelling schemes. For refraction lines along strike, where lateral heterogeneity is less pronounced, the resulting velocity depth models would more closely represent the subsurface structure.

References

Aki, K. and Richards, P.G., 1980, *Quantitative Seismology, Theory and Methods*, **1**: W.H. Freeman and Company, San Francisco, 535 pp.

Berg, H.C., Jones, D.L. and Coney, P.J., 1978, Pre-Cenozoic tectonostratigraphic terranes of southeastern Alaska and adjacent areas, United States Geological Survey Open File Report 78-1085.

Berg, H.C., Jones, D.L. and Richter, D.H., 1972, Gravina- Nutzotin belt-tectonic significance of an upper Mesozoic sedimentary and volcanic sequence in southern and southeastern Alaska, United States Geological Survey, Professional Paper 800-D, pp. D1-D24.

Bessonova, E.N., Fishman, V.M., Ryaboyi, V.Z., and Sitnikova, G.A., 1974, The Tau method for inversion of traveltimes–I. Deep seismic sounding data, Geophysical Journal of the Royal Astronomical Society **36**, pp. 377-398.

Bessonova, E.N., Fishman, V.M., Shnirman, M.G., Sitnikova, G.A. and Johnson, L.R., 1976, The Tau method for inversion of traveltimes–II. Earthquake data, Geophysical Journal of the Royal Astronomical Society, **46**, pp. 87-108.

Carrion, P.M., Kuo, J.T., and Stoffa, P.L., 1984, Inversion method in the slant stack domain using amplitudes of reflection arrivals, Geophysical Prospecting **32**, pp. 375-391

Chapman, C.H., 1978, A new method for computing synthetic seismograms, Geophysical Journal of the Royal Astronomical Society, **54**, pp.481-518.

Chapman, C.H., 1981, Generalized Radon transform and slant stacks. Geophysical Journal of the Royal Astronomical Society, **66**, pp.445-453.

Claerbout, J.F., 1976, *Fundamentals of Geophysical Data Processing*, New York, McGraw-Hill Book Co. Inc., 274 pp.

Clayton, R.W. and McMechan, G.A., 1981, Inversion of refraction data by wave field continuation, Geophysics **46**, pp. 860-868.

Clowes, R.M., 1985, Study of upper crustal structure below Hecate Strait from Air-gun/Ocean Bottom Seismograph data, Final Report, DSS Contract file number 06SB.23445-4-1170, 16 pp.

Clowes, R.M. and Gens-Lenartowicz, E., 1985, Upper crustal structure of southern Queen Charlotte Basin from sonobuoy refraction studies, Canadian Journal of Earth Sciences **22**, pp. 1696-1710.

Dehler, S. A., 1986, A seismic refraction study of the Queen Charlotte fault zone, M.Sc. thesis, University of British Columbia, Vancouver, B. C., 112 pp.

Garmany, J., Orcutt, J.A., and Parker, R.L., 1979, Travel time inversion: a geometrical approach, Journal of Geophysical Research, **84**, pp 3615-3622.

Gazdag, J., 1978, Wave equation migration with the phase shift method, Geophysics, **43**, pp.1342-1351.

Heffler, P.E. and Barrett, D.L., 1979, OBS development at Bedford Institue of Oceanography, Marine Geophysical Research, **4**, pp 227-245.

Hillhouse, J.W., 1977, Paleomagnetism of the Triassic Nikolai Greenstone, McCarthy quadrangle, Alaska. Canadian Journal of Earth Sciences, **14**, pp. 2578-2598.

Jones, D.L., Irwin, W.P. and Hillhouse J., 1977., Wrangellia — a displaced terrane in northwestern North America. Canadian Journal of Earth Sciences, **15**, pp. 2565-2575.

Mackie, D., 1985., Subduction beneath the Queen Charlotte Islands? The results of a seismic refraction survey. M.Sc. thesis, University of British Columbia, Vancouver, B.C., 130 pp.

McMechan, G.A. and Wiggins, R.A., 1972, Depth limits in body wave inversions, Geophysical Journal of the Royal Astronomical Society, **283**, pp. 459–473.

McMechan, G.A. and Ottolini, R., 1980, Direct observation of a $p - \tau$ curve in a slant stacked wavefield, Bulletin of the Seismological Society of America **70**, pp. 775-789.

Phinney, R.A., Chowdhury, K.R. and Fraser, L.N., 1981, Transformation and analysis of record sections, Journal of Geophysical Research, **86**, no. BI, pp. 359-377.

Rona, P.A., 1980, Global plate motion and mineral resources. *In* The continental crust and its mineral deposits. *Edited by* D.W. Strangway. Geological Association of Canada, Special Paper 20, pp. 607-622.

Shouldice, D.H., 1971, Geology of the western Canadian continental shelf. Bulletin of the Canadian Association of Petroleum Geology, **19**, pp. 405-436.

——— 1973, Western Canadian continental shelf. *In* Future petroleum provinces of Canada. *Edited by* R.G. McCrossan. Canadian Society of Petroleum Geologists, Memoir 1, pp. 7-35.

Spence, G.D., Whittall, K.P. and Clowes, R.M., 1984, Practical synthetic seismograms for laterally varying media calculated by asymptotic ray theory. Bulletin of the Seismological Society of America, **74**, pp. 1209–1223.

Stacey, R.A., 1975, Structure of the Queen Charlotte Basin. *In* Canada's continental margins and offshore petroleum exploration. *Edited by* C.J. Yorath, E.R. Parker, and D.J. Glass. Canadian Society of Petroleum Geologists, Memoir 4, pp. 723-741.

Stacey, R.A. and Stephens, L.E., 1969, An interpretation of gravity measurements on the west coast of Canada, Canadian Journal of Earth Sciences, **6**, pp. 463-474.

Sutherland Brown, A. 1968. Geology of the Queen Charlotte Islands. British Columbia Department of Mines and Petroleum resources, Bulletin 54, 226 pp.

Tipper, H.W., amd Cameron, B.E.B., 1980, Stratigraphy and paleontology of the Upper Yukon Formation (Jurassic) in Alliford Bay syncline, Queen Charlotte Islands, British Columbia, in Current Research, part C. Geological Survey of Canada, Paper 80-1C, pp. 37-44.

Van der Voo, R. and Channel, J.E.T., 1980, Paleomagnetism in oregenic belts. Reviews of Geophysics and Space Physics, **18**(2), pp. 455-481.

Van der Voo, R., Jones, M., Gromme, C.S., Iberlein, G.D. and Churken, Jr., M., 1980, Paleomagnetism and northward drift of Alexander terrane, southeastern Alaska. Journal of Geophysical Research, **85**, pp. 5281-5296.

Wenzel, F., Stoffa, P.L., and Buhl, P., 1982, Seismic modelling in the domain of intercept time and ray parameter, IEEE Transactions on Acoustics, Speech and Signal Processing, **ASSP-30**(3), pp. 406-422.

Yorath, C.J. and Cameron, B.E.B., 1982, Oil off the west coast? GEOS, **11**, pp. 13-15.

Yorath, C.J. and Chase, R.L., 1981. Tectonic history of the Queen Charlotte Islands and adjacent areas — a model. Canadian Journal of Earth Sciences, **18**, pp. 1717-1739.

Yorath, C.J. and Hyndman, R.D., 1983, Subsidence and thermal history of the Queen Charlotte Basin. Canadian Journal of Earth Sciences, **20**, pp 135-158.

Young, I.F., 1981, Geological development of the western margin of the Queen Charlotte Basin. M.Sc. thesis, University of British Columbia, Vancouver, B.C.

Appendix I

Summary of the Formations for the Queen Charlotte Region

Period	Epoch/ Stage	Group or Formation			Lithology	Maximum Thickness (meters)	Tectonic or Depositional Environment	Intrusive Rocks
Quaternary	Recent				Alluvium		Non-marine and near-shore marine	
	Pleistocene	Cape Ball Formation			Till, sand, silt, clay	150+	Glacial marine and non-marine	
	Pleistocene or Pliocene	Tow Hill Sills			Olivine basalt	110		
Tertiary	Pliocene ? M.-U. Miocene	Skonun Fm.	Upper Marine Mbr.		Calcareous Ss.	1800+	Near-shore marine and non-marine	
					Sandstone, siltstone			
			Basal Conglom.		Conglomerate			
	Lower Miocene	Masset Fm.	Dana Facies		Pyroclastic breccias volcanic Ss, porphyry	1500+		Post Tectonic Plutons Middle Miocene – Upper Eocene Ridge subduction ? Divergent wrenching ?
			Kootenay Facies		Rhyolite tuffs&flows dacite, basalt flows	1200+	Mantle plume ?	
	Oligocene		Tartu Facies	Basalt Mbr.	Basalt flows, pyroclastics, andesite	1500+	Rifting ?	
	Eocene			Rhyolite Mbr.	Rhyolite, ash flows, basalt flows	2100	Divergent wrenching ?	
	Paleocene ?			Mixed Mbr.	Basalt breccias & flows	2000		
Cretaceous	Upper	Queen Charlotte Group	Skidegate Formation		Siltstone, sandstone	600+	Shallow marine	
	Turonian		Honna Formation		Conglomerate, sandstone, shale	1200	Near-shore marine or non-marine	
	Cenomanian		Haida Fm.	Shale Mbr.	Shale, siltstone	330	Near-shore marine	
	Lower Albian			Sdstone Mbr.	Sandstone, siltstone	820		Syntectonic Batholiths Lower Cretaceous (?)–Upper Jurassic Collision event
	Barremian Hauterivian Valangian		Longarm Formation		Siltstone, sandstone conglomerate	1200+	Marine	
Jurassic	Callovian Bathonian	Vancouver Group	Yakoun Fm.	E Mbr.	Volcanic Ss, shale, siltstone, congl.	140	Marine	
	Middle			D Mbr.	Tuffs, tuffaceous sands	240		
	Bajocian			C Mbr.	Andesitic agglomerates and tuffs	290	Volcanic arc	
				B Mbr.	Shale, Ss, tuffs	30+	Marine	
				A Mbr.	Calcareous and lapilli tuffs	200		
	Toarcian		Maude Formation		Shale, sandstone	225	Marine	
	Lower Pleinsbachian Sinemurian Hettangian		Kunga Fm.	Black Argillite Mbr.	Argillite, sltstone, shale, Ls., Ss.	580	Marine	
				Black Limestone Mbr.	Carbonaceous limestone, argillite	270		
				Grey Limestone Mbr.	Limestone	180		
Triassic	Upper Norian		Karmutsen Formation		Basalt flows & pillows, tuffs, minor sediments	4,300	Ocean crust ? Volcanic arc ? Interarc basin ?	
	Karnian							
Lower Permian or Pennsylvanian		Sicker Group ?			Limestone, shale, basalt, diabase	(not exposed ?)	Shallow marine Volcanic arc ?	

Table I.1 Table of formations for Queen Charlotte Islands (Young, 1981).

Appendix II

Horizontal and Hydrophone Component Data
for 1983 Airgun/OBS Survey

Figures II.1 – II.12 Record sections for the horizontal and hydrophone components for OBSs 1 to 4 plotted using the same parameters as those in Chapter IV (see Chapter IV for explanation).

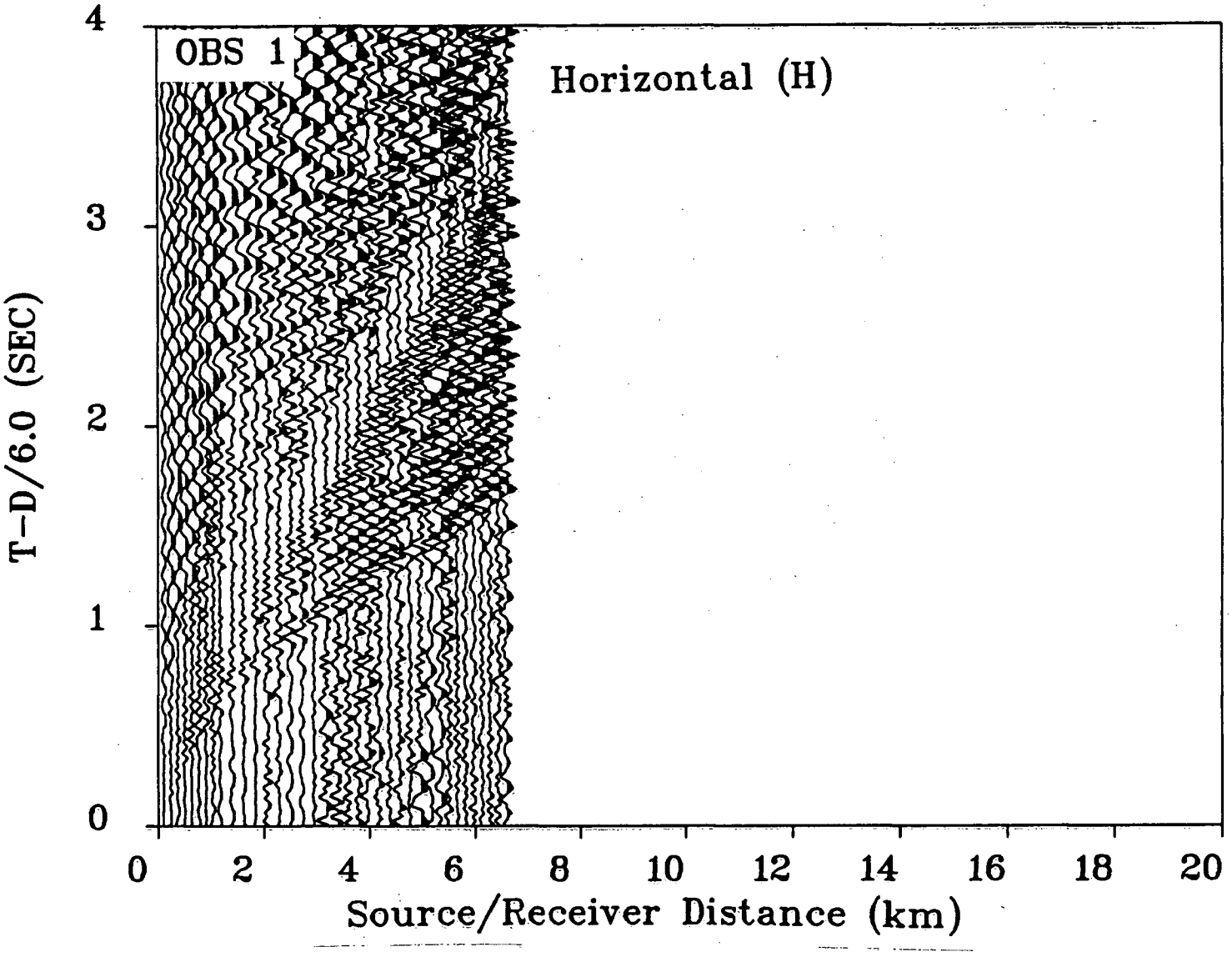
OBS 1
Horizontal (H)
T-D/6.0 (SEC)
4
3
2
1
0
0
2
4
6
8
10
12
14
16
18
20
Source/Receiver Distance (km)

Figure II.1

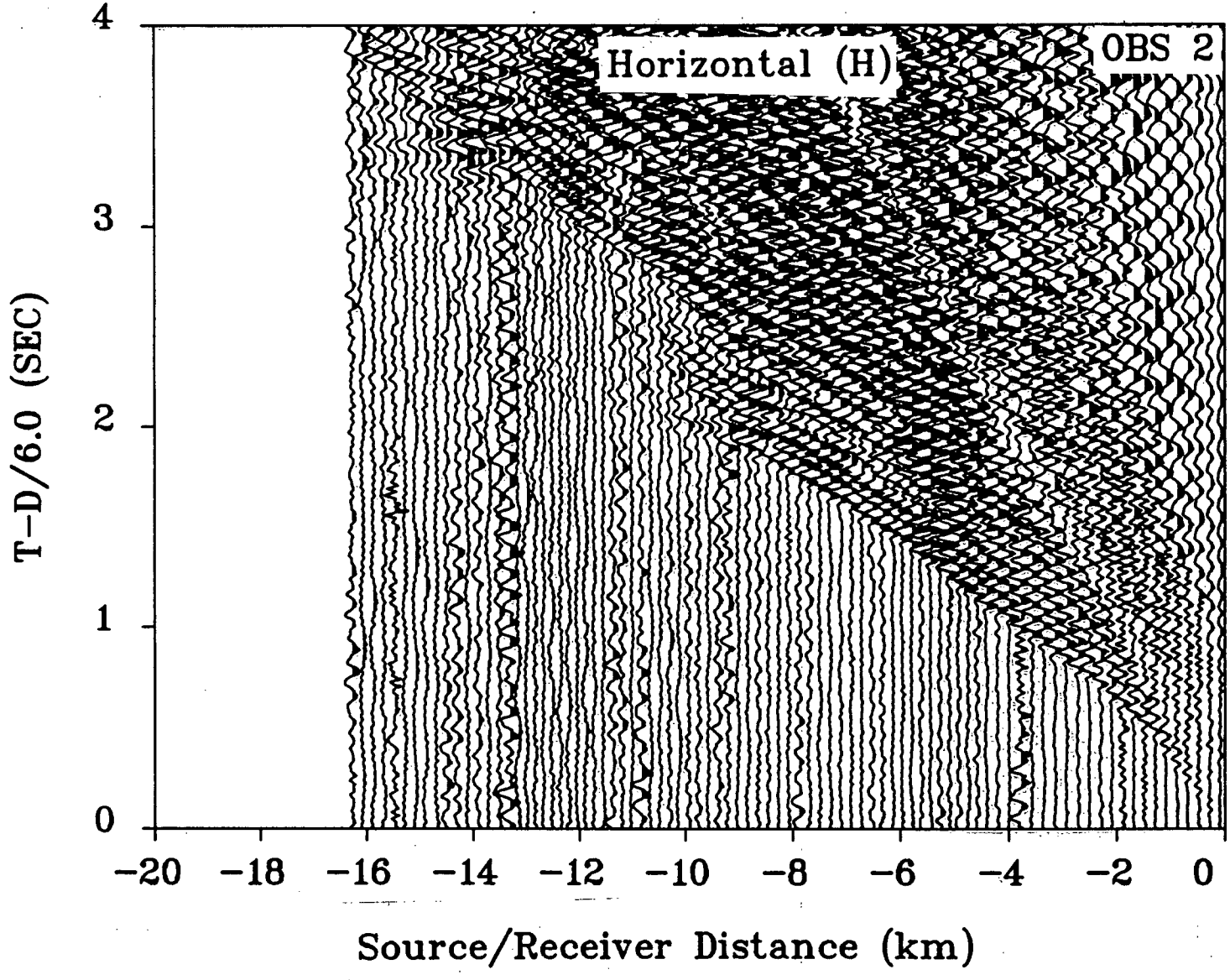
Horizontal (H)
OBS 2
T-D/6.0 (SEC)
4
3
2
1
0
-20
-18
-16
-14
-12
-10
-8
-6
-4
-2
0
Source/Receiver Distance (km)

Figure II.2

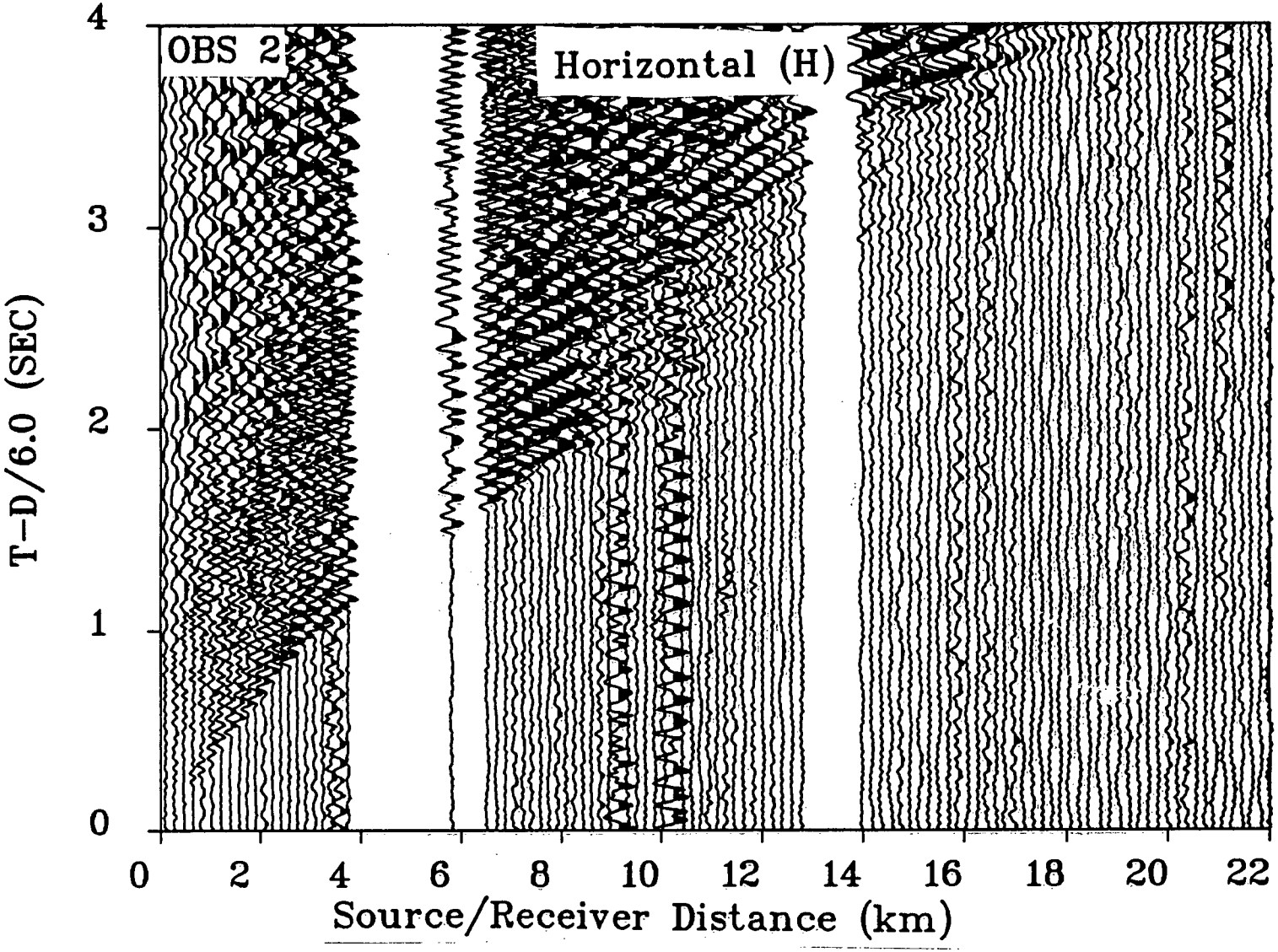
OBS 2
Horizontal (H)
T-D/6.0 (SEC)
4
3
2
1
0
0
2
4
6
8
10
12
14
16
18
20
22
Source/Receiver Distance (km)

Figure II.3

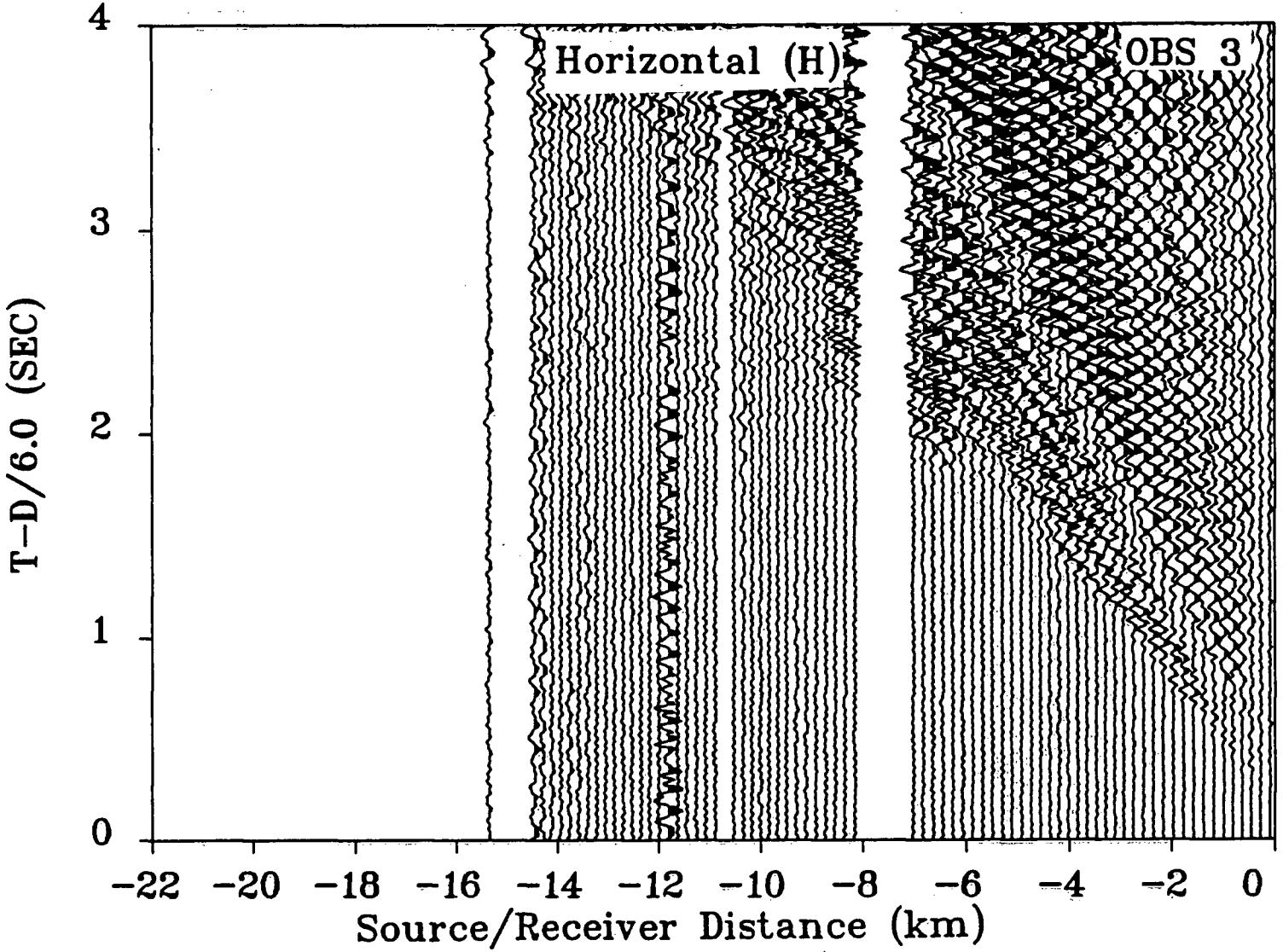
Horizontal (H)
OBS 3
T-D/6.0 (SEC)
4
3
2
1
0
-22
-20
-18
-16
-14
-12
-10
-8
-6
-4
-2
0
Source/Receiver Distance (km)

Figure II.4

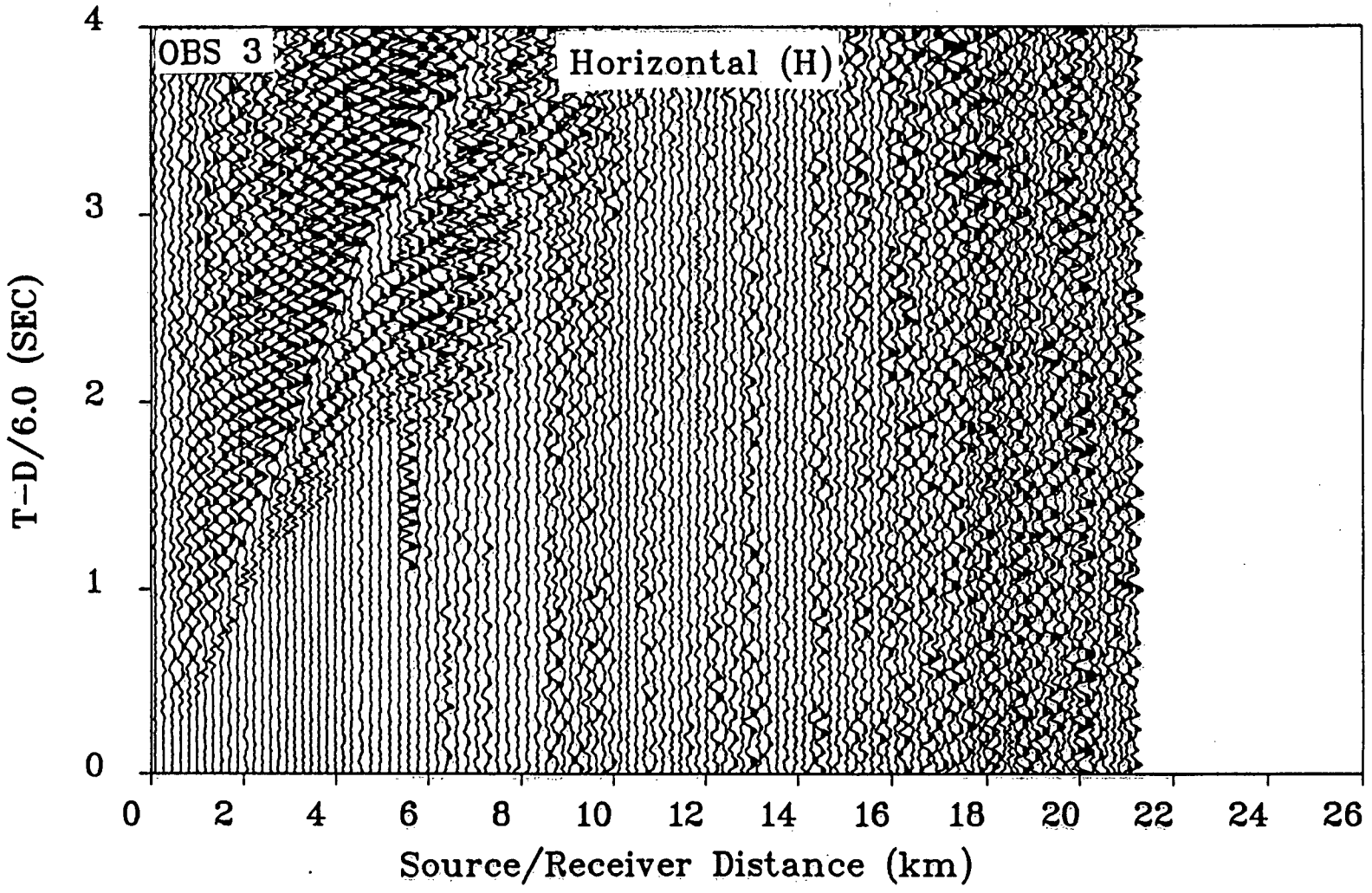
OBS 3
Horizontal (H)
T-D/6.0 (SEC)
0
1
2
3
4
0
2
4
6
8
10
12
14
16
18
20
22
24
26
Source/Receiver Distance (km)

Figure II.5

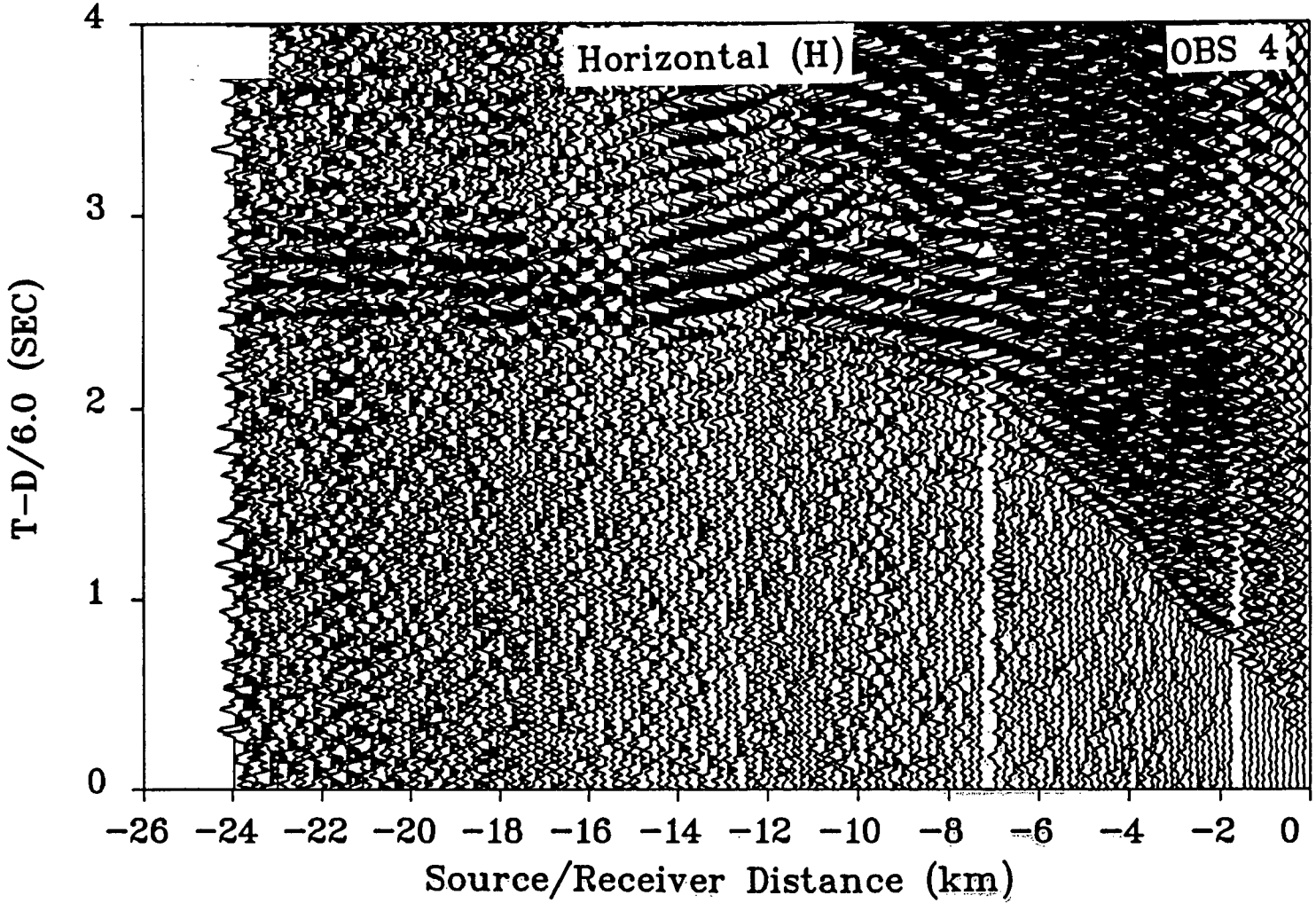
Horizontal (H)
OBS 4
T-D/6.0 (SEC)
4
3
2
1
0
-26 -24 -22 -20 -18 -16 -14 -12 -10 -8 -6 -4 -2 0
Source/Receiver Distance (km)

Figure II.6

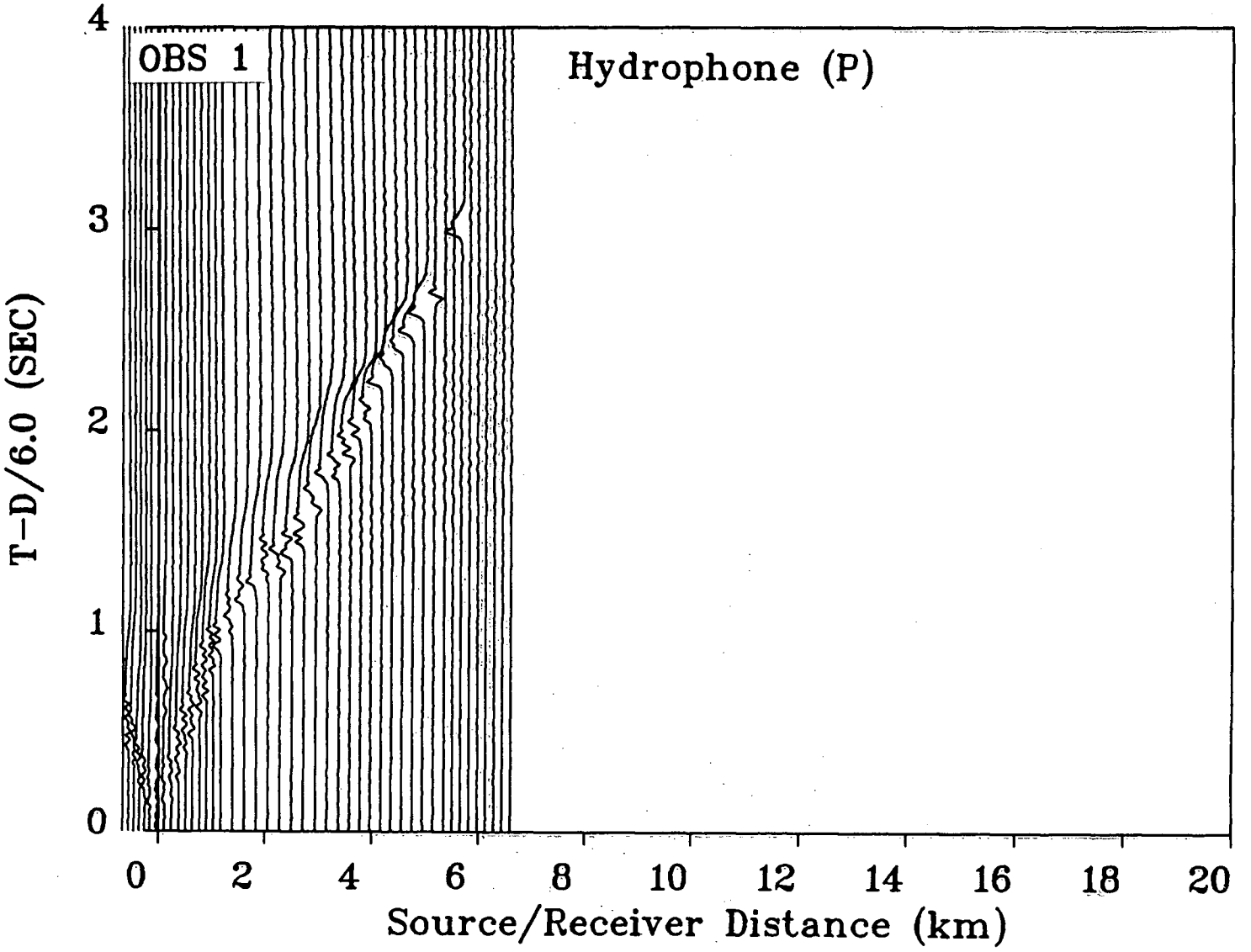
OBS 1
Hydrophone (P)
T-D/6.0 (SEC)
0
1
2
3
4
0
2
4
6
8
10
12
14
16
18
20
Source/Receiver Distance (km)

Figure II.7

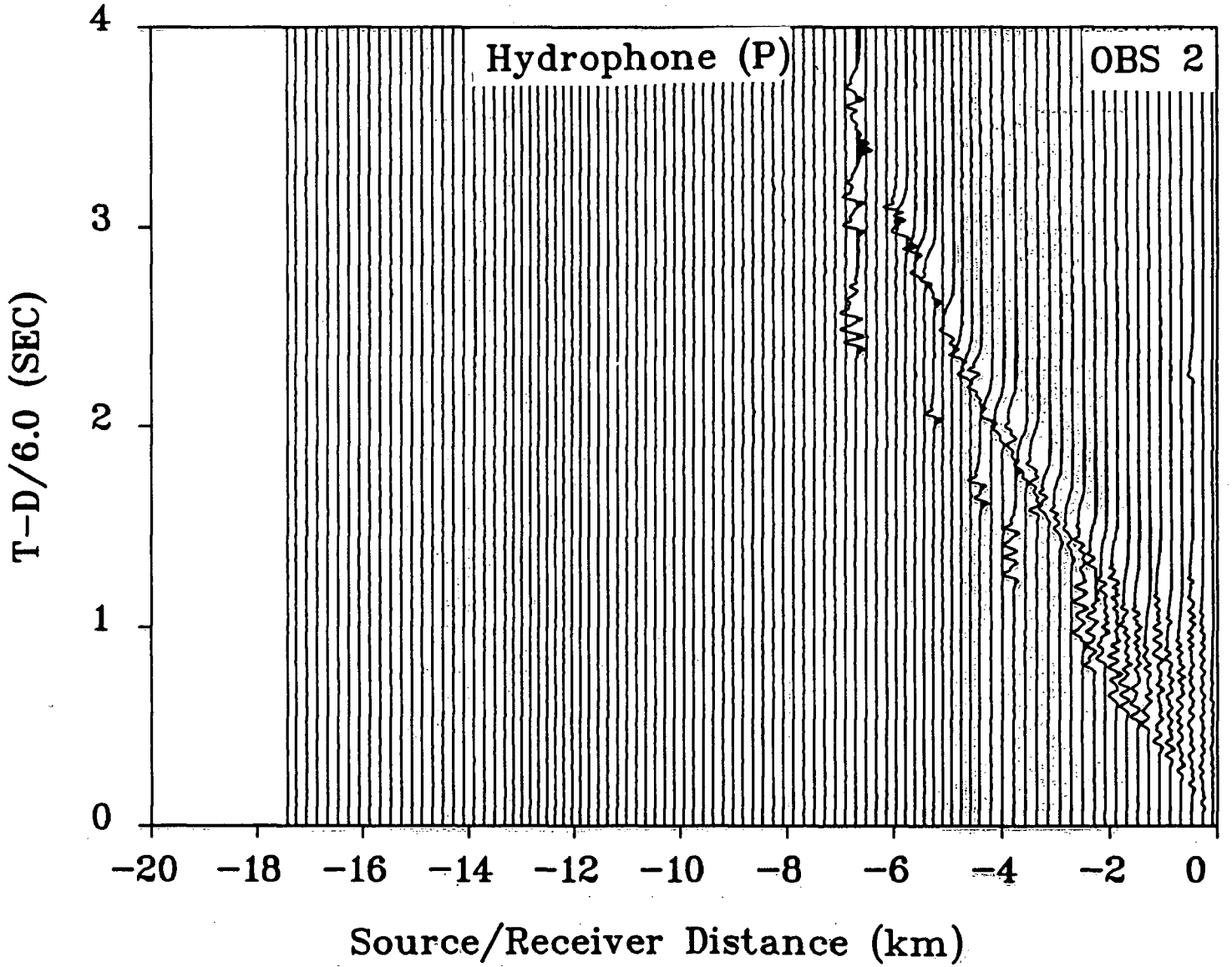
Hydrophone (P)
OBS 2
T-D/6.0 (SEC)
4
3
2
1
0
−20
−18
−16
−14
−12
−10
−8
−6
−4
−2
0
Source/Receiver Distance (km)

Figure II.8

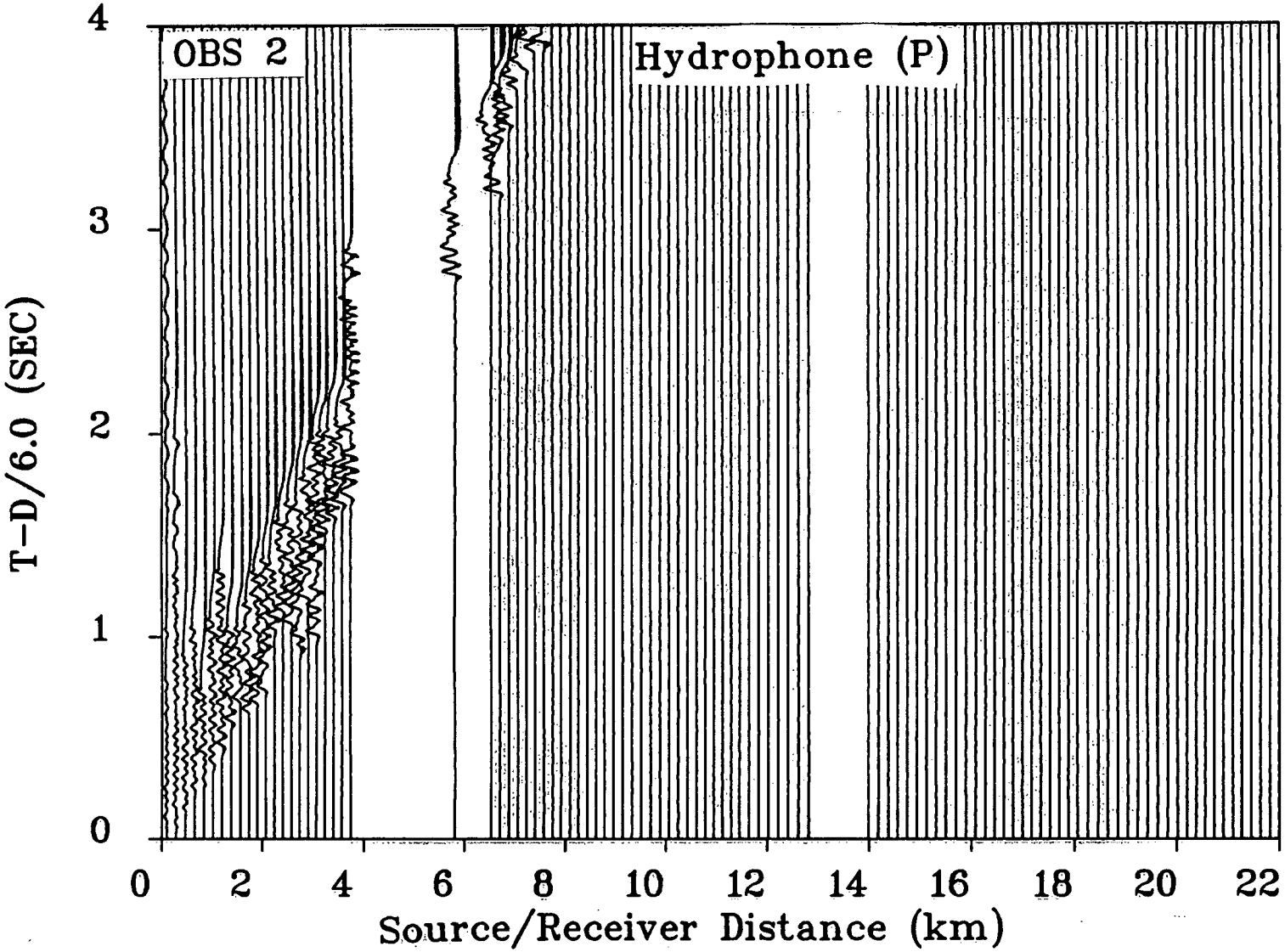
OBS 2
Hydrophone (P)
T-D/6.0 (SEC)
0
1
2
3
4
0
2
4
6
8
10
12
14
16
18
20
22
Source/Receiver Distance (km)

Figure II.9

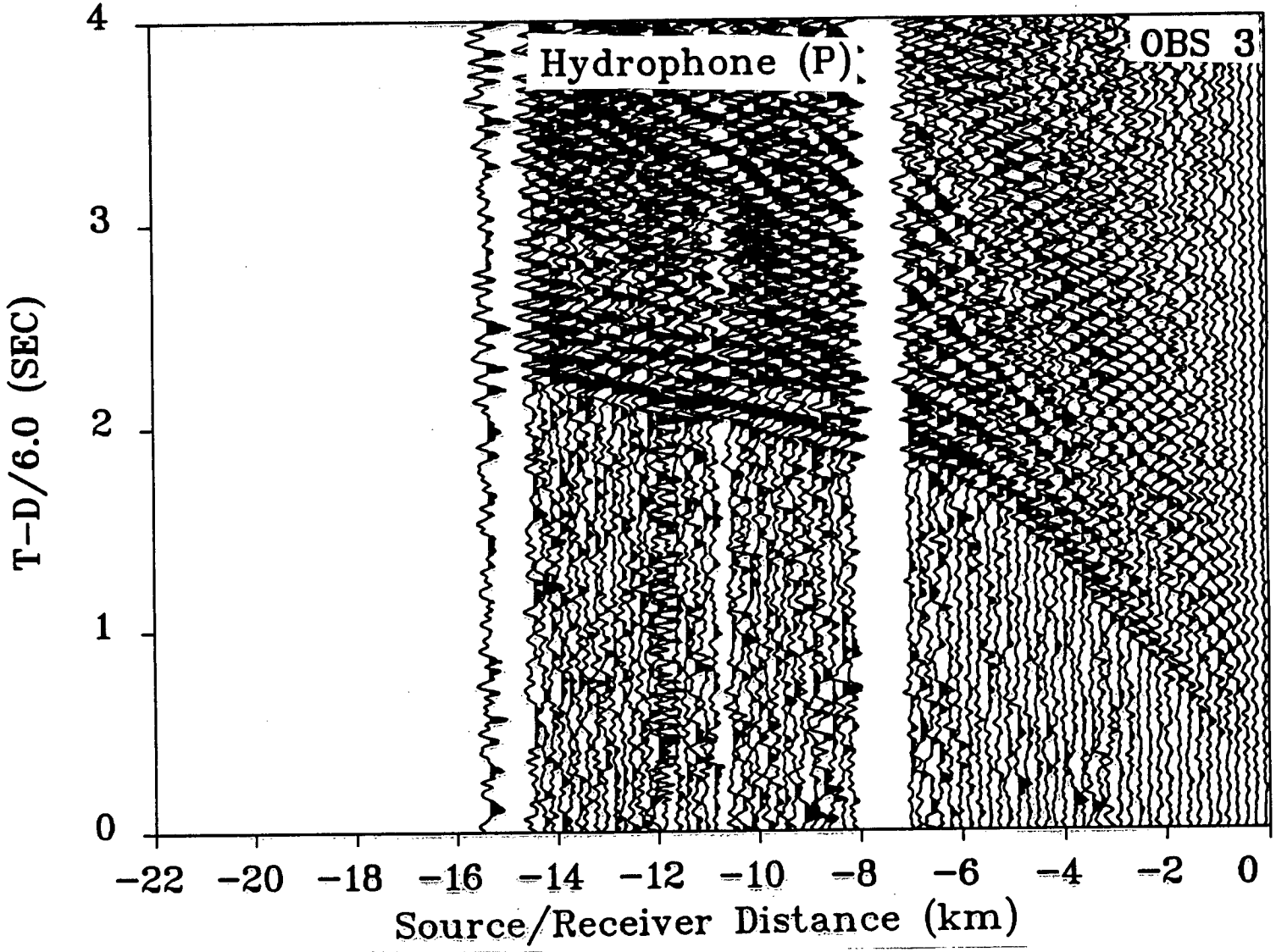
Hydrophone (P)
OBS 3
T-D/6.0 (SEC)
4
3
2
1
0
-22
-20
-18
-16
-14
-12
-10
-8
-6
-4
-2
0
Source/Receiver Distance (km)

Figure II.10

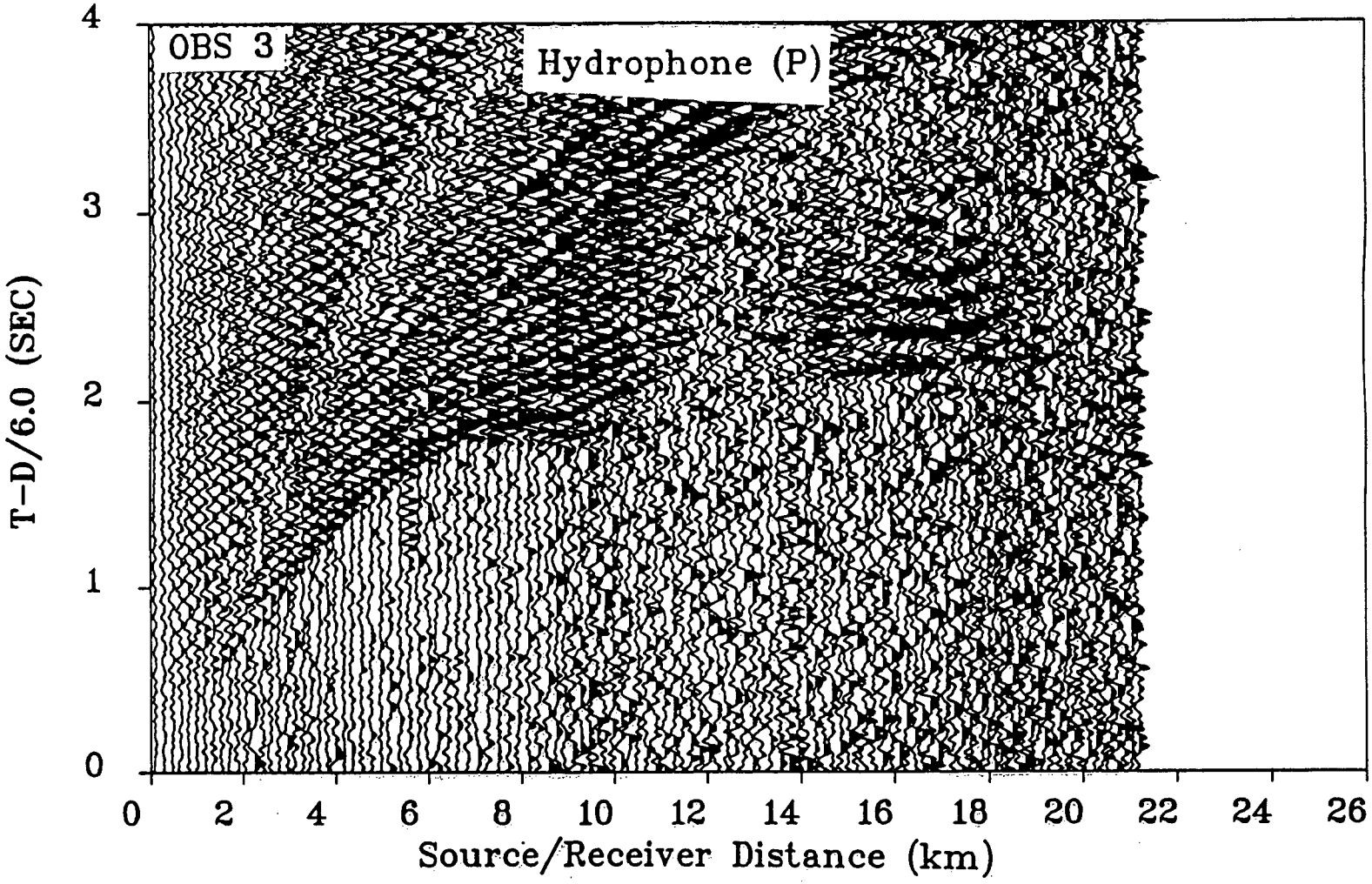
OBS 3
Hydrophone (P)
T-D/6.0 (SEC)
0
1
2
3
4
0
2
4
6
8
10
12
14
16
18
20
22
24
26
Source/Receiver Distance (km)

Figure II.11

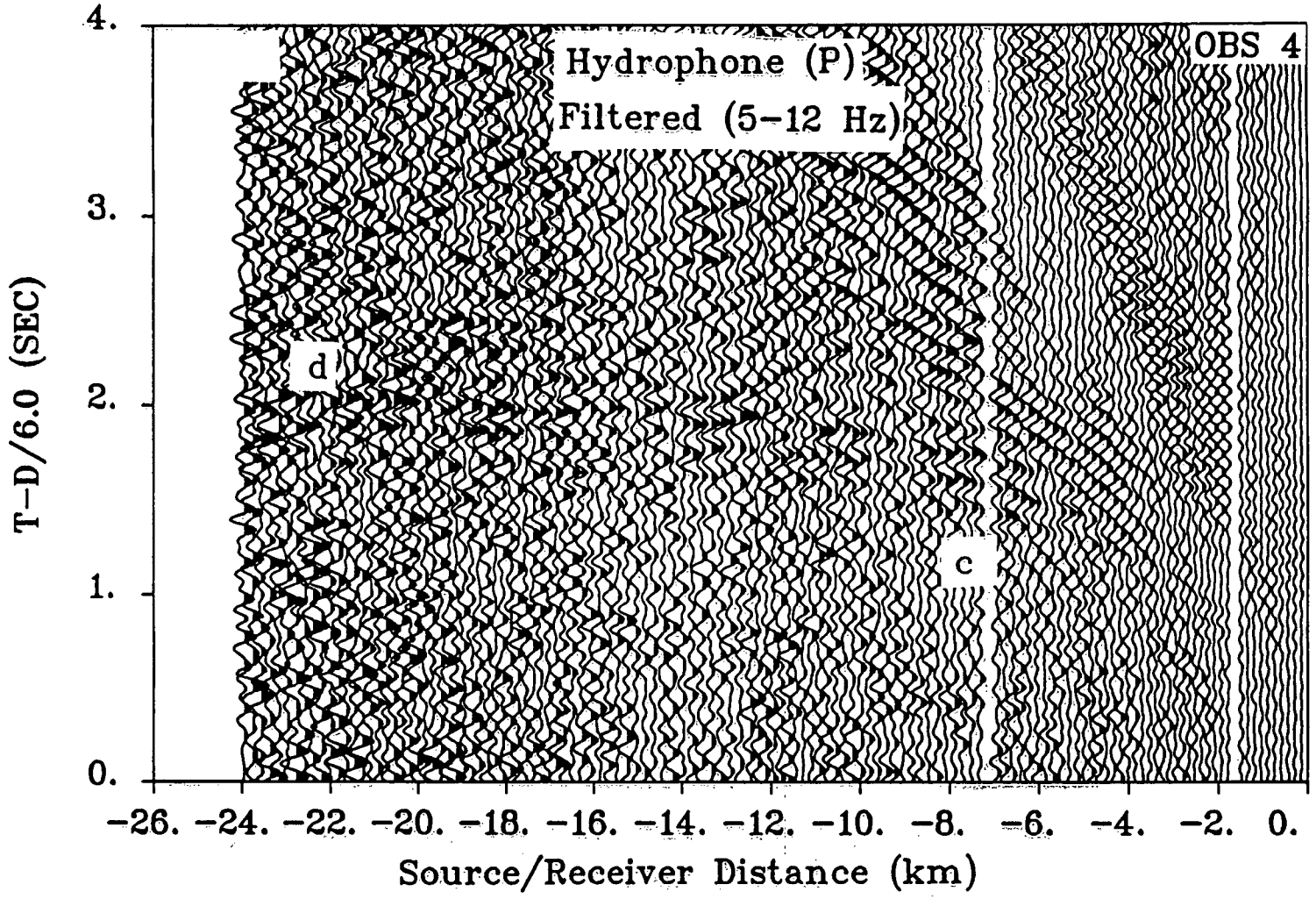
OBS 4
Hydrophone (P)
Filtered (5-12 Hz)
d
c
T-D/6.0 (SEC)
4.
3.
2.
1.
0.
-26. -24. -22. -20. -18. -16. -14. -12. -10. -8. -6. -4. -2. 0.
Source/Receiver Distance (km)

Figure II.12